Declassified and Approved For Release 2013/02/06 : CIA-RDP10-02196R000300020002-8
ISSN 0038-531X

Russian Original Vol. 54, No. 2, February, 1983

August, 1983

[redacted]

PEEL HERE .983)

SOVIET ATOMIC ENERGY

АТОМНАЯ ЭНЕРГИЯ
(ATOMNAYA ÉNERGIYA)

TRANSLATED FROM RUSSIAN

c/b CONSULTANTS BUREAU, NEW YORK

Declassified and Approved For Release 2013/02/06 : CIA-RDP10-02196R000300020002-8

Declassified and Approved For Release 2013/02/06 : CIA-RDP10-02196R000300020002-8

SOVIET ATOMIC ENERGY

Soviet Atomic Energy is abstracted or indexed in *Chemical Abstracts, Chemical Titles, Pollution Abstracts, Science Research Abstracts, Parts A and B, Safety Science Abstracts Journal, Current Contents, Energy Research Abstracts,* and *Engineering Index.*

Soviet Atomic Energy is a translation of *Atomnaya Energiya,* a publication of the Academy of Sciences of the USSR.

An agreement with the Copyright Agency of the USSR (VAAP) makes available both advance copies of the Russian journal and original glossy photographs and artwork. This serves to decrease the necessary time lag between publication of the original and publication of the translation and helps to improve the quality of the latter. The translation began with the first issue of the Russian journal.

Editorial Board of *Atomnaya Énergiya:*

Editor: O. D. Kazachkovskii

Associate Editors: N. A. Vlasov and N. N. Ponomarev-Stepnoi

Secretary: A. I. Artemov

I. N. Golovin
V. I. Il'ichev
V. F. Kalinin
P. L. Kirillov
Yu. I. Koryakin
E. V. Kulov
B. N. Laskorin
V. V. Matveev
I. D. Morokhov
A. A. Naumov
A. S. Nikiforov
A. S. Shtan'
B. A. Sidorenko
M. F. Troyanov
E. I. Vorob'ev

Copyright © 1983, Plenum Publishing Corporation. *Soviet Atomic Energy* participates in the program of Copyright Clearance Center, Inc. The appearance of a code line at the bottom of the first page of an article in this journal indicates the copyright owner's consent that copies of the article may be made for personal or internal use. However, this consent is given on the condition that the copier pay the stated per-copy fee through the Copyright Clearance Center, Inc. for all copying not explicitly permitted by Sections 107 or 108 of the U.S. Copyright Law. It does not extend to other kinds of copying, such as copying for general distribution, for advertising or promotional purposes, for creating new collective works, or for resale, nor to the reprinting of figures, tables, and text excerpts.

Consultants Bureau journals appear about six months after the publication of the original Russian issue. For bibliographic accuracy, the English issue published by Consultants Bureau carries the same number and date as the original Russian from which it was translated. For example, a Russian issue published in December will appear in a Consultants Bureau English translation about the following June, but the translation issue will carry the December date. When ordering any volume or particular issue of a Consultants Bureau journal, please specify the date and, where applicable, the volume and issue numbers of the original Russian. The material you will receive will be a translation of that Russian volume or issue.

Subscription (2 volumes per year)
Vols. 52 & 53: $440 (domestic); $489 (foreign)
Vols. 54 & 55: $500 (domestic); $555 (foreign)

Single Issue: $100
Single Article: $7.50

CONSULTANTS BUREAU, NEW YORK AND LONDON

c/b
233 Spring Street
New York, New York 10013

Published monthly. Second-class postage paid at Jamaica, New York 11431.

Mailed in the USA by Publications Expediting, Inc., 200 Meacham Avenue, Elmont, NY 11003.

POSTMASTER: Send address changes to *Soviet Atomic Energy,* Plenum Publishing Corporation, 233 Spring Street, New York, NY 10013.

Declassified and Approved For Release 2013/02/06 : CIA-RDP10-02196R000300020002-8

Declassified and Approved For Release 2013/02/06 : CIA-RDP10-02196R000300020002-8

SOVIET ATOMIC ENERGY

A translation of *Atomnaya Énergiya*

August, 1983

Volume 54, Number 2 February, 1983

CONTENTS

	Engl.	Russ.
ARTICLES		
International Tokamak-Reactor "INTOR." Phase I — B. B. Kadomtsev and V. I. Pistunovich	83	83
Cooling Conditions of the Reactor of the Beloyarsk Nuclear Power Station First Unit during Shutdown of the Station and Depressurization of the Evaporative Circuit — P. A. Gavrilov, V. G. Zakharov, G. A. Zvereva, A. I. Ionov, V. D. Kozyrev, V. I. Mikhan, Yu. I. Mityaev, T. D. Ogina, L. N. Podlazov, N. Z. Rybakov, A. G. Sheikman, and S. V. Shirokov	103	98
A Test of Correlation Measurements of the Flow Rate of Sodium in the BN-600 Assembly — L. A. Adamovskii, V. G. Vysotskii, V. V. Golovanov, V. V. Golushko, V. N. Efimov, B. V. Kebadze, É. P. Kozubov, and V. I. Kupnyi	106	100
Role of Fast Reactor Physical Characteristics in Limiting the Consequences of Hypothetical Accidents — I. A. Kuznetsov, Yu. E. Bagdasarov, and Yu. M. Ashurko	110	103
Measurements of the Cross Section of the ^{237}Np(n, 2n) Reaction at Neutron Energies of 14.8 MeV — E. A. Gromova, S. S. Kovalenko, Yu. A. Nemilov, L. D. Preobrazhenskaya, Yu. A. Selitskii, B. I. Tarler, Yu. N. Trofimov, V. B. Funshtein, and S. V. Khlebnikov	116	108
Effects of Previous Heat Treatment and Mechanical Working on the Swelling of 0Kh16N15M3B Stainless Steel — V. A. Krasnoselov, V. I. Prokhorov, A. N. Kolesnikov, and Z. A. Ostrovskii	121	111
Corrosion of Zirconium Alloys in the Superheated Steam of a Power Reactor — B. V. Samsonov, S. V. Seredkin, V. N. Shulimov, V. K. Shamardin, and G. I. Maërshina	124	114
Effect of Bombardment with Deuterium Ions on the Structure of Polycrystalline Niobium — A. A. Pisarev, A. I. Evstyukhin, Yu. A. Perlovich, and V. G. Tel'kovskii	127	116
Behavior of Titanium Diboride under Irradiation and Post-Radiation Annealing — L. M. Murzin, V. V. Ogorodnikov, and V. D. Kelim	130	118
LETTERS TO THE EDITOR		
Vacuum Fission Chamber with Compensation of γ-Induced Current — Yu. P. Bakulin, E. K. Malyshev, S. V. Chuklyaev, and O. I. Shchetinin	136	123

Declassified and Approved For Release 2013/02/06 : CIA-RDP10-02196R000300020002-8

Declassified and Approved For Release 2013/02/06 : CIA-RDP10-02196R000300020002-8

CONTENTS

(continued)

Engl./Russ.

Neutron Fields for Research in the IR-100 Reactor — S. A. Barabanov, G. A. Borisov, E. I. Grigor'ev, I. N. Martem'yanov, V. D. Sevast'yanov, G. B. Tarnovskii, and V. P. Yaryna	139	124
Kinetics of Two Strongly Coupled Pulsed Reactors — A. V. Lukin	141	125
Radiation Damage to Tungsten Single Crystals by an Argon Ion Beam — V. N. Bugrov and S. A. Karamyan	144	127
Comparative Neutron-Physics Calculations of Fast Reactors — I. D. Iordanov and N. A. Antonov	147	129
A Universal Neutron Irradiator with a ^{252}Cf Source — M. A. Bak, A. S. Krivokhat-skii, V. A. Nikolaev, B. D. Stsiborskii, and B. M. Shiryaev	152	132
Effects of Hydrogen-Ion Bombardment on the Structure and Composition of a Nickel-Rich Alloy — M. I. Guseva, A. N. Mansurova, O. S. Naftulin, Yu. V. Nikol'skii, P. A. Fefelov, and O. I. Chelnokov	154	134
Removal of Mono-2-ethylhexylphosphoric Acid from Solid Extraction Agents with Di-2-ethylhexylphosphoric Acid — V. B. Dedov, P. S. Trukhlyaev, B. S. Kalinichenko, and I. K. Shvetsov	157	135
Neutron Activity of the Earth and the Cl–Ar Neutrino Experiment — I. R. Barabanov, V. N. Gavrin, G. T. Zatsepin, I. V. Orekhov, and L. P. Prokop'eva	158	136
Ion Synchrotron Complex of V. G. Khlopin Radium Institute — N. A. Perfilov, V. P. Shilov, V. P. Eismont, V. L. Auslender, V. N. Lazarev, and B. L. Faktorovich	161	137

The Russian press date (podpisano k pechati) of this issue was 1/27/1983. Publication therefore did not occur prior to this date, but must be assumed to have taken place reasonably soon thereafter.

Declassified and Approved For Release 2013/02/06 : CIA-RDP10-02196R000300020002-8

Declassified and Approved For Release 2013/02/06 : CIA-RDP10-02196R000300020002-8

ARTICLES

INTERNATIONAL TOKAMAK-REACTOR "INTOR." PHASE I

B. B. Kadomtsev and V. I. Pistunovich

UDC 621.039.6

At the end of 1978 on the initiative of the Soviet government, work began on the project of an international tokamak-reactor, dubbed INTOR. An International Working Group (IWG) consisting of representatives of scientists and engineers from four parties — Euratom members, the USSR, the USA, and Japan — was organized at the IAEA in Vienna. The International Council on Thermonuclear Fusion (ICTF), which is a consultative organ of the IAEA General Directorate, formulated the following task for the Group:

1. To determine the goals and characteristics of an experimental facility in the world thermonuclear tokamak program which would follow the large JET, JT-60, T-15, and TFTR tokamaks under consideration at present and which can be built on the basis of international cooperation.

2. To evaluate the preparedness of industry for the construction of such a facility in the early 1990's.

3. To specify experiments necessary for producing a project for the reactor.

4. To develop a detailed project for the reactor and a detailed program of experiments on it.

5. To build the reactor and ensure its operation on an international basis.

It was agreed that the work on INTOR would be carried out in separate phases. The zero phase of the project was successfully implemented in 1979 [1]. The main work was done by experts of the participating parties under the leadership of the Group. The contribution of each party is estimated at 15-20 man-years with the participation of the leading scientists and engineers working in the field of thermonuclear fusion. Each party presented a national contribution on the zero phase of the project to the Group for consideration [2-5]. On the basis of these contributions after discussions at meetings of the Group an international report on the zero phase was prepared [1].

The goals set for INTOR characterize this facility as an engineering—technological test tokamak-reactor with a long burn time of the deuterium—tritium fusion reaction. INTOR should represent the stage of engineering demonstration of controlled fusion as a new source of energy. This step is a natural stage after the physical demonstration which is proposed for the facilities now under construction (JET, JT-60, T-15, and TFTR). The main results of the work of Soviet scientists and engineers in the zero phase were presented in [6].

On the basis of the results of the zero phase the Group decided to continue this activity in the next phase (phase I) in order to develop the conceptual project of the reactor. The ICTF considered the report of the Working Group and recommended that the IAEA continue the work in this phase. Phase I was completed in June, 1981. The INTOR parameters agreed upon by the Working Group in the zero phase served as the initial conditions for designing. The contribution of each party in phase I was presented in a national report on the conceptual INTOR design. The four national designs [7-10] formed the basis for the international conceptual design [11] which the Working Group prepared in June, 1981.

The ICTF discussed the Working Group report on phase I and recommended that the work be continued in the next phase (phase IIA) within the organizational framework employed in the previous work. The phase-IIA workshop envisages optimization of the INTOR conceptual design and is to be conducted from July, 1981 to June, 1983.

OBJECTIVES OF INTOR

The objectives of INTOR follow from the role that it should play in the development of the world fusion program and by the engineering capabilities which may arise in the next sev-

Translated from Atomnaya Énergiya, Vol. 54, No. 2, pp. 83-98, February, 1983. Original article submitted July 15, 1982.

0038-531X/83/5402-0083$07.50 © 1983 Plenum Publishing Corporation

Declassified and Approved For Release 2013/02/06 : CIA-RDP10-02196R000300020002-8

Declassified and Approved For Release 2013/02/06 : CIA-RDP10-02196R000300020002-8

TABLE 1. Schedule of INTOR Operation

Stage	No. of years	Principal investigations	Utilization factor, %	Annual fluence of 14-MeV neutrons,* $MW \cdot yr \cdot m^{-2}$	Annual tritium requirement, kg
IA	1	Operation with hydrogen plasma, verification of functioning of units	10	—	—
IB	2	Operation with D – T plasma	15	0,16	3,6
II	4	Engineering tests	25	0,31	6,9
III	8	Engineering tests at maximum parameters†	50	0,62	13,8

*In test modules set up on the outside of the torus.
†Roughly 5 $MW \cdot yr \cdot m^{-2}$ for $\leq$ 10 yr after the end of the second stage.

veral years for the construction of the reactor project. The engineering foundations were assessed and the required additional investigations were determined in the zero phase [1].

The program objectives of INTOR are:

INTOR should attain the plasma parameters necessary for the operation of a demonstration reactor;

study and develop the reactor technology required for the construction of a demonstration power reactor;

serve as a facility for blanket testing, production of tritium and materials, and development of an engineering technology;

demonstrate the reliability of fusion reactor components;

study the system for operating a thermonuclear reactor;

make it possible to investigate factors that affect the reliability, operating safety, and protection of the environment during operation of the thermonuclear reactor.

The technical objectives of INTOR have been formulated so that this program can be accomplished.

The technical objectives of INTOR are:

A. Reactor operating regime:

1. Ignition of a fusion reaction in D–T plasma.
2. Burning of D–T reaction controlled for more than 100 sec.
3. Reactor level of heat and particle fluxes ($\geq$ 1 MW/m^2).
4. Optimal plasma parameters.
5. Load factor $\geq$ 70%.
6. Utilization factor 25-50%.

B. Reactor technology:

1. Superconducting toroidal and poloidal coils.
2. Control of the composition of the plasma (divertor).
3. Monitoring of the fusion power level.
4. Plasma heating and fuel makeup.
5. Heat removal from blanket and production of tritium.

Declassified and Approved For Release 2013/02/06 : CIA-RDP10-02196R000300020002-8

Declassified and Approved For Release 2013/02/06 : CIA-RDP10-02196R000300020002-8

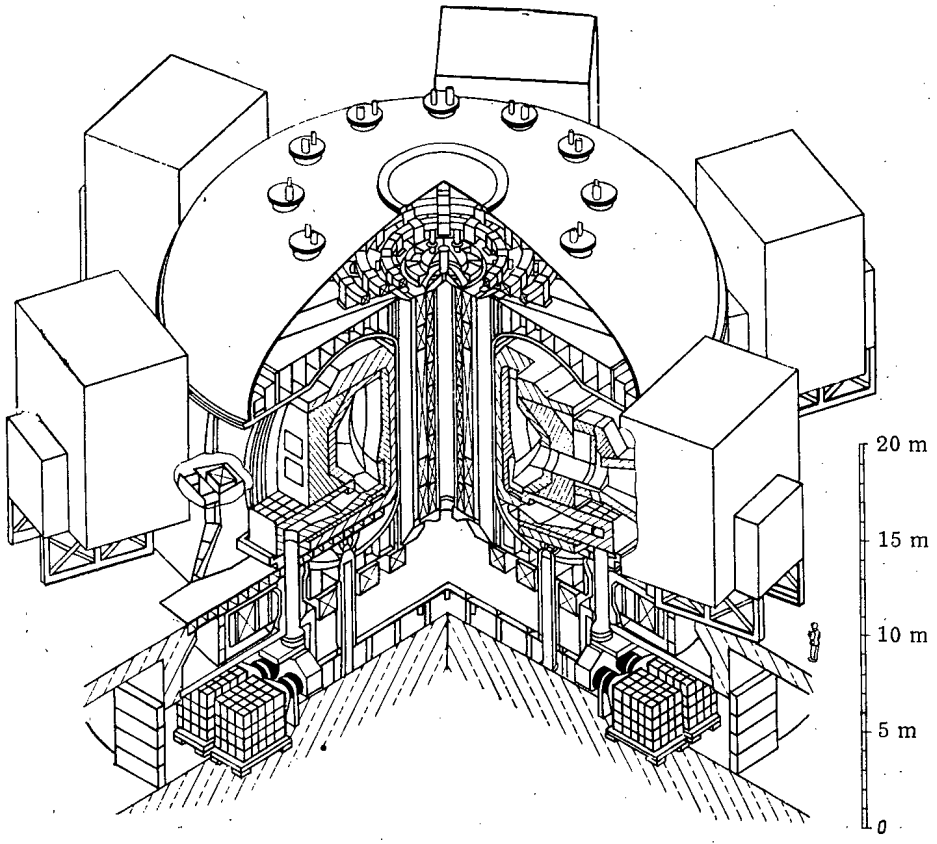

Fig. 1. General view of INTOR.

6. Tritium fuel cycle.
7. Remote servicing.
8. Vacuum engineering.
9. Fusion power cycle.

C. Engineering tests:

1. Breeding and extraction of tritium.
2. Advanced blanket concepts.
3. Materials testing.
4. Plasma engineering.
5. Production of electricity [5-10 MW(elec.)].
6. Neutron fluence $\sim$5 MW·yr·m^{-2} during phase III for testing the reliability and radiation resistance.

These requirements will be met in several stages of INTOR operation (Table 1). In stage I optimum regimes of operation with D–T plasma will be investigated. Most of the problems of groups A and B will be solved in the first stage of reactor operation. Stage II will be devoted to engineering tests, the bulk of which will pertain to group C. During operation in stage III a reactor regime is to be attained with a high utilization factor and a high neutron fluence for testing materials and the operating reliability of the reactor units.

DESCRIPTION OF CONCEPTUAL DESIGN

General Remarks. The conceptual design executed in phase I is based on the realistically expected laws of similarity of the behavior of plasma with fusion parameters and on the expected development of technology in the next several years. This consistent design, which is fairly detailed as to the individual units, gives an idea of emergent problems and possible ways of solving them. The principal parameters of the reactor (Fig. 1) are given:

Declassified and Approved For Release 2013/02/06 : CIA-RDP10-02196R000300020002-8

Declassified and Approved For Release 2013/02/06 : CIA-RDP10-02196R000300020002-8

Geometric:

major radius of chamber, m	5.2
chamber volume, m^3	320
area of chamber surface, m^2	380

Plasma:

minor radius of plasma, m	1.2
elongation of plasma cross section	1.6
aspect ratio of plasma	4.4
mean value of beta $<\beta>$, %	5.6
poloidal beta β_I	2.6
average ion temperature, keV	10
average ion density, 10^{20} m^{-3}	1.4
energy-confinement time, sec	1.4
plasma current, MA	6.4
field on axis, T	5.5
stability safety factor (on separatrix)	2.1
fusion power, MW	620
neutron load on wall, $MW \cdot m^{-2}$	1.3

Operating:

burn time (stages I/II and III), sec	100/200
load factor (stages I/II and III), %	70/80
No. of pulses during operation	$7 \cdot 10^5$
maximum utilization factor, %	50

Neutral-beam heating system:

No. of injectors (operating/reserve)	4/1
beam power, MW	75
beam energy, keV	175
pulse duration, sec	10

Fuel makeup system	Pellet injection and gas filling

Impurity control:

method	Single-zero poloidal divertor
collector	Tungsten, riveted or welded to copper or stainless steel cooling backing
power reaching divertor, MW	80

First wall:

power at first wall (without neutrons), MW	44
at outer contour of torus:	
material	SS-316 stainless steel, cooled with water D_2O
thickness, mm	11.7
at inner contour of torus:	
material	SS-316 stainless steel, cooled with water H_2O
thickness, mm	13.5
lifetime, yrs	15

Blanket:

material	H_2O, SS-316, Li_2SiO_3, Pb, C
temperature, °C	400-600
thickness, m	0.5
location	On outside and top
breeding ratio	0.65

Declassified and Approved For Release 2013/02/06 : CIA-RDP10-02196R000300020002-8

Declassified and Approved For Release 2013/02/06 : CIA-RDP10-02196R000300020002-8

tritium removal	Continuous, with helium
tritium charged, kg	1

Tritium makeup:

tritium circulation rate, $g \cdot h^{-1}$	64
annual tritium requirement at 25% utilization factor, $kg \cdot yr^{-1}$	7
isotopic enrichment	Cryogenic distillation

Tritium charge, kg:

blanket	0.5-1
reserves	2.3
plasma system	0.2
makeup system, pumps, etc.	0.4

Shielding, m:

internal (blanket + shield)	0.85
external (blanket + shield)	1.55
in central injection pipe	1.0
around injectors	0.5-0.75

Toroidal vacuum system:

initial base pressure, Pa	$1.33 \cdot 10^{-5}$
base pressure between pulses, Pa	$4 \cdot 10^{-3}$
pumps	Mixed cryosorption
pumping out	Through divertor chamber

Toroidal field coils:

number	12
internal size, m	7.75·10.7
conductor	Nb_3Sn, NbTi
stabilizer	Cu
maximum field, T	11.6

Poloidal field coils:

total flux, W·sec	110
location	On outside of toroidal coils
conductor	NbTi
maximum field, T	8

Windings for gas breakdown:

breakdown voltage, V	70
location	Inside solenoid
conductor	Cryoresistive, Cu

Electrical stored energy:

No. of energy storage devices	6
total stored energy in one generator, GJ	4
peak load on generator, MVA	750

Mechanical configuration:

The sectors of the blanket are assembled by rectilinear motion in the horizontal direction through windows between the toroidal coils. The semifixed shield inside the torus, on top and at the bottom, forms the primary vacuum boundary at the inner surface. The end flange of the primary vacuum boundary is at the outer boundary of the blanket sector. The test modules are inserted horizontally in the median plane. All of the superconducting coils are in a common cryostat. Of the 12 sectors, 5 are used for the injection of fast atoms, 2 are for fuel makeup, 3 are for tests, and 2 are for diagnostics and control.

Declassified and Approved For Release 2013/02/06 : CIA-RDP10-02196R000300020002-8

Declassified and Approved For Release 2013/02/06 : CIA-RDP10-02196R000300020002-8

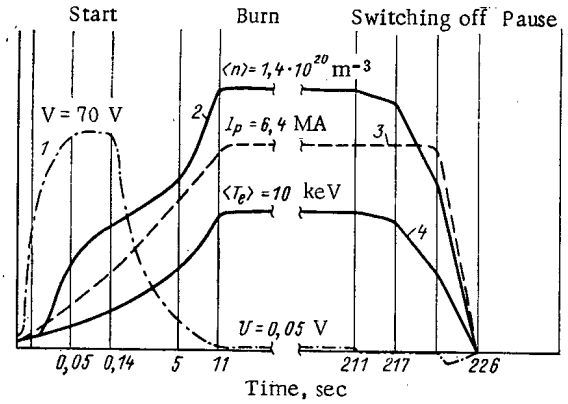

Fig. 2. INTOR operating cycle: 1) voltage per circuit of plasma filament; 2) plasma density; 3) plasma current; 4) electron temperature.

As one of the technical objectives for INTOR it is proposed to bring the utlization factor up to 50% in the last stage of operation. Analysis of the reliability of the reactor operation, based on an estimate of the reliability of its separate components, shows that reactor reliability requires intensified efforts to ensure reliable operation of its components. When the present operating reliability of the various units is taken into account, the utilization factor may be 30-40%.

Physical Substantiation. The physical foundations of INTOR, described in the zero-phase report [1], were developed and reviewed in phase I from the point of view of consistent solutions of the physical and engineering aspects. The main problems are those of plasma confinement, the maximum value of β, the characteristics of the tearing instability, energy transport caused by the corrugation of the magnetic field, production and maintenance of plasma equilibrium including the requirements of the system of the poloidal magnetic field, the physics of wall and divertor plasma, the thermal load and the particle flux at the first wall and in the divertor chamber, and problems associated with the operating cycle (raising the current, heating the plasma to ignition of the reaction, control of the burn, suppression of the reaction and turning off the discharge and the pause between pulses).

The use of alcator scaling leads to attainment of the ignition regime. A considerable indeterminacy still exists, however, in the extrapolation of the experimental results obtained for INTOR. Undesirable tendencies cannot be ruled out as yet, in particular as β is increased. Moreover, the estimates of the possibility of confining energy in plasma do not take sufficiently accurate account of the energy losses for the radiation of heavy impurities. This means that the poloidal divertor should serve as an effective means of preventing the plasma from accumulating heavy impurities in it.

The theoretically predicated limiting value of β is roughly 3%. Such a value, however, has already been attained in a tokamak with a circular plasma cross section. If the elongation and triangular shape of the cross section of the plasma do give the expected positive result, then β = 5.6%, adopted in the INTOR parameters, will prove possible. These data must be substantiated experimentally and this will be done in the near future.

A description of tearing instability and its characteristics has been elaborated for INTOR. Although additional investigations of tearing have been carried out, there is still not sufficient knowledge of the details of this effect in existing devices, and extrapolation to the INTOR operating regimes adds a large indeterminacy. In better regimes with ohmic heating of the plasma the tearing frequency increases. For INTOR, a tearing frequency of $5\cdot10^{-3}$ and 10^{-3}, respectively, has been assumed for the initial and later periods of operation with a characteristic energy-liberation time of 20 msec. It has been shown experimentally that the limiting value of the density in the tokamak grows as the plasma is purified of impurities. The use of additional heating leads to high values of density. The energy losses because of the corrugation of the magnetic field depends weakly on the temperature. An estimate of the loss of particles injected for heating the plasma indicates that the losses remain within allowable limits.

Considerable efforts have been undertaken to develop a divertor design for INTOR that would be consistent as far as the physics and engineering are concerned. It has been shown

Declassified and Approved For Release 2013/02/06 : CIA-RDP10-02196R000300020002-8

Declassified and Approved For Release 2013/02/06 : CIA-RDP10-02196R000300020002-8

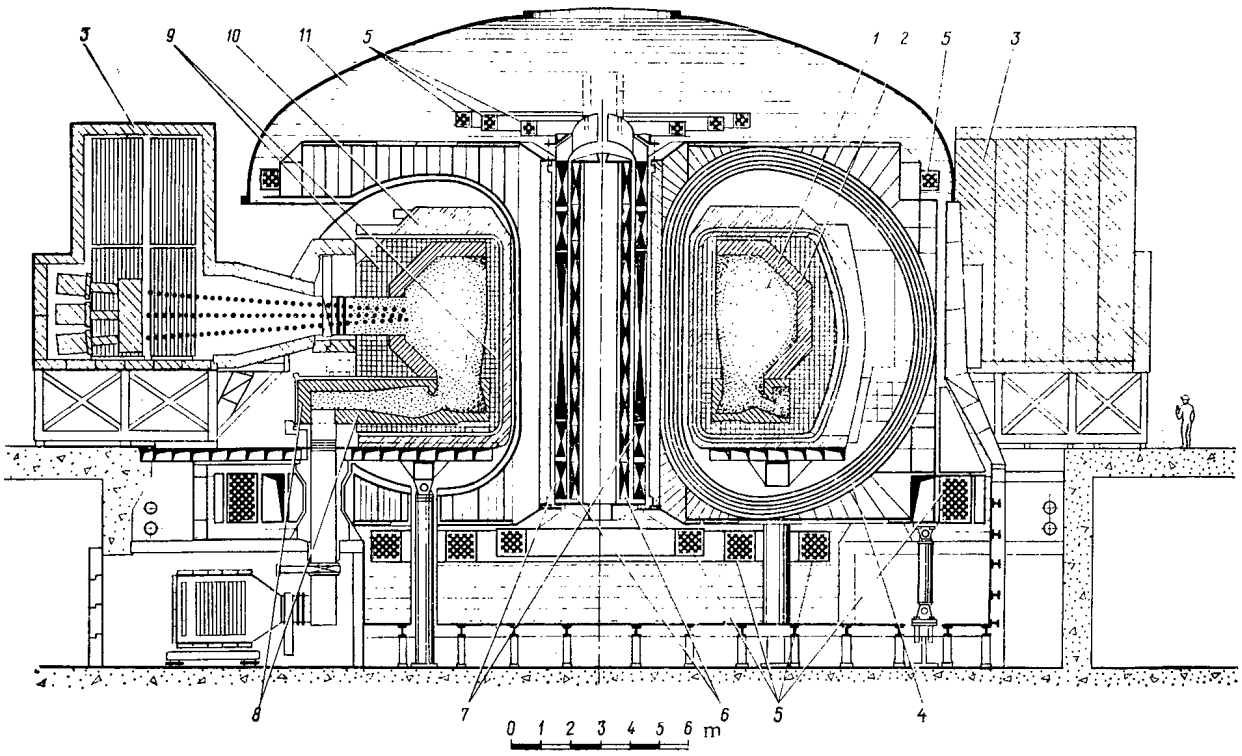

Fig. 3. Cross section of reactor: 1) plasma; 2) blanket; 3) injector of fast atoms; 4) torodial field coils; 5) poloidal field coils; 6) cryoresistive part of inductor; 7) superconducting inductor; 8) divertor chamber; 9) removable shield; 10) semifixed shield; 11) cryostat.

that the plasma can be confined in the configuration of a poloidal divertor with one zero at $\beta_I = 2.6$ by means of a system of poloidal field coils located outside the toroidal windings. The modulus of the sum of the currents in the poloidal coils is about 100 MA × No. of turns. Preliminary analysis indicates that this configuration can be established during heating of the plasma from the ohmic regime to ignition. The horizontal position of the plasma can be easily controlled. As for the control of the vertical position and the shape of the plasma filament, it is proposed that a system of passive turns on the first wall be used. New results have been obtained on the modeling of plasma behavior in the region of the wall and in the divertor chamber. New experimental results have been obtained on tokamaks with a divertor. It has been established that INTOR will operate at high density ($\sim 5 \cdot 10^{19}$ m^{-3}) and at low temperature ($\sim$100 eV) of plasma in the wall region if it is possible to have a regime with a strong recycling of gas in the space of the divertor. Under these conditions, the pumping rate that ensures removal of helium and other impurities reaches a value of about $2 \cdot 10^5$ liters·sec^{-1}. The depth of penetration of impurity atoms in the plasma is small, being a few centimeters. The self-sputtering of the divertor plates is also minimal. An open poloidal-divertor geometry, therefore, is applicable and it is expected that a cold protective plasma layer will exist near the first wall if the thickness of the divertor layer is 10 cm or more.

The main features of the operating cycle, which were presented in the zero phase, have been confirmed in phase I (Fig. 2). New results on the initiation of current in plasma enable the initial voltage per circuit of torus to be reduced to 70 V. It is desirable to introduce rf power of 5-10 MW in order to facilitate gas breakdown and an increase in the current. A 5-sec ohmic phase of plasma heating seems to be a reasonable duration. Heating the plasma to ignition by 175-keV, 75-MW atomic beams continues to be preferable. Radio frequency methods of heating (ion-cyclotron, lower-hybrid, and electron-cyclotron) can be used if they can be demonstrated to be physically and technically feasible. The burn time has been increased to 200 sec but remains substantially shorter than the INTOR total skin time. Controlling the reaction burn regime by means of corrugation losses which grow with the temperature proves to be less definite. On the other hand, the latest experiments revealed the existence of a limiting β such that losses increase sharply as it is approached. It cannot be ruled out that it is necessary to have a control system incorporating a combination of dif-

Declassified and Approved For Release 2013/02/06 : CIA-RDP10-02196R000300020002-8

Declassified and Approved For Release 2013/02/06 : CIA-RDP10-02196R000300020002-8

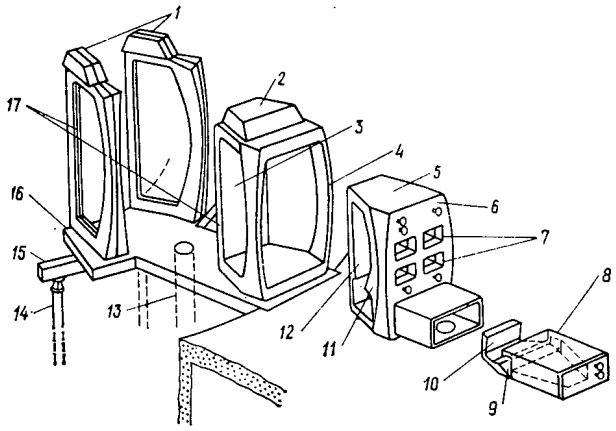

Fig. 4. Component parts of an INTOR sector: 1) torus supports; 2, 3) semifixed torus sector and inner shield; 4) vacuum seal; 5, 6) interchangeable torus sector and outer shield; 7) test modules; 8) divertor module; 9, 10) outer and inner collector plates; 11) blanket; 12) interchangeable outer shield; 13) pump-out piping; 14) inner support column; 15, 16) beam and lower support of torus; 17) sealed surface of supports in sector.

ferent methods. Further work is required to find a satisfactory solution. The duration of the quenching phase has been increased to 15 sec in conformity with new results of calculations. Preliminary analysis of gas pumping from the operating volume during the pause between working pulses revealed that a duration of 20 sec is sufficient.

Mechanical Configuration. Servicing. Activation of the machine by thermonuclear neutrons, the presence of tritium, and the complicated electromagnetic system of the tokamak give rise to potentially serious problems for servicing and preparing the reactor for operation. From the very beginning of work on the design, therefore, consideration of the problems of servicing has been fundamental for the development of the design. A philosophy of the main reactor servicing that satisfies the requirements of the configuration under consideration was elaborated during the conceptual design stage. The existence of such a philosophy has led to a modular concept of the design and has affected the design of all systems of the tokamak from the point of view of fulfilling the requirement that they be accessible. The main features of the configuration of the INTOR design are considered below. A cross section of the reactor is shown in Fig. 3.

The Accessibility Requirement in the Design of the Magnetic Field Coils. The most significant feature of the design configuration is the possibility of access for servicing the torus system. The 12 toroidal field (TF) coils are of a size such that a toroidal sector, constituting 1/12-th of the torus, can be removed completely simply by displacement in one direction between the outer supports of the TF coils. These 12 sectors are installed inside a semifixed frame that protects the torus from the top, inside, and underneath.

In order to simplify the reactor servicing, all of the poloidal field (PF) coils are installed on the outside of the TF coils, above and below, so as to provide free windows for the assembly of the sectors. All of the PF coils can be superconducting since their assembly does not require mechanical coupling. A small solenoidal resistance coil is placed inside the solenoid for ohmic plasma heating so as to deliver a voltage pulse for gas breakdown.

Cryogenic Vacuum Topology. Since the PF coils are on the outside of the TF coils and are superconducting, it proved possible to design a single cryostat linking all the coils. The cryostat incorporates all the individual enclosures for the outer supports of the TF coils as a part of the overall cryostat. It is thus possible to ensure access to the torus without disrupting the cryogenic vacuum boundary. Another significant difference of the design is the complete separation of the cold and hot subassemblies, which simplifies the requirements as to the thermal deformation of the large structures.

The Vacuum Topology of the Plasma Chamber. The toroidal system, consisting of the first wall, blanket, shield, and divertor plates, has been divided into two large parts: a semifixed shield and interchangeable sectors (Fig. 4). The parts subjected to the strongest

Declassified and Approved For Release 2013/02/06 : CIA-RDP10-02196R000300020002-8

Declassified and Approved For Release 2013/02/06 : CIA-RDP10-02196R000300020002-8

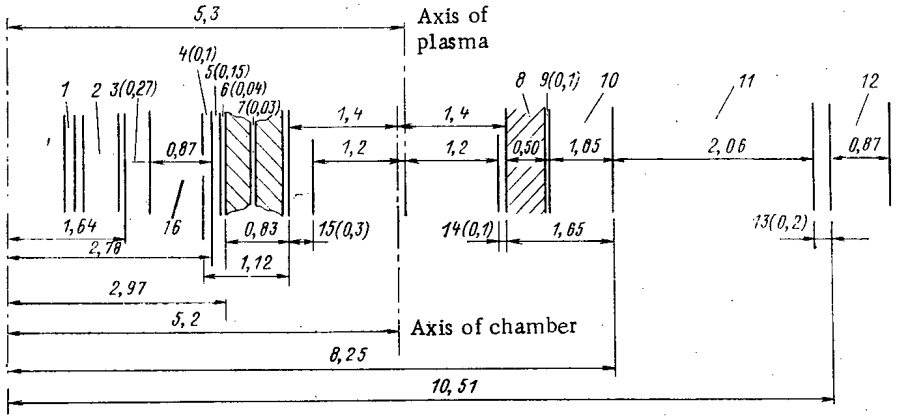

Fig. 5. Radial dimensions of INTOR: 1) starting winding; 2) solenoid; 3) support cylinder; 4) jacket of toroidal coil; 5, 13) sylphon bellows; 6) inner clearance; 7, 9) clearances; 8) blanket; 10) outer shield; 11) outer clearance; 12) toroidal coil; 14, 15) outer and inner divertor layers (all the dimensions in parentheses and without parentheses are given in meters).

effect of the stream of particles and heat (the first wall and the region of the blanket) have been combined into a sector which could be moved separately away from the toroidal shield. It is most important that the vacuum seal for this sector be entirely on the outer part of the torus. The welded seal, on a rectangular flange, between the outer supports of the TF coils is readily accessible for servicing. The other part of the torus, comprising the structural framework and the semifixed shield, forms the primary vacuum boundary and is not moved away during planned normal servicing procedures.

Single-Zero Poloidal Divertor. The divertor collector devices are the most subject to damage and, therefore, the design provides for their frequent repair. The modular divertor sector has been designed so that it could be moved away just as the main toroidal sector is moved away. A two-zero divertor offers only limited access to the upper part of the torus. For this reason the concept of a single-zero divertor has been chosen, regardless of the problems involved in producing an asymmetric poloidal field configuration and caused by the large particle and heat loads on the divertor plates.

In a divertor system with a single zero the divertor chamber is located in the lower part of the toroidal chamber. This has proved possible as a result of the displacement of the plasma upward by 0.6 m relative to the horizontal axis of the TF coils. In this case centered assembly of the toroidal and divertor chambers is possible inside the system of toroidal coils and servicing is facilitated. The configuration of the divertor region consists of 12 divertor modules (Fig. 4), arranged inside the removeable toroidal sector.

Support Design. Great efforts went into the design of the support configuration. The TF coils along with the PF coils generate very strong pulsed magnetic forces which act on the TF system. Thermal calculations show that the support structures should operate at cryogenic temperature. The structural form of the support structures, consisting of mechanically connected reinforced parts, was designed with allowance for the condition of maintaining the space necessary for removing the toroidal sector. The design was checked by means of three-dimensional calculations using a finite-element model. The model took account of the presence of all 12 TF coils and their support structure. In order to study the details of the design a local stress analysis was made with allowance for the local planar bending. Another feature of the structural configuration is the support system bearing the mass of the reactor. The supports of the magnet system are located on the outer side of the reactor so as to ensure access to the lower part of the reactor (see Fig. 3).

Radial Dimensions of the Tokamak. The spatial arrangement of all the reactor components and the required clearances for assembly of the separate units are shown in Fig. 5.

Assembly and Servicing. The INTOR reactor was designed with allowance for the requirements of assembly and remote servicing. An important factor in establishing these requirements is the frequency of equipment breakdown. The assumed numbers of repairs per year for

Declassified and Approved For Release 2013/02/06 : CIA-RDP10-02196R000300020002-8

Declassified and Approved For Release 2013/02/06 : CIA-RDP10-02196R000300020002-8

TABLE 2. Cooling System Parameters

Characteristics	Magnetic systems	Injector + rf system	Total
Cooling system power, kW	42.5 (helium) 1100 (nitrogen)	10.5 —	53 1100
Liquid-helium flow rate, liters·h^{-1}	1800	200	2000

some of the main components of the tokamak are given below:

Divertor, ion sources of injector . . . . . 2-10 (minor repair)
First wall, blanket (removable toroidal sector) . . . 1 (medium repair)
Magnets, shield (semifixed toroidal sector) . . . . . 0.1 (major repair)

The requirements associated with servicing of the equipment have been studied from the point of view of general transporting as well as in order to determine the role of manipulators and special equipment and inspection of the systems.

The magnetic and electrical systems are designed for the production of the necessary magnetic field configuration by the single-zero poloidal divertor and for providing the power supply to the main reactor systems.

System of TF Coils. The TF coils have been designed so as to permit use of one of the three main superconducting-cooling concepts under study in the world. The superconductor concepts considered were: hybrid NbTi/Nb_3Sn, cooled by immersion at 4.2°K; NbTiTa, cooled by superfluid helium at 1.8°K by the immersion method; and Nb_3Sn with forced cooling with liquid helium as an alternative. The first variant is based on cooling technology that has already been tried and tested in functioning devices. A drawback is the use of Nb_3Sn, which is a relatively brittle material and is difficult to fabricate. The second variant does not have this drawback. At a lowered cryogenic temperature it is possible to use NbTi, but the technology of producing superfluid helium has not been sufficiently tested. The third variant has substantial technical advantages over the other two: better heat removal from the conductor and a simpler method of insulation, but this variant is based on a technology which has not had sufficient practical testing. The choice from these variants will be made on the basis of experimental results in the development of the appropriate programs. Losses due to Foucault (or eddy) currents have been taken into account in designing the cryogenic system.

The system of PF coils was developed in connection with the requirement that the coils be positioned outside the TF coils. The PF coils are divided into three main groups:

a superconducting solenoid that is placed inside the supporting cylinder and performs the function of maintaining the current in the plasma and effecting the ohmic heating of the plasma;

a cryoresistive solenoid that is positioned coaxially inside the superconducting solenoid and serves to cause breakdown of gas in the tokamak as well as initiation and initial growth of the current in the plasma;

eight annular superconducting coils that are positioned above and below the TF coils and ensure that the plasma is maintained in equilibrium.

The system of PF coils is asymmetric relative to the median plane of the toroidal coils, as a consequence of the use of a single-zero poloidal divertor. The cross section of the annular superconducting coils is 1.5 × 1.5 m. The total current at the end of the burn pulse is 38 MA × No. of turns in the superconducting solenoid, 41 MA × No. of turns in the cryoresistive solenoid, and 60 MA × No. of turns in the eight annular superconducting coils. The fields and forces acting on the winding were calculated, and the distribution of the forces on the support structure was determined.

Two concepts of superconducting coils have been developed. One concept is based on the forced method of cooling the conductor, while the other is based on immersion cooling with liquid helium at 4.2°K. The choice of variant will be made after results of experiments on the appropriate test stands are obtained.

The ac power supply system provides the power necessary for the operation of INTOR and has a sufficient reserve for further development. The high-power line ensures a supply for the following reactor systems (in MW):

Declassified and Approved For Release 2013/02/06 : CIA-RDP10-02196R000300020002-8

Declassified and Approved For Release 2013/02/06 : CIA-RDP10-02196R000300020002-8

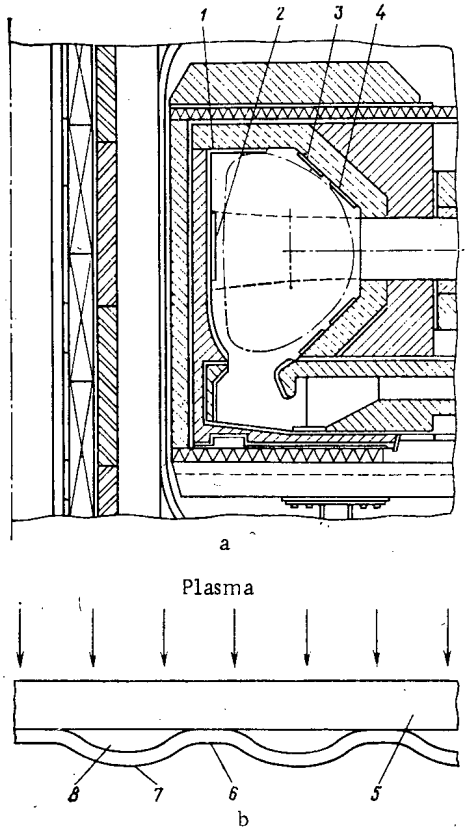

Fig. 6. Configuration of the first wall: a) poloidal section of the reactor; b) cross section of the first wall; 1) area of contact with plasma during tearing; 2) region of entry of neutral beam; 3) region of diaphram; 4) surface of emergence of particles due to corrugation of magnetic field; 5) first wall; 6) site of roller joint; 7) corrugated surface; 8) coolant.

Motor-generators	120
All cooling pumps	20
Cryogenic system	41
Vacuum system	5
Auxiliary heating (in foundation)	20
Tritium system	5
Burn control system	15
Auxiliary equipment	15
Total	241

An independent low-power line, at a lower voltage, supplies the respective systems even when the high-power line fails. Provision has been made for diesel generators to provide energy for the critical loads in cases when both lines fail.

The system for storing electrical energy reduces the peak power required in the transmission line. It uses power from the line during the burn phase of the operating cycle and from the inductive load of the energy converter of the poloidal magnetic field during the discharge phase and stores this energy for the pulsed loads of the next cycle. It is proposed to use the surge generator for large pulsed loads isolated from the power lines. Five surge generators with a stored energy of 4.5 GJ each are necessary for supplying the poloidal field system and the fast-atom injector. Each generator has a peak power of 800 MVA and the duration of the starting pulse is 5 sec.

The cryostat of the magnetic system is a vacuum volume in which all of the cooled structures are enclosed. Each coil has its own helium volume. Helium vapor cools baffles placed inside the vacuum volume to reduce the thermal fluxes from the surfaces which are at liquid-helium temperature. It is proposed, if necessary, to use compounds with a high electrical

Declassified and Approved For Release 2013/02/06 : CIA-RDP10-02196R000300020002-8

Declassified and Approved For Release 2013/02/06 : CIA-RDP10-02196R000300020002-8

resistance so as to reduce the induced toroidal currents. The cryogenic system of INTOR is based on the forced-cooling variant in which the TF and PF coils are cooled with liquid helium and includes two cooling circuits: a liquid-helium system, ensuring a temperature of 4-4.5°K for maintaining the superconducting coils in the working state and a liquid-nitrogen system at 80-95°K for cooling the cryoresistive solenoid and the baffles separating surfaces at 4 and 300°K. The liquid-helium system also serves to cool cryogenic panels in the neutral-beam injectors.

The cooled units have the following parameters. The mass of the structures cooled to liquid-helium temperature is 9000 tons; the mass of the structures cooled to liquid-nitrogen temperature is 150 tons; the area of the surface carrying off heat by radiation is 3000 m^2; and the length of the iron supporting structures is 1 m and their cross-sectional area is 2 m^2. The helium system should have liquefiers and refrigerators. The requirements placed on the cooling system are given in Table 2.

The heating and fuel makeup system is designed to heat the plasma to the ignition temperature of the D–T reaction and to provide a makeup supply of D–T fuel for it.

The Neutral-Beam Injector. Four injectors provide an injected power of 75 MW. An auxiliary injector is backup. Each injector contains six independent ion sources, the injection angle being from 16 to 22°. The width and height of the cross section that is formed by the intersection of each injector with the tokamak chamber were 1.0 and 1.2 m. The injectors are connected to the tokamak chamber by means of an absolute gate. A shield 1 m thick around the drift tube of the injector increases the area of the intersection of the injector with the tokamak to 9.6 m^2 for each injector. The width, height, and depth of the main injector casing are 6, 8, and 4 m, respectively. The mass of each injector is about 100 tons, while the mass of the shield surrounding the injector is about 350 tons. The shield is made so that the injector could be assembled and disassembled. The power supplies and auxiliary equipment (cryogenic refrigerators, control systems, cooling systems, etc.) are positioned outside the reactor hall. The gas efficiency of the ion sources is assumed to be 50%. Roughly 10^4 $Pa \cdot liter \cdot sec^{-1}$ of cold gas is pumped from the six ion sources by differential pumping of the chamber, carried out with cryogenic pumps with an area of 30 m^2 at a pressure of $1.33 \cdot 10^{-2}$ Pa and 64 m^2 at $5 \cdot 10^{-4}$ Pa. These pumps, of the cryogenic-condensation type, are covered with liquid-nitrogen cooled stripes. The atom guide ends with an absolute vacuum gate which is opened only during injection, thus reducing the flow of tritium and helium from the tokamak to the injector. An iron magnetic shield 15 cm thick surrounds the gas target chamber. This reduces the scattered magnetic fields of the tokamak to $\sim 8 \cdot 10^{-4}$ T in the region of the ion source and the gas target. The influence of neutron irradiation has been reduced by the presence of the shield and an appropriate choice of materials. The insulators in the source, in the system of the direct converter, and in the magnet are either covered or made of inorganic materials.

The fuel makeup system includes a system for admitting gas and injecting pellets, and ensures controlled admission of gas into the plasma of INTOR. Gas can be admitted by using all 12 special pipes, on which devices for admitting the gas have been installed, or by using some of them. The backup devices enable the system to be made reliable and flexible for a controlled supply of gas into the plasma chamber after appropriate purification. Two pellet injectors, which can inject deuterium and tritium pellets simultaneously, are installed on opposite sides of the torus. In principle, one injector can ensure satisfactory operation of the tokamak, although a more uniform density distribution in the toroidal direction can be attained with two injectors. The design value of the velocity of pellets from the injector into the tokamak plasma is $2 \cdot 10^3$ $m \cdot sec^{-1}$. Both the pneumatic and centrifugal methods of acceleration of pellets have been developed in fair detail and can be used in pellet injectors in both channels simultaneously.

The First Wall. The concept of the construction of a first wall (Fig. 6) that will function for the entire service life of the reactor has been developed in the INTOR design. The structure of the first wall includes an outer surface which is a substantial part of the surface of the plasma chamber and receives particle and heat fluxes from the plasma and radiation from the divertor; an internal region subject to the action of particles and radiation while the thermonuclear reaction burns in the plasma and receives the main part of the plasma energy during tearing instability; a diaphragm region on the outer part of the wall, confining the plasma filament in the initial stage of the discharge; part of the inner surface of the chamber, receiving atoms with the injection energy which pass through the plasma filament

Declassified and Approved For Release 2013/02/06 : CIA-RDP10-02196R000300020002-8

Declassified and Approved For Release 2013/02/06 : CIA-RDP10-02196R000300020002-8

TABLE 3. Operating Conditions of First Wall in Steady-State Regime of Reactor*

Region	Total thickness, mm	Maximum erosion, mm	Maximum temp., °C	Maximum stress, MPa	No. of pulses (with allowance for material fatigue)	
					without erosion	with erosion
Outer wall	11,7	8,7†	260	360	$3 \cdot 10^6$	10^7
Corrugated device	11,7	8,7†	297	400	$1 \cdot 10^6$	10^7
Diaphragm	12,8	9,8†	280	410	$8 \cdot 10^5$	10^7
Inner wall	13,5	10,5‡	275	408	$9 \cdot 10^5$	10^7
Region of beam reception	13,5	10,5‡	332	495	$2 \cdot 10^5$	10^7

*The maximum temperature is assumed to be 350°C; the maximum allowable stress is 650 MPa from the plasma side and 765 MPa from the coolant side.
†Physical sputtering.
‡ Physical sputtering + vaporization.

in the initial period of injection; and a region of the outer surface on which substantial particle fluxes impinge in the final stage of neutral injection as a consequence of the corrugation of the magnetic field.

The main variant of the first-wall design uses water-cooled stainless steel panels. The wall thickness in special regions, i.e., of the diaphragm and the inner part, is increased because of the great erosion of these portions. The structural material chosen is type 316 stainless steel, which ensures radiation resistance throughout the operation of the reactor. It is proposed to avoid corrosion-induced low-temperature cracking of the stainless steel by controlling the chemical composition of the water at low pressure. The thin-walled corrugated cooling channels of the panel structure of the first wall were chosen in order to reduce the flexural stresses and to increase the service life in comparison with tubes. The outer wall is part of the blanket and is capable of neutron multiplication.

The design presents calculations of the erosion rate and the required panel thickness for the various regions. The calculated rate of vaporization due to tearing instability is $8 \cdot 10^{-4}$ mm per tearing for an energy density of 289 $J \cdot cm^{-2}$, released in 20 msec. The extent of the erosion of the inner part of the wall (1.8 mm) during 15 years of reactor lifetime is obtained with an indeterminancy factor of 2. It is assumed that a thin molten layer ($\sim$140 μm) is formed on the inner part of the wall during a tearing and does not erode in $\sim$10 msec (Table 3).

Near cuts in the inner part of the wall, an erosion of up to 10% of the thickness of the molten layer ($\sim$0.14 mm/tearing) is assumed. As an alternative material for the first wall consideration was given to aluminum, which is attractive because of its high thermal conductivity and, therefore, lower thermal stresses. Preference was given to stainless steel in the design, however, mainly because of the large body of data about its properties, its extensive use in the worldwide fusion program, and its great capability for withstanding tearings.

An alternative variant of the first-wall concept is that of a radiation-cooled graphite liner, placed on the inner wall, with water-cooled stainless steel panels as the outer wall. The graphite liner consists of plates with an area of 30 cm^2 and a thickness of 4 cm, mounted on rails. In order to replace them a sector of the blanket with the shield must be moved away. The graphite liner functions at $\sim$1500°K and absorbs an additional power of 40 MW which is radiated to the outer and inner walls.

Divertor Collector Plates. The system chosen for eliminating impurities in INTOR is that of a single-zero poloidal divertor positioned in the lower part of the plasma chamber (see Fig. 3). Of the total of 80 MW of power arriving at the divertor, 70 MW impinges directly on the divertor plates. This means that the divertor collector plates operate under the most stressed conditions of all the subassemblies of the tokamak and they must be replaced several times during the lifetime of the reactor.

Declassified and Approved For Release 2013/02/06 : CIA-RDP10-02196R000300020002-8

Declassified and Approved For Release 2013/02/06 : CIA-RDP10-02196R000300020002-8

The collector plates are subjected to large thermal stresses with considerable temperature gradients, physical sputtering, and radiation damage in the form of swelling, embrittlement, and creep of materials. To reduce the effect of plasma flows, the inner plate is inclined at 30° and the outer plate at 14.5° to the separatrix. With this positioning of the plates the maximum density of the heat flux is reduced to 2 $MW \cdot m^{-2}$ and the maximum particle flux, to $1.5 \cdot 10^{22}$ $m^{-2} \cdot sec^{-1}$.

The two concepts of collector plates considered envisage shielding in the form of tungsten or molybdenum plates, which have the lowest sputtering coefficients and can be joined to a cooled stainless steel or copper backing. The shielding plates are sputtered under the effect of particles and, therefore, they must be replaced. The main difference between the concepts considered rests in the method of attaching the protective plates. In the first case, soldering is employed, ensuring high thermal conductivity between the plate and the cooled surface. The other concept is based on a mechanical method of attachment, leading to an uneven removal of heat from the protective plate.

When soldering is used, the temperature of the shielding plates is low, but their thermal expansion is limited by the existence of the joint. Compression of the soldered joints leads to large stresses and can cause cracking of the plates, seams, or the cooled backing. On the other hand, at the present time it is difficult to ensure the integrity ot the soldered joints during the entire operation of INTOR. Moreover, the copper backing is subjected to radiation fracture, which may limit its service life to 1 yr.

In the case of mechanical fastening, the shielding plates can rotate freely and expand when the temperature changes during a pulse. The plate thickness in this variant can be increased so as to extend their serivce life as far as sputtering is concerned. During an operating pulse the temperature of the shielding plates rises from 1600 to 2300-2500°C, at which 40-50% of the incident energy is reemitted to the divertor and plasma chambers. This reduces the temperature gradient in the shielding plates and the heat flux to the stainless steel backings, which are designed for the entire operating lifetime of the reactor. The main drawback of this variant is that of operation at a high temperature, which may lead to recrystallization and embrittlement. At high temperature the chemical sputtering by oxygen impurities may be large and may reach roughly 0.75 of the rate of physical sputtering. Both concepts are feasible but entail considerable uncertainties. Futher investigations are required in order to choose the final variant.

Tritium-Breeding Blanket. The concept of the INTOR blanket envisages the possibility of obtaining a considerable quantity of tritium.

From the engineering point of view it seems advisable to place the tritium blanket on the outer and upper parts of the INTOR chamber. In designing the blanket the minimum value of the tritium-breeding ratio was assumed to be 0.6. Solid and liquid materials were considered for the breeding of tritium. Solid materials have an advantage from the point of view of engineering simplicity and a relatively low stored chemical energy. The main problem pertaining to the use of solid materials lies in how the tritium is to be extracted. The greatest uncertainty is associated with the possible influence of radiation on the mechanism of tritium liberation. Ceramics are the solid materials that have the greatest potentialities for acceptable liberation of tritium.

The main variant of blanket design uses lithium metasilicate Li_2SiO_3, while Li_4SiO_4 is an alternative material. An alternative concept of a blanket with Li_2O and $Li_{17}Pb_{83}$ has also been developed. A lead neutron multiplier is placed in the blanket in order to reach the required tritium-breeding ratio. Structurally, the first wall is an inseparable part of the blanket. Water at low temperature is used to cool all parts of the blanket. Two blanket concepts have been chosen. The main difference between them is in the choice of moderator and in the positioning of the materials breeding tritium relative to the coolant. In the first concept (design 1) graphite is the moderator and the cooling tubes are surrounded by a lithium-containing material. In the second concept (design 2) water (H_2O) is the moderator while lithium-containing materials are placed concentrically on the outside of the cooling tubes. In both concepts the lead neutron multiplier is positioned between the first wall and the tritium-breeding region. Low-temperature water H_2O is used to cool the tritium-breeding region, while D_2O is employed to cool the first wall and the neutron multiplier. Below we give the main parameters of the tritium-breeding blanket:

Declassified and Approved For Release 2013/02/06 : CIA-RDP10-02196R000300020002-8

Declassified and Approved For Release 2013/02/06 : CIA-RDP10-02196R000300020002-8

	Design 1	Design 2
No. of blanket sectors	12	12
Neutron multiplier:		
material	Pb	Pb
thickness, cm	5	5
maximum temperature, °C	290	290
melting point, °C	327	327
coolant	H_2O	D_2O
Tritium-breeding region:		
breeding material	Li_2SiO_3	Li_2SiO_3
temperature (max/min), °C	600/400	600/400
effective filling density	0.7	0.7
fuel-element diameter, cm	4-6	6
^6Li enrichment, %	30	30
tritium-extracting gas	He	He
structural material	Type-316 stainless steel	
maximum temperature of structure, °C	150	150
coolant	H_2O	H_2O
coolant temperature (in/out), °C	50/100	50/100
coolant pressure, MPa	0.7	0.7
neturon multiplier	C	H_2O
thickness of tritium-breeding region, cm	43	26
effective covering with blanket	0.6	0.6
tritium-breeding ratio	0.65	0.65

In both designs tritium is extracted from ceramic materials by means of a stream of purified helium at low pressure (∿0.01 MPa). Design 2 is distinguished by several advantages: simplicity of assembly; a minimal charge of solid tritium-breeding material; and a thinner blanket because of the use of the most efficient moderator.

The total quantity of tritium in the blanket (200 g) is determined on the basis of data for the unirradiated material. As shown by theoretical estimates, this quantity can be increased to roughly 1 kg. The INTOR design, therefore, envisages the use of 0.5-1.0 kg tritium in the blanket.

Radiation Shielding. The radiation shielding of INTOR has been designed for the purpose of protecting the reactor components from extreme radiation damage and nuclear heating, reducing the level of activity induced in the reactor components, and shielding the operating personnel and the population from the radiation. The system of shielding by means of a local shield makes it possible for personnel to enter the reactor building 24 h after reactor shutdown. This system consists of a toroidal main shield, an auxilliary shield for the open parts of the torus not protected by the main shield, and the walls of the reactor building, which also serve as biological shielding.

The main shield is divided into an inner shield, positioned inside the torus, and an outer shield. The inner shield serves primarily to protect the central part of the superconducting magnet system. Its total thickness in the median plane from the plasma side of the first wall to the inner surface of the region of the toroidal magnetic coil is 1.1 m. Incorporated here are a region 40 cm thick that consists of stainless steel (90%) and water (10%) as well as a 34-cm region of boronized steel (60%) and water (40%). The real thickness of the shield, including the first wall and a 3-cm gap, is 0.85 m. Below we give the radiation conditions on the inner part of the toroidal magnetic coils under a neutron load of 1.3 MW·m^{-2} on the first wall and a total neutron fluence of 6 MW·yr·m^{-2}:

Maximum neutron fluence in superconductors, neutrons·cm^{-2}	$4 \cdot 10^{17}$
Maximum resistance of copper stabilizer, Ω·cm	$3 \cdot 10^{-8}$
Maximum No. of displacements per atom in copper stabilizer, displacements·$atom^{-1}$	$2.5 \cdot 10^{-4}$

Declassified and Approved For Release 2013/02/06 : CIA-RDP10-02196R000300020002-8

Declassified and Approved For Release 2013/02/06 : CIA-RDP10-02196R000300020002-8

Maximum dose in insulators, Gy:	
thermal insulator	$2.5 \cdot 10^7$
electrical insulator	$7 \cdot 10^6$
Maximum nuclear heat release in the superconductor, $W \cdot cm^{-3}$	$9 \cdot 10^{-5}$
Total power of nuclear heating, kW:	
12 TF coils	7
magnetic vacuum volume	9

The outer shield, 105 cm thick, has been designed to protect the individual components of the reactor and to provide access by the personnel when the reactor has been turned off. This shield and the 50-cm blanket are separated by a 10-cm gap. This makes it possible to reduce the biological dose rate to 2.5 mR/h (1 R = $2.58 \cdot 10^{-4}$ C/kg) on the outside of the main shield for 24 h after reactor shutdown. The main part of the outer shield (90% steel and 10% water), 70 cm thick, is placed beyond the blanket. Then comes a 28-cm-thick region of boronized steel and water and, finally, a 4-cm layer of lead. Steel with a low nickel content is used in order to reduce the induced activity.

Since the details of the design of the auxiliary shield have a considerable effect on the cost and operation of the reactor as well as on the requirements concerning personnel access, detailed calculations of neutron and photon transport during reactor operation and γ-ray transport after shutdown have been carried out. The calculations established that 3 kW of nuclear power is accounted for by a fraction of the vacuum pumps of the atom-injection system with the gate opened. In order to reach a biological dose rate of 2.5 mR/h in 24 h after reactor shutdown it is necessary to have an auxiliary 1-m shield for the atom guide connecting the injector to the tokamak; 0.75 m for the surfaces of the injector chamber and 0.5 m for the remaining parts of the injector and the divertor section are also necessary.

The Tritium and Vacuum Systems. The INTOR design provides for a complete deuterium–tritium–lithium cycle.

The tritium system ensures execution of the following functions with a minimum tritium content in the system and a minimum effect on the environment and the operating personnel: regeneration of tritium coming from the plasma chamber, storage of this tritium, and feeding into the plasma supply; tritium breeding in the blanket; extraction of the tritium from the blanket and feeding into the plasma supply system; purification of wastes and coolant to remove tritium; and monitoring of the quantity of tritium in all buildings. The tritium system should be shielded from γ rays and neutrons and should be designed for maximum reliability coupled with the best utilization factor.

The tritium circulation rate in the system during continuous operation is 1035 g/day in stage I and 1597 g/day in stages II and III, including the tritium bred and the external makeup. The quantity of tritium circulating in the plasma system is $\sim$200 g and to this we must add the 390 g of tritium present in the vacuum pumps, at the pelletizing sites, and in the blanket regeneration system. Upon assuming the amount of stored tritium to be 2300 g from calculation of 30 days of continuous operation and taking the amount stored in the blanket to be 0.5–1 kg, we find that the total quantity of tritium in the systems of INTOR is 3.4–3.9 kg.

The gases expelled from the plasma chamber are subjected to low-temperature rectification. At cryogenic temperature, the gas impurities, except helium, are deposited on the cooled surface and are separated. The purified fuel is redirected into the plasma supply system.

Tritium is removed from the blanket with a purified stream of helium in the form of T_2O. At first, in the tritium-breeding system all of the gas functions are converted into water on passage through a catalytic reactor. Then at cryogenic temperature the water is separated from the helium stream and is subjected to electrolysis. The liberated tritium is fed back into the plasma supply system.

An important problem is that of the penetration of tritium through the first wall and the divertor plates. The implantation of a large number of tritium atoms in the surface of the first wall in the absence of appreciable recombination may substantially increase the amount of tritium penetrating through the first wall into the coolant. Further investigations in this area are necessary.

Declassified and Approved For Release 2013/02/06 : CIA-RDP10-02196R000300020002-8

Declassified and Approved For Release 2013/02/06 : CIA-RDP10-02196R000300020002-8

In order to limit the total liberation of tritium to a level of 10-20 $Ci \cdot day^{-1}$ (1 Ci = $3.700 \cdot 10^{10}$ Bq), the coolant should be processed and should have a fairly low tritium concentration. The system is being designed so that the tritium content in the air in all the premises would be less than 5 $\mu Ci \cdot m^{-3}$. If necessary, triple confinement of the tritium in the system is employed. Double confinement is envisaged everywhere. A special ventilation system protects the surrounding space from tritium fallout. The total quantity of tritium discharged into the environment should not exceed 10 $g \cdot yr^{-1}$.

The Vacuum System of the Torus. The initial pressure in the toroidal vacuum chamber should be $1.33 \cdot 10^{-5}$ Pa. It is proposed to use heating and cleansing of the chamber. The vacuum chamber in assembled form is heated to 200-300°C. The maximum heating temperature is limited by the lead zone of the blanket. The inner surface of the vacuum chamber is cleaned of oxygen and carbon by a hydrogen discharge and is in a hot state. The effective pumping rate necessary for ensuring the initial pressure is $5 \cdot 10^{4}$ $liters \cdot sec^{-1}$. During the pause the pressure in the vacuum chamber reaches $4 \cdot 10^{-3}$ Pa in 20 sec at an effective pumping rate of $1.5 \cdot 10^{5}$ $liters \cdot sec^{-1}$.

During the burning of the reaction the helium concentration in the plasma is kept below 5%. In order to accomplish this, it is necessary to eliminate from the chamber about 1% of the helium atoms that emerge from the plasma. Estimates show that the effective helium pumping rate should be roughly $2 \cdot 10^{5}$ $liters \cdot sec^{-1}$. Thus, the requirements on the pumping system during burning of the reaction are decisive.

The pumping system of the toroidal chamber consits of 12 evacuating cells, symmetrically arranged about the reactor axis. Each cell is connected to the divertor chamber by means of piping with a 1 × 1.2-m cross section and a length of 9 m. In order to ensure an effective helium pumping rate of $2 \cdot 10^{5}$ $liters \cdot sec^{-1}$, each cell should have a pumping rate of $5 \cdot 10^{4}$ $liters \cdot sec^{-1}$.

The vacuum system of the fast-atom injector includes a vacuum chamber which contains a gas neutralizer and sorption pumps, high-vacuum and forepumps, valves, and measuring instruments. A source of positive ions is connected to the vacuum chamber of the injector. The vacuum system of the injector should ensure: an initial pressure of $1.33 \cdot 10^{-5}$ Pa; vacuum conditions in the ion sources, neutralizer, and the injection channel; as well as a minimum tritium flow from the discharge chamber into the injector; a possibility of replacing the ion source without disruption of the vacuum; measuring the pressure; and effecting vacuum blocking.

It is proposed that condensation pumps with liquid helium be used as the principal means of high-vacuum pumping. The rate of deuterium pumping by helium cryogenic panels is roughly 8 $liters \cdot cm^{-2} \cdot sec^{-1}$. The injector is provided with a differential pumping system, helium cryogenic panels installed in chambers separated by diaphragms. This system makes it possible to reduce the area of the cryogenic panels to 45-50 m^2. The pumping rate in each injector is $(3 - 4) \cdot 10^{6}$ $liters \cdot sec^{-1}$. In order to obtain the initial pressure and to evacuate the vacuum chamber during regeneration of the cryogenic panels use is made of turbomolecular and mechanical fluid-free pumps.

Diagnostics, Data Acquisition, and Control. A preliminary study has been made of means of plasma diagnostics, technological cycles, and control systems. Two qualitatively different systems have been distinguished: a system of controls and means of plasma disgnostics and a system of acquisition of data about the parameters of the technological and electrical equipment.

Plasma diagnostics, in comparison with that existing in tokamaks, should be developed for the operating conditions in the field of thermonuclear neutrons of D–T plasma. The operation of the technological and electrical equipment in INTOR must be controlled at a higher level than in previous tokamaks. Some of the means of controlling the technogical systems can be taken from other areas: radiation detection — from nuclear reactors; control of the magnetic system — from high-energy physics; etc. Further efforts are necessary, however, to create combined systems for controlling the reactor operation.

An automatic control system is envisaged for controlling the reactor complex by means of feedbacks. Underlying the construction of the control system is the principle of adaptive operation of the individual systems and the entire complex as a whole so as to ensure high operating reliability of the system and to attain optimum regimes of the operation of the complex.

Declassified and Approved For Release 2013/02/06 : CIA-RDP10-02196R000300020002-8

Declassified and Approved For Release 2013/02/06 : CIA-RDP10-02196R000300020002-8

TABLE 4. Schedule for the Design and Construction of INTOR

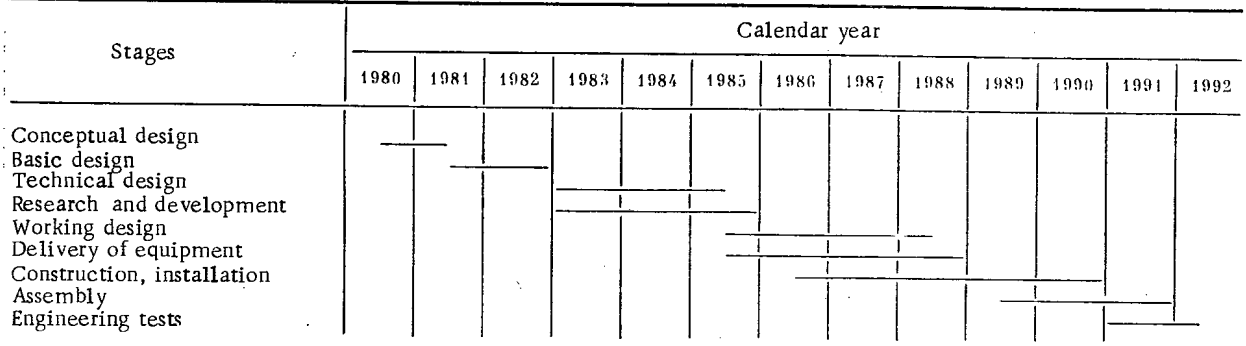

Note. The decision as to construction will be made in mid-1985.

Criteria for the Selection of the Site and Arrangement of Equipment. The following principal criteria must be taken into account in choosing the reactor construction site:

availability of a plot of land sufficiently large for the site of the reactor building and the servicing systems, at some distance from any populated region (the population density in the environs should be low);

fulfillment of the pertinent seismic requirements;

an appropriate electrical supply system for the complex;

existence of water resources for the cooling systems;

possibility of building a storage facility for radioactive waste, large units for equipment, and weakly tritiated water;

fulfillment of the safety requirements during accidental discharge of tritium;

availability of manpower for the construction and operation of the reactor and appropriate living quarters and conveniences;

possibility of transporting oversize loads during construction of the reactor, transferring tritium during the reactor operation, and transporting personnel daily and during trips abroad;

proximity of well-developed industry for the assembly of the reactor.

The conceptual design of the INTOR complex was elaborated in order to determine the main dimensions of the buildings and the requirements placed on them. The boundaries of the radioactive zone and the layout of the equipment have been established. Equipment is arranged about the toroidal chamber as follows: four operating fast-atom injectors and one backup occupy the space of five torus sectors between the toroidal field windings, while two injectors for fuel makeup to the plasma are arranged in two sectors. Three sectors are occupied by test modules and two sectors are earmarked for the diagnostics and control systems. Each of the 12 sectors is furnished with a pumping stem and a pump for removing gas from the divertor chamber.

PROGRAM OF REACTOR TESTS AND OPERATION

The design project presents a program of INTOR tests which determines the program of reactor operation with allowance for the fact that it is being built on an international basis. The plasma physics tests are aimed at problems which cannot be solved on other devices — a study of the behavior of plasma during a prolonged reaction. The plasma engineering tests consist in investigating methods of plasma heating, including rf heating. Testing the blanket consists of testing the prototype of a blanket module with an area of 1 m^2, investigating the process of tritium extraction, and determining the service life of the stressed elements of the blanket. In the materials testing program it is necessary to obtain information about the principal and alternative variants of materials, about materials operating under large thermal loads, and about insulators and tritium-breeding materials. The length of such tests is determined by requirements necessary for the functioning of the first wall and the blanket of the demonstration power reactor. In order to satisfy these requirements, it was decided to change the specimens after bombardment with neutrons at a fluence of 4, 10, 30, 50, and 100% of the neutron fluence 6.6 $MW \cdot yr \cdot m^{-2}$ adopted in the INTOR

Declassified and Approved For Release 2013/02/06 : CIA-RDP10-02196R000300020002-8

Declassified and Approved For Release 2013/02/06 : CIA-RDP10-02196R000300020002-8

design. After tests on the surface properties of the materials, information will be obtained about the operation of the divertor plates, the limiter, and the first wall. It is proposed to use roughly 5000 specimens of different materials with an area of 1 cm^2 each. The neutron tests will be carried out in order to measure the tritium-breeding ratio, the nuclear heating, the reaction rate, and the neutron and γ-ray spectra, as well as the induced activity.

A demonstration of electricity production on a special blanket sector set up during assembly of the reactor is proposed for the end of stage II and the beginning of stage III. At the end of stage III it will be possible to produce tritium and electricity simultaneously on a blanket sector serving as a prototype of the demonstration power reactor.

SAFETY AND THE ENVIRONMENTAL IMPACT

The aim of the present section in the INTOR design project is to evaluate the possibility of building a reactor so that its operation would not pose any significant risk to the personnel and the environment.

Radioactive Sources. The total tritium content in INTOR is 3.4-3.9 kg. Of this, about 2.3 kg is in store and 0.5-1.0 kg is in the blanket. A tritium discharge into the atmosphere during an accident is most likely from the plasma chamber, the vacuum system, and the system of fuel makeup to the plasma, i.e., an amount of 0.6 kg.

The induced activity of the structure and equipment surrounding the plasma chamber, the cooling system, and the atmosphere of the reactor building ranges from $3.2 \cdot 10^8$ to $1.3 \cdot 10^9$ Ci after extinction of the reaction. A large part of the activity is accounted for by the first wall: $(4 - 10) \cdot 10^7$ Ci$\cdot m^{-3}$. The most radioactive nuclides are ^{55}Fe, ^{56}Mn, ^{51}Cr, ^{58}Co, and ^{54}Mn, which are contained in stainless steel. The cooling water loop contains a small part (24-70 Ci) of the total activity, which is caused by corrosion or sputtering products of the stainless steel. Moreover, the water coolant will contain a large amount of ^{16}N (roughly 10^6 Ci$\cdot m^{-3}$). Because of its short lifetime, however, its content does not pose any serious problem. Estimates have been made of the ^{41}Ar concentration in the atmosphere of the reactor hall during operation. After shutdown of the reactor this concentration falls off rapidly as a consequence of the short lifetime.

Energy Sources and Possible Accidents. The design considers the most important energy sources which in the event of an accident may lead to a tritium discharge into the atmosphere. The greatest source of stored energy is the superconducting magnet toroidal field system ($\sim$40 GJ). Various scenarios of breakdowns of the magnet system and possible consequences have been considered.

Analysis of the possible consequences when the coolant is completely cut off in the blanket and in the first wall shows that roughly 300 sec are required, with the reaction proceeding continuously, for melting of the first wall to occur. In this time it is possible to take measures to protect the first wall from fracture. A high probability of melting exists for the zone of the lead neutron multiplier in the blanket. The design should, therefore, provide for measures against melting of the lead zone.

Estimates show that the probability of a hydrogen explosion is low. The concentration of hydrogen isotopes in the plasma in the worst case can be one or two orders of magnitude smaller than the value that leads to danger of an explosion (4%).

The INTOR plasma contains roughly 0.23 GJ of thermal energy. During a tearing instability, in 20 msec energy with a density of 289 J$\cdot cm^{-2}$ is released on the first wall, a layer $\sim$0.14 mm thick melts, and $\sim$1% of the material of this layer vaporizes. By the end of the operating time of the reactor the thickness of the first wall is 4 mm, i.e., the probability of of fracture of the first wall because of tearings is low.

There is some likelihood of the cryogenic system developing a leak and releasing helium into the reactor building. In this case the pressure in the building may increase by roughly $3 \cdot 10^4$ Pa, which is not dangerous for the designed building.

Radioactive Discharges and Their Consequences. In normal operation the discharge of tritium owing to diffusion and escape through leaking seals ranges from 10 to 20 Ci$\cdot day^{-1}$, according to estimates. It turns out that such a tritium leak does not result in the ground-level dose of 5 mR$\cdot yr^{-1}$, established for the population, being surpassed at a distance of 800 m or more.

Declassified and Approved For Release 2013/02/06 : CIA-RDP10-02196R000300020002-8

Declassified and Approved For Release 2013/02/06 : CIA-RDP10-02196R000300020002-8

The consequences of large discharges were evaluated for a 10-g discharge in the form of the oxide. Indeed, the tritium purifying systems will reduce a discharge into the atmosphere from the building by several orders of magnitude. A tritium discharge of 10 g gives a ground-level dose below the maximum value (25 R) for single events at a distance of 400 m or more. Assessment of all possible accidents leading to a discharge of activated products gave a dose of about 1%, or less, of the dose arising during the discharge of tritium under conditions of ordinary operation.

SCHEDULE FOR THE DESIGN AND CONSTRUCTION OF INTOR

As far as deadlines are concerned, the schedule (Table 4) is fairly tight, but is considered to be feasible provided there are not delays associated with the decisions of the governments concerning the construction of INTOR. It is proposed that the indicated research and development program, providing the basis for the design, will be carried out at the same time.

RESEARCH AND DEVELOPMENT

The program of research and development necessary for the design, construction, and operation of INTOR was considered in the zero phase of the design project [1]. This program was developed in greater detail in phase I and was supplemented with technological problems, whose solution is necessary for the construction of a tritium-breeding blanket.

CONCLUSIONS

The conceptual design for INTOR can serve as a basis for the technical design. The design has been drawn up with some margin in the parameters so that present uncertainties in plasma physics and technology would not significantly change the solutions adopted in the design after further research and development in the nearest future. The design has made it possible to reveal problems which must necessarily be solved in order to build an experimental thermonuclear reactor. Work on the design has reached a stage such that the solution of technological and engineering problems depends on the details of the design. It has become necessary to optimize the design in regard to all of the main subassemblies by working it out in greater detail.

The work of the International INTOR Group in phase I made it possible to focus the attention of the scientific community on the solution of the most important problems of both existing tokamaks and those being built. The design gains much by being developed on an international basis. It concentrates all of the latest world advances in the domain of plasma physics and engineering and technological developments for fusion reactors. It constitutes an example of fruitful international cooperation of scientists and engineers which enabled the zero and first phases to be carried out in a short time (2.5 yrs). In respect of the level of execution the design surpasses all existing national designs for fusion reactors.

LITERATURE CITED

1. INTOR Group, "International Tokamak Reactor — Zero Phase," IAEA Report, Vienna (1980); Yad. Sintez, 20, No. 3, 349 (1980).
2. G. Grieger et al., European Contributions to the INTOR Workshop. EUR FUBRU/XII 501/79/EDV-50, EUR FUBRU/XII 501/79/EDV-60, Brussels (1979).
3. B. B. Kadomtsev et al., USSR Contribution to the INTOR Workshop — 1979, Kurchatov Institute Report, Moscow (1980).
4. S. Mori et al., Japanese Contribution to the INTOR Workshop — 1980, JAERI Report, Tokai-Mura, Japan (1980).
5. W. Stacey et al., US Contribution to the INTOR Workshop — 1979, US INTOR Report, Georgia Institute of Technology, Atlanta, Ga. (1979).
6. B. B. Kadomtsev, Problems of Atomic Science and Engineering. Series "Thermonuclear Fusion" [in Russian], No. 1(15), 3 (1980).
7. EC Conceptual Design Contribution to the INTOR Phase-I Workshop, EC Report, Brussels (1981).
8. Japanese Conceptual Design Contribution to the INTOR Phase-I Workshop, JAERI Report, Tokai-Mura (1981).
9. USA Conceptual Design Contribution to the INTOR Phase-I Workshop, Report INTOR/81-1, Georgia Institute of Technology, Atlanta, Ga. (1981).

Declassified and Approved For Release 2013/02/06 : CIA-RDP10-02196R000300020002-8

Declassified and Approved For Release 2013/02/06 : CIA-RDP10-02196R000300020002-8

10. USSR Conceptual Design Contribution to the INTOR Phase-I Workshop, Kurchatov Institute Report, Moscow (1981).
11. INTOR Group, "International Tokamak Reactor — Phase One," IAEA Report, Vienna (1982).

COOLING CONDITIONS OF THE REACTOR OF THE BELOYARSK NUCLEAR POWER STATION FIRST UNIT DURING SHUTDOWN OF THE STATION AND DEPRESSURIZATION OF THE EVAPORATIVE CIRCUIT

P. A. Gavrilov, V. G. Zakharov,
G. A. Zvereva, A. I. Ionov,
V. D. Kozyrev, V. I. Mikhan,
Yu. I. Mityaev, T. D. Ogina,
L. N. Podlazov, N. Z. Rybakov,
A. G. Sheikman, and S. V. Shirokov

UDC 621.039.58

An analysis of the dynamics of the processes in the case of emergency situations with shutdown of the station and depressurization of the circulatory circuit allow the conditions of heat removal in the core to be determined in these regimes (reserves up to limiting power, fuel element temperature), and recommendations to be formulated for the assurance of the safe operation of the AMB-200 reactor, which has two main (MCP) and two emergency (ECP) circulatory pumps in each of the two circulation loops [1].

The investigation of an emergency situation associated with total shutdown of the facility is an essential part of the work carried out for substantiating the safety of the Beloyarsk nuclear power stations. In the computational investigations of this emergency, the results of which are presented below, experimental data on the switching-off of the MCP in the Beloyarsk nuclear power station (Fig. 1) and data on a mechanical breakdown of the turbogenerator used for powering the electric motors of the circulator pumps were used. In the case of triggering of the scram system, the experimental data on the transit time of the signal to the equipment and to the control and safety system logic were used.

Experiments on tripping the MCP were conducted at a power of 35-45% of the nominal. Before the start of each experiment, stabilization of the thermotechnical parameters of the reactor and the unit as a whole was carried out for 15-30 min, and loop oscillographs were prepared, having recorded on photographic film the variation of the coolant flow rate and other characteristics of the power generating unit (power, reactivity). After stabilization, the physical and thermotechnical parameters of the unit were recorded and then the MCP were switched off [2] simultaneously with the start of closure of the slide valve at the pump outlet. As a result of this, the flow rate in the circuit changed abruptly over 2-3 sec. In order to ensure nuclear safety and to prevent functioning of the scram system, simultaneously with switching off the MCP, two rods of the standby automatic regulator, operated in the manual regulation regime were inserted to a specified depth in the core [2].

When studying the variation of the coolant flow rate after switching off the MCP, it was established that in the cooling reactor the flow rate decreases smoothly without pulsations. In this case, by switching off one MCP in each loop, i.e., two per reactor, a stable flow rate is established over 3.5 sec, and when two MCP in each loop are switched off, i.e., four per reactor, the flow rate attains a zero value over 3.6 sec. When the MCP are switched off at power, the change of the flow rate has a more complex nature. Three seconds after switching off one MCP in each loop, the flow rate reaches a minimum, and then increases smoothly and after 8 sec becomes stable. The minimum flow rate through the evaporative circuit when one MCP is switched off in each loop at power attained 20% of the initial value. Later it rose to 36% of nominal.

In the numerical scheme of the facility, one of the two technological evaporative loops of the reactor with a superheat system is considered [1, 2]. The main plant of the circuit

Translated from Atomnaya Énergiya, Vol. 54, No. 2, pp. 98-100, February, 1983. Original article submitted March 18, 1982.

0038-531X/83/5402-0103$07.50 © 1983 Plenum Publishing Corporation

Declassified and Approved For Release 2013/02/06 : CIA-RDP10-02196R000300020002-8

Declassified and Approved For Release 2013/02/06 : CIA-RDP10-02196R000300020002-8

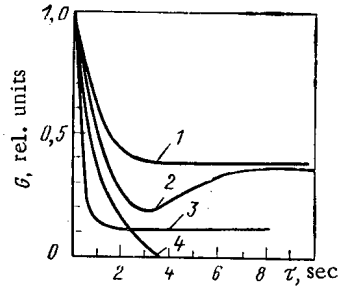

Fig. 1. Change of flow rate through the evaporative circuit when the MCP are switched off: 1, 2) one MCP in each loop switched off in reactor cooling and with 44% power, respectively; 3, 4) all 4 MCP switched off in reactor cooling with simultaneous switch-on of the 4 ECP, and only switch-off of all 4 MCP, respectively.

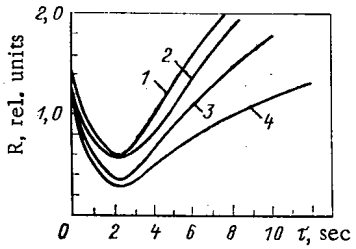

Fig. 2. Reserves $R = N_{lim}/N$ up to limiting power of maximally located EC, when the MCP are switched off: 1, 2) one MCP switched off and the turbogenerator maintained at coasting by one MCP in each loop for EC-5 and EC-6, respectively; 3, 4) all 4 MCP switched off, with simultaneous switch-on of 4 ECP for EC-5 and EC-6, respectively.

is listed: separator, descending channel, MCP subassembly, distributing collector, and evaporative channels (EC) and their communications. The superheat system was described as the superheat channel with communications from the separator to the stream takeoff at the turbine. In accordance with the normal electric power supply system for the inherent requirements of the unit, it was assumed that the MCP are fed from busbars, supplying voltage from the turbogenerator unit through a transformer. The mathematical description of the facility and the numerical programs on the computer were based on theoretical requisites for choosing the basis of the mathematical models of reactor dynamics, explained in [3].

The calculations performed on the basis of the experiments on the change of coolant flow rate when the MCP is switched off allow the cooling conditions of the EC to be estimated in the station shutdown cycle. In the calculations the duration of the crisis was determined from the time of exceeding the limiting power of the EC. When the MCP is shut off, the coolant circulation continues for a few seconds because of coasting of the MCP, and then it continues with the emergency circulatory pumps, which 2 sec after shutdown develop nominal efficiency. Because of the nonconformity between flow rate and power, no noncritical cooling of the channels is provided during 4-8 sec.

The time of stay of the EC of the reactor in the critical regime of heat removal during operation of the ECP amounts to (Fig. 2) 5.5 sec for EC-5 (five-element channels) and 8 sec for EC-6 (six-element channels). The crisis condition of the heat transfer is dependent upon a positive steam reactivity coefficient, because of which the power of individual EC becomes higher than limiting as a result of the coolant flow rate having been reduced at this instant to its minimum value.

Because all types of EC enter the crisis cooling cycle, the permissible level of the temperature increase of the fuel elements is used as a safety assessment criterion of this cycle. Data are given below of a calculation of the fuel-element outer-casing temperature

Declassified and Approved For Release 2013/02/06 : CIA-RDP10-02196R000300020002-8

Declassified and Approved For Release 2013/02/06 : CIA-RDP10-02196R000300020002-8

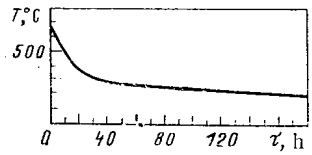

Fig. 3. Cooling of the graphite masonry of the reactor in the case of breakdown of the distribution water collector (T is the maximum temperature of the masonry).

for maximally loaded EC for the worst case during transition after switching off the MCP to operation with the ECP — the temperature before shutdown and the maximum temperature in the crisis, °C are given:

EC-5.	.375	550
EC-6.	.360	520

Taking account of the brevity of the arrival at crisis, this increase of temperature of the casing can be assumed to not exceed the permissible values in emergency situations [4].

An experiment was carried out at the Beloyarsk nuclear power station with an electric power of the turbogenerator of 7 MW, using coasting of the turbogenerator for supplying electric power to the MCP. Before the start of the experiment, the thermotechnical parameters of the power generating unit were stabilized during 20 min, after which the air cut-out of the 110 kV turbogenerator was tripped and the reactor was shut down by the scram system. The shutoff value of the turbine was closed after 20 sec by the normal circuit. As a result of this, the intrinsic requirements of the unit were provided by the coasting of the turbogenerator. The nature of the change of flow rate was recorded with a loop oscillograph. Experiments on the use of turbogenerator coasting for supplying power for two MCP of different loops during an emergency with shutdown of the station showed that the flow rate is reduced smoothly to 40% of the nominal, 100 sec after switching off the air cut-out. In this case during the first 20-25 sec the coolant flow rate through the EC was not below nominal. When using turbogenerator coasting for supplying power to the MCP motor, all the EC are cooled by the coolant during 100 sec, the flow rate of which significantly exceeds the flow rate during operation of the ECP.

It was established in the numerical investigations that by using the coasting of the turbogenerator for feeding one MCP in each loop — two per reactor — the EC in 4-5 sec briefly enter a heat-removal crisis (see Fig. 2). In this condition, as mentioned above, the temperature of the fuel element casings exceeds the permissible values.

An accident with breakdown of the distributing collector is the most serious from the point view of ensuring the temperature conditions of the core. In this case the pressure in the collector becomes less than the pressure in the separator, and leads to reversal of the circulation, operation of the check valves in the outlet circuits of the EC, and to their almost instantaneous steaming. The evaporative circuit is rapidly dehydrated (after 12-30 sec). The increase of the steam content causes an increase of the reactivity and power of the reactor. Owing to the special structural features of the normal EC in conditions of total stoppage of the circulation, a simultaneous heating up of the fuel elements and the graphite masonry occurs due to residual heat release.

In the numerical investigation of this hazard it was assumed that the scram system operates by the period or exceeding the power setting, and that the heating up of the fuel elements at the start of development of the hazard takes place adiabatically. After the fuel elements of the normal EC have heated up to a temperature equal to the average temperature of the graphite masonry 630°C (not before 15 sec), a further change of temperature of the EC takes place quasistationarily together with the graphite masonry of the reactor. Because of the drain of heat to cooling the zone of heating, acceptable cooling conditions are ensured (Fig. 3) as a result of the alternation of the numbers of evaporative and superheat channels of the reactor core.

LITERATURE CITED

1. P. I. Aleshchenkov et al., At. Energ., 16, No. 6, 489 (1964).
2. V. P. Andreev et al., At. Energ., 50, No. 6, 381 (1981).

Declassified and Approved For Release 2013/02/06 : CIA-RDP10-02196R000300020002-8

Declassified and Approved For Release 2013/02/06 : CIA-RDP10-02196R000300020002-8

3. I. Ya. Emel'yanov et al., Control and Safety of Nuclear Power Generating Reactors [in Russian], Atomizdat, Moscow (1975), p. 12.
4. N. A. Dollezhal' et al., in: Experience in the Operation of Nuclear Power Stations and the Course for Further Development of Nuclear Power Generation. Report of the Anniversary Obninsk Conference [in Russian], Vol. 1, Physicopower Institute (1974), p. 149.

A TEST OF CORRELATION MEASUREMENTS OF THE FLOW RATE OF SODIUM IN THE BN-600 ASSEMBLY

L. A. Adamovskii, V. G. Vysotskii,
V. V. Golovanov, V. V. Golushko,
V. N. Efimov, B. V. Kebadze,
É. P. Kozubov, and V. I. Kupnyi

UDC 621.039.564.5

The measurement of the sodium flow rates in the heat-transfer loops of a reactor has become a serious problem with the development of fast power reactors using sodium coolant. The electromagnetic primary transducers (magnetic transducers) used for this have, along with the known merits (inertia-free, absence of contact with the flow, convenience in combination with secondary devices, and so forth), a number of significant inadequacies associated mainly with the difficulties of their operational calibration and verification [1].

The necessity of providing direct measurements of the flow rate and calibration of regular flowmeters at the operating site has become especially evident during the period of start-up adjustments and power-up of the BN-600. The problem has been solved by the correlation method using magnetic transducers [2]. The essence of the method reduces to recording the average time for hydrodynamic inhomogeneities of the flow to cover the distance between detectors, for which identical magnetic transducers are used which are mounted on a straight section beyond the local hydraulic drag — a bend in the piping, a gate, a valve, etc. (Fig. 1). Small random fluctuations of the signals from the magnetic transducers which are correlated with the passage of hydrodynamic inhomogeneities enter into the calculation of the mutual correlation function after amplification and shaping; the time to transport the sodium between the first and second cross sections is determined from the shift in the maximum of the correlograms on the time delay axis.

The basic positions to be calibrated were the bypass line of the reactor with IRMU-50 flowmeters* (four positions, first circuit) and sections of the steam generators (SG) with IRMU-300 flowmeters mounted at the exits from the evaporators (24 positions, second circuit). The bypass line of the reactor contains a calibrated nozzle which accounts for ∿95% of the hydraulic drag of the bypass; therefore, one can indirectly estimate the accuracy of the hydraulic calculation of the first circuit by measuring the flow rate in this line.

It is important for SG to measure the total flow rate, which is necessary for estimation and comparison with the calculation of the hydraulic characteristics of the pump and circuit as a whole, and to control the cross-sectional distribution of the flow rate. The parameters of the measuring sections (see Fig. 1) were selected on the basis of experience from correlation measurements on similar BOR-60 piping and sodium test stands [2]. Regular and auxiliary IRMU-300 flowmeters identical to them served as the transducers.

The signals were processed by a 100-channel polar correlometer implementing an algorithm for calculating the sign mutual correlation function

$$\mu(\tau) = \frac{1}{T}\int_0^T \operatorname{sign} x(t) \operatorname{sign} y(t+\tau)\, dt,$$

where x(t) and y(t) are the variable components of the signal of the first and second magnetic transducers, respectively;

*IRMU-50 — a magnetic unified flow rate indicator for piping 50 mm in diameter.

Translated from Atomnaya Énergiya, Vol. 54, No. 2, pp. 100-103, February, 1983. Original article submitted April 26, 1982.

 0038-531X/83/5402-0106$07.50 © 1983 Plenum Publishing Corporation

Declassified and Approved For Release 2013/02/06 : CIA-RDP10-02196R000300020002-8

Declassified and Approved For Release 2013/02/06 : CIA-RDP10-02196R000300020002-8

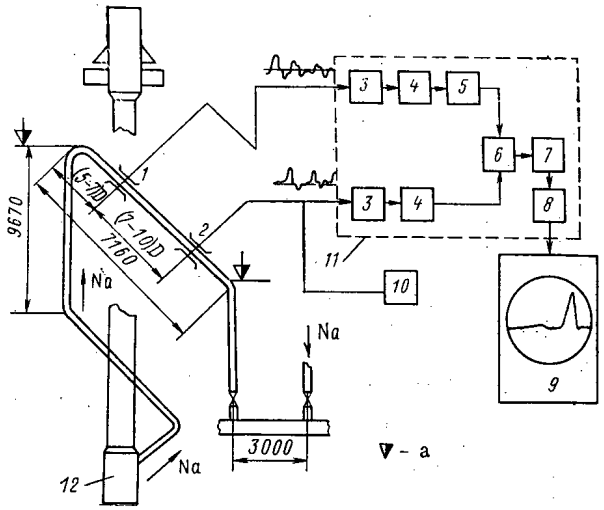

Fig. 1. Schematic diagram of the measurements: 1, 2) magnetic transducers; 3) unit for analog processing of the signal (filtering, amplification); 4) shaper of the polar signal; 5) shift register; 6) logic multiplication unit; 7) memory accumulator unit; 8) digital-analog converter; 9) oscillograph; 10) potentiometer for measurement of the signal of the regular flowmeter; 11) polar correlometer; 12) evaporator of the steam generator (D is the inner diameter of the piping, D = 300 mm; a) identical height markings of the levels).

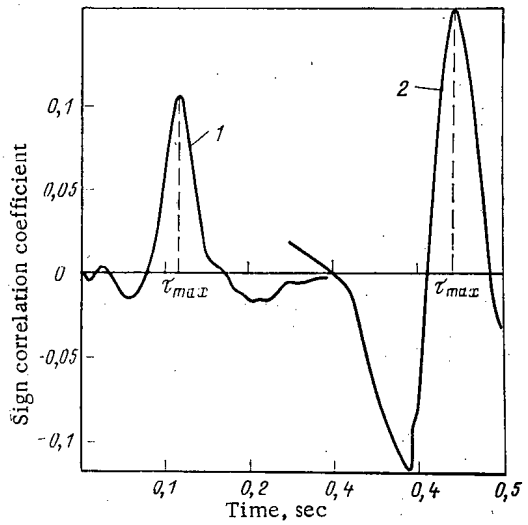

Fig. 2. Examples of measured correlograms: 1) bypass line of the reactor, D = 50 mm, L ≈ 6D, G = 17.5 m^3/h; 2) section B4 of steam generator 1, D = 300 mm, L ≈ 8D, G = 1670 m^3/h.

$$\operatorname{sign} x(t),\ \operatorname{sign} y(t) = \begin{cases} +1 & \text{for } x(t),\ y(t) > 0, \\ -1 & \text{for } x(t),\ y(t) < 0; \end{cases}$$

τ is the time delay, and T is the collection time of a correlogram.

The flow rate has been measured and flowmeters have been calibrated as the appropriate circuits and loops were activated. In the majority of cases programs of correlation measurements were combined with programs for rolling the equipment, flushing the active zone with a sodium flow, and determining the hydraulic characteristics of the circuits.

Unfortunately, the correlation flowmeters in the SG sections were not equipped with auxiliary magnetic systems. However, subsequent preparation, filling with sodium, and rolling

Declassified and Approved For Release 2013/02/06 : CIA-RDP10-02196R000300020002-8

Declassified and Approved For Release 2013/02/06 : CIA-RDP10-02196R000300020002-8

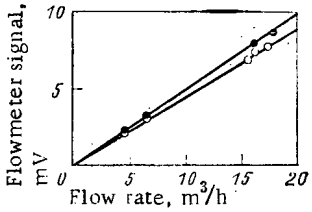

Fig. 3

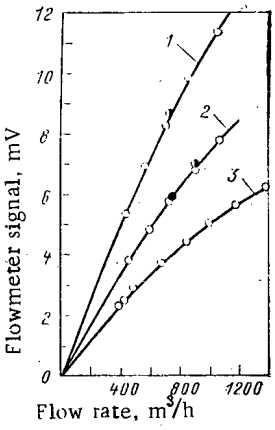

Fig. 4

Fig. 3. Calibration characteristics of the first (●) and second (○) hanging magnetic flowmeters of the bypass line.

Fig. 4. Calibration characteristics of the IRMU-300: 1) section B3 of steam generator 3; 2) section B4 of steam generator 2; 3) section B1 of steam generator 2; ○ — calibration at T_{Na} = 250°C; ●, ◑ — checks at T_{Na} = 340 and 310°C, respectively.

of the loops of the second circiut permitted using the regular magnetic systems of the third loop as auxiliary ones for correlation measurements in the first and second loops. Four reserve IRMU-300 magnetic systems were used for the measurements in the third loop.

The principal measurements in the first and second circuits were made at a sodium temperature of 250°C; the control measurements were made at 310 and 340°C. At each stage (the flow rate was regulated by the number of pump revolutions) there was a delay of 10-15 min to stabilize conditions. A triple set of correlograms was made to raise the reliability; the position of the maximum was controlled to an accuracy of half a channel; the cycle interval was varied until a maximum was found in the region of channels 70-90. Examples of measured correlograms are given in Fig. 2. The flow rate, to which the average emf of a regular flowmeter was taken to correspond, was determined from the transport time τ_{max}.

If the calibration characteristic of the flowmeters of the bypass line (Fig. 3) is practically linear, then the characteristic of the IRMU-300 (Fig. 4) is significantly nonlinear for a flow rate greater than 500 m^3/h and requires specified approximations to describe flow rates over the entire range of flow rates and setting up the scale of secondary devices. The main reason for the nonlinearity is a distortion of the primary magnetic field near the ends of the magnetic field zone due to induced currents [3]. This distortion is expressed in a drift of the magnetic field along the flow, and the higher the magnetic Reynolds number is, the more strongly it is exhibited. For nominal flow rates through sections of the SG (G = 1000 m^3/h) $Re_m \approx 15 \gg 1$, which for a relatively small length of the plate which equalizes the magnetic field creates the prerequisites for the appearance of an end effect and nonlinearity of the characteristics.

The form of the approximation dependence can be indicated on the basis of the assumption that the distortion of the primary magnetic field by induced currents is proportional to the induced emf:

$$E = kG(B_0 - \alpha E),$$

where B_0 is the induction of the primary field, and k and α are proportionality coefficients. From this we get

$$E = kB_0G/(1 + k\alpha G).$$

It is evident that as $G \to \infty$ the induced emf tends to some limiting value $E_{lim} = B_0/\alpha$. If the operating characteristic is nonlinear but sufficiently far from saturation, which is

Declassified and Approved For Release 2013/02/06 : CIA-RDP10-02196R000300020002-8

Declassified and Approved For Release 2013/02/06 : CIA-RDP10-02196R000300020002-8

TABLE 1. Main Components of the Systematic Measurement Error

Parameter x_i	Error S_i, %	Source of estimate
Distance between detector electrodes (baseline) L	±0.1	Measurement conditions in the piping
External diameter of the piping D_e	±1.5	Tolerances on pipes according to engineering conditions
Wall thickness Δ	±1.0	
Time shift of the correlation maximum τ_{max}	±0.5	Engineering data of the 100-channel correlometer
Correction coefficient $K_c = 1$	±3.0	Measurement experience on test stands
Temperature correction of the measurements K_T	±0.1	Calculation

observed under our conditions, then with $k\alpha G \ll 1$ taken into account one can make use of the first terms of the series expansion: $E = kB_0G(1 - k\alpha G)$. In what follows, dependences of the form $E = AG - BG^2$, where the coefficients were found by the method of least squares, were determined in the analysis of our measurements. One can judge the quality of the approximation and the scatter of the experimental points from the deviations of the measurement results from the approximation curves, which deviate by more than 1% at only 12 points out of 150, and the mean square deviation is < 0.5%. The dependences obtained are used to represent the information with the help of the CCS (controlling computational system) of the BN-600 assembly and are used for the formation of a nonlinear scale of recordings in the standard secondary control system (transducer—amplifier—recorder).

Let us estimate the systematic and random measurement errors. We shall relegate errors associated with inexact knowledge of the geometrical parameters of the measuring section and an error in their temperature correction, the error in determination of the time shift caused by the engineering data of the equipment, and the indeterminancy of the correction coefficient K_c, which establishes the relation between the average rate of movement of the hydrodynamic markers and the average flow velocity, to the nominally constant systematic errors. These errors, with an indication of the sources for the estimates, are given in Table 1. The errors are referred to parameters which directly enter into the formula for calculation of the flow rate:

$$G = k_n \frac{\pi (D_e - 2\Delta)^2 L}{4\tau_{max}} [1 + 3\alpha_s (T_{op} - T_m)],$$

where T_{op} is the piping temperature under operating conditions, °K; T_m, piping temperature during measurement of the geometrical characteristics of the measuring section, °K; and α_s, linear expansion coefficient of steel, $^oK^{-1}$.

A uniform distribution of terms [4] was assumed in estimating the total systematic error. Then

$$\sigma_\Sigma = c\sqrt{\sum_{i=1}^{n} (b_i S_i)^2},$$

where c is a coefficient determined by the confidence probability and the number of errors being summed, and b_i is the influence coefficient; $b_i = \frac{\partial G}{\partial x_i} x_i$. For a confidence probability of P = 0.99 (c = 1.42 for n = 5, [4]) and the data of Table 1, the total systematic error is $\sigma_\Sigma \approx 6.7\%$.

The random measurement error is caused by the random nature of the process being analyzed. With the correlogram collection time selected from experiment (2-5 min), reproducibility of the position of the maximum and the shape of the correlation peak is observed, which corresponds to a measurement error of the time shift which is less than 0.2%. An additional error arises in connection with the determination of the calibration characteristic when measuring the constant component of the signal. The systematic error is determined by the accuracy class of the potentiometer and amounts to ∿0.1% for typical values of the measured emf (5-10 mV). Fluctuations in the flowmeter signal are the main source of random error; based on

Declassified and Approved For Release 2013/02/06 : CIA-RDP10-02196R000300020002-8

Declassified and Approved For Release 2013/02/06 : CIA-RDP10-02196R000300020002-8

measurement experience, the inaccuracy in reading the compensated signal does not exceed one small division of the potentiometer scale, i.e., does not exceed 0.1-0.2%. To sum up, the total error in the calibration characteristics amounts to no more than 7%.

Thus, direct measurements of the sodium flow rate in the main heat-transfer loops of the BN-600 in the absence of any other means of control at all were made during the stage of start-up adjustments and power-up of the installation with the help of the correlation method. As a result the absolute value of the flow rate has been measured, the distribution of the flow rate through the steam generator loops has been established, the hydraulic characteristics of the assembly have been refined, and the calibration characteristics of the regular flowmeters have been determined over the entire range of circulation pump revolutions. With the data obtained taken into account, nominal conditions for the operation of the main circuits of the BN-600 have been established; the calibration characteristics have been included in the measurement and control system and are constantly used by station personnel at the present time. The research performed has increased to an appreciable extent the safety and has provided for confident power-up of the BN-600.

The task for subsequent investigations is to increase the accuracy of the correlation measurements for conversion of regular electromagnetic flow-rate indicators of fast reactors to a class of detectors. Most of the attention should be devoted to metrologic documentation of the correlation method on flowmeter test stands (the establishment of a limiting error of the coefficient K_c, which determines the correspondence between the velocity measured by the correlation method and the average flow velocity) and to standardization of the measuring section (reduction of the error in determination of the measuring volume and the use of standard sources of flow perturbations with fixed parameters).

LITERATURE CITED

1. Yu. E. Bagdasarov et al., Engineering Problems of Fast Neutron Reactors [in Russian], Atomizdat, Moscow (1969).
2. B. V. Kebadze et al., At. Energ., 45, No. 1, 30 (1978).
3. J. A. Shercliff, The Theory of Electromagnetic Measurement of the Flow Rate [Russian translation], Mir, Moscow (1965).
4. G. D. Rabinovich, Measurement Errors [in Russian], Énergiya, Moscow (1978).

ROLE OF FAST REACTOR PHYSICAL CHARACTERISTICS IN LIMITING THE CONSEQUENCES OF HYPOTHETICAL ACCIDENTS

I. A. Kuznetsov, Yu. E. Bagdasarov, and Yu. M. Ashurko

UDC 621.039.526:621.039.586

It has been proposed in some foreign papers that an accident involving the breakdown of the main circulating pumps and the simultaneous failure of the scram system be taken as the maximum design basis accident in a fast reactor. Actually, it is difficult to imagine more serious reactor operating conditions than in this situation. It was assumed that under these conditions the coolant very quickly starts to boil and is ejected from the core. The fuel then melts. The displacement of the molten fuel in combination with the effects of the radioactivity resulting from the removal of the coolant from the core may lead to an energy burst with the formation in the reactor of a bubble of evaporated fuel at high pressure and temperature. It is the opinion of the authors of the above proposal that the expansion of this bubble accompanied by the liberation of mechanical energy determines the maximum load for which the primary loop of the reactor must be designed. It should be stated at once that in the opinion of most specialists in our country such an accident can be taken as the maximum hypothetical, but not the maximum design basis accident in a fast reactor, since there is a negligible probability of such a large number of breakdowns and failures in the reactor equipment and systems occurring simultaneously in practice. The consequence of this hypothetical accident are analyzed in developing a plan to protect the staff and population. In the analysis the question arises of how much the change of temperature can be limited by

Translated from Atomnaya Énergiya, Vol. 54, No. 2, pp. 103-108, February, 1983. Original article submitted April 1, 1982.

 0038-531X/83/5402-0110$07.50 © 1983 Plenum Publishing Corporation

Declassified and Approved For Release 2013/02/06 : CIA-RDP10-02196R000300020002-8

Declassified and Approved For Release 2013/02/06 : CIA-RDP10-02196R000300020002-8

the intrinsic physical characteristics of the reactor — reactivity feedback. It is desirable that the reactor have such characteristics that in the breakdown of all the pumps the reactor power would decrease rapidly as the result of temperature reactivity effects, and the coolant in the core would not start to boil. In this case the fuel elements would have sufficient stability to prevent the development of a dangerous situation in spite of an appreciable temperature rise [1]. This definite optimism is based on features of fast reactors which distinguish them from reactors of other types and contribute to their safety: a large "underheating" of the coolant at the core outlet under nominal operating conditions at temperatures below boiling (∿350-400°C), very good heat transfer to liquid metals, and certain development of natural circulation of the coolant in the reactor.

The rate of rise of the core temperature resulting from the shutdown of the primary loop pumps is determined largely by their coast-down constant. It is known [2] that when pumps coast freely the flow rate of the coolant through the reactor varies hyperbolically with time. The time for the flow rate to be halved, which is practically the same as the coast-down constant of the pumps, is ∿3.5 sec for the BN-350 reactor, and ∿6 sec for the BN-600 reactor. The rapid decrease of the flow rate leads to a rapid increase in the core temperature. In such a situation the rate of rise of the sodium temperature in the most stressed fuel element assembly for the BN-350 and BN-600 reactors reaches 50-70°C/sec. This imposes more rigid requirements on the rapid action and accuracy of the coolant flow rate scram system.

Simplification of the flow rate scram system by increasing the coast-down constant of the pumps complicates the problem of thermal shock in the structural elements. In existing installations the rate of fall of the coolant temperature at the reactor outlet in relatively fast scrams (FS) is decreased by slowing down the main circulating pumps. The temperature variations are moderated mainly by an outlet mixing chamber whose time constant is inversely proportional to the rate of flow of coolant through it. Slowing the coast-down of the pumps during a FS decreases its effective time constant and increases the rate of fall of the temperature and the thermal stresses in the structural elements. For example, by increasing the coast-down constant of the BN-350 reactor pumps from 3.5 to 50 sec, the stresses at the surface of the intermediate heat exchanger housing in a FS are more than doubled.

It should be noted here that a large mass of sodium in the reactor tank does not imply good moderation of the temperature variations at its outlet in emergencies. It is quite complicated to ensure such thorough mixing in the tank that a large part of the coolant takes part in the heat exchange.

An increase of the coast-down constant of the primary loop pumps is justified if it promises additional advantages in ensuring reactor safety, e.g., if it is an important help in preventing boiling of the coolant during pump breakdown with the simultaneous failure of the scram system.

Let us first estimate the asymptotic temperature changes in the reactor in the transition from forced to natural circulation. We write down the reactivity balance equation from which we determine the parameters of the final state [2]:

$$(K_N + K_W \delta G)(\bar{n} - 1) + \delta G K_W + K_t(\theta_{in} - \theta_{in,0}) + \rho_{ex} = 0, \quad (1)$$

where K_N, K_W, and K_t are, respectively, the power, flow-rate, and temperature reactivity coefficients;

$$\delta G = 1/\bar{G} - 1; \quad (2)$$

$\bar{n}$ and $\bar{G}$ are the reactor power and coolant flow rate through the reactor divided by their nominal values; θ_{in} is the coolant temperature at the reactor inlet.

In this equation the hydrodynamic effects of reactivity are not separated into individual components, but can be taken into account in the "external" component ρ_{ex} (reactivity introduced from the outside), since we plan to consider large changes in the flow rate, when practically all the hydrodynamic effects occur.

The coolant temperature at the core outlet in the final state is

$$\theta = \theta_{in} + \Delta\theta_0 \frac{\bar{n}}{\bar{G}};$$
$$\bar{n}(0) = 1,\ G(0) = 1,\ \theta_{in}(0) = \theta_{in,0}. \quad (3)$$

Declassified and Approved For Release 2013/02/06 : CIA-RDP10-02196R000300020002-8

Declassified and Approved For Release 2013/02/06 : CIA-RDP10-02196R000300020002-8

From the reactivity balance equation we obtain the following relation:

$$\theta = \theta(0) + \Delta\theta_0 \delta G \frac{K_N - K_W}{K_N + K_W \delta G} + \Delta\theta_{in}\left[1 - \frac{K_t \Delta\theta_0 (1+\delta G)}{K_N + K_W \delta G}\right] + \frac{\rho_{ex}\Delta\theta_0}{\frac{K_N}{1+\delta G} + \frac{K_W \delta G}{1+\delta G}}. \quad (4)$$

Here $\Delta\theta$ is the nominal heating of the coolant in the core. The power and flow-rate reactivity effects characterize the nominal operating conditions.

In the transition from nominal conditions ($\bar{n} = 1$, $\delta G = 0$) to natural circulation of the coolant following pump shutdown, when $\delta G \gg 1$, we obtain

$$\theta = \theta(0) + \Delta\theta_0 \frac{K_N - K_W}{K_W} + \Delta\theta_{in}\left[1 - \frac{K_t \Delta\theta_0}{K_W}\right] + \rho_{ex}\frac{\Delta\theta_0}{K_W}. \quad (5)$$

If the coolant temperature at the reactor inlet is not changed, and the external reactivity component is zero, the heating of the coolant in the reactor is established at the level

$$\Delta\theta = \Delta\theta_0 \frac{K_N (1+\delta G)}{K_N + K_W \delta G} \approx \Delta\theta_0 \frac{K_N}{K_W}. \quad (6)$$

For example, for the BN-350 reactor $K_W = -0.19 \times 10^{-2}$, and $K_N = -0.72 \times 10^{-2}$ [3] in the range 0-650 MW. Therefore, following shutdown of the primary loop pumps in the BN-350, and the transition to natural circulation, the heating of the sodium in the final steady state is 3.8 times greater than the initial value. This means that for a constant inlet temperature, a temperature of 920°C is established at the core outlet. The boiling point of sodium is ∿960°C.

According to calculations of G. M. Pshakin, $K_N = -0.686 \times 10^{-2}$ and $K_W = -0.256 \times 10^{-2}$ for the BN-600 reactor. Therefore, the final heating of the sodium in this reactor is 2.7 times as large as the initial value, which for a constant inlet temperature corresponds to a temperature of ∿970°C at the core outlet.

Equation (6) shows that if other conditions remain the same, the larger the increase in the heating of the coolant in the reactor in the transition from forced to natural convection in a self-regulating regime the greater the ratio of the power coefficient of reactivity to the flow-rate coefficient. This means that to limit the heating it is necessary to strive for an increase in the absolute value of those components of the reactivity related to the temperature of the coolant and steel, and a decrease in those related to the fuel temperature. This can be achieved by certain structural measures, but analysis [4] shows that these measures lead to a decrease in the channel stability reserve "reactivity-power".

Let us now consider the effect of a change in the inlet temperature on the temperature of the reactor. In case of complete loss of power, which actually may be the cause of the shutdown of all the circulating pumps, it is impossible to ensure maintenance of a constant inlet temperature. Its variation depends largely on the heat-transfer arrangement in the tertiary loop.

Let us return to Eq. (5), which relates the temperature changes of the coolant at the reactor inlet and the core outlet. Clearly, most frequently

$$|K_t \Delta\theta_0| > |K_W|, \quad (7)$$

since in most cases K_W lies between $^1/_2(K_t - K_R)\Delta\theta_0$ and $^1/_2 K_t \Delta\theta_0$, where K_R is the component of the temperature coefficient of reactivity due to radial expansion of the reactor; $K_R < 0$ and $|K_R| < |K_t|$. This means that lowering the coolant temperature at the reactor inlet will lead to a temperature rise at the core outlet.

In principle there are the following possibilities of emergency heat removal from the tertiary loop of a fast reactor: removal of heat by an auxiliary air heat exchanger connected to the primary loop of the reactor; removal of heat by an air heat exchanger connected to the secondary loop of the reactor; removal of heat by a once-through steam generator; removal of heat by a steam generator with natural circulation.

There is a danger of a very large temperature drop at the reactor inlet when heat is removed by a once-through steam generator. Here without automatic maintenance of the coolant temperature at the steam generator outlet the temperature at the reactor inlet may be lowered to the temperature of boiling water.

Declassified and Approved For Release 2013/02/06 : CIA-RDP10-02196R000300020002-8

Declassified and Approved For Release 2013/02/06 : CIA-RDP10-02196R000300020002-8

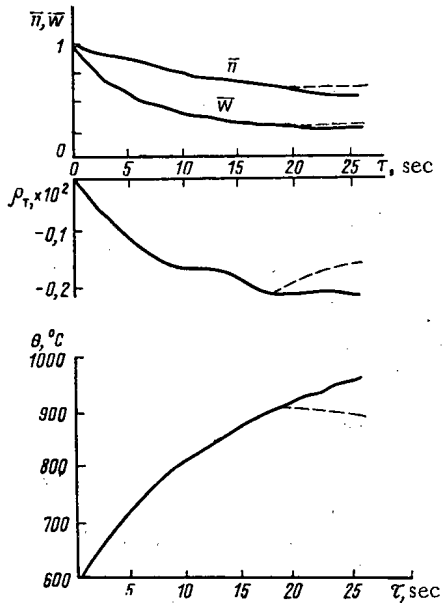

Fig. 1. Variation of BN-600 parameters under automatic regulation during (———) shutdown of primary loop pumps, and (-----) their slowdown; ρ_T, reactivity feedback; $\rho_{ex} = 0$; coast-down constant of circulating pumps b ≈ 6 sec.

The scheme employing a steam generator with natural circulation works better in this respect. In this scheme the coolant temperature at the steam generator outlet is limited by the saturation temperature of the water in it. Of course automatic maintenance of the steam pressure in the steam generator is required in this case, but this problem is simpler than that of maintaining a constant coolant temperature at the steam generator outlet by varying the flow rate of the feed water at low flow rates.

In schemes employing an air heat exchanger, the problem can be solved still more simply by choosing appropriate thermohydraulic characteristics of the air loop. They are chosen so that at the nominal temperature in the primary loop the air heat exchanger ensures the removal of a specified power. Therefore, in such a scheme the inlet temperature of the coolant will be uniquely determined by the reactor power level.

Under natural circulation the heating of the coolant in each loop is

$$\Delta\theta \sim (\bar{n})^{2/3}. \tag{8}$$

If $\bar{n}_*$ is the power level at which the coolant temperature at the reactor inlet is nominal, then for a scheme with an air heat exchanger

$$\Delta\theta_{in} = (\theta_{in.0} - \theta_{air})\left[\left(\frac{\bar{n}}{\bar{n}_*}\right)^{2/3} - 1\right], \tag{9}$$

where θ_{air} is the air temperature. The natural circulation flow rate is

$$G \sim \bar{n}^{1/3}; \tag{10}$$

$$\delta G = \frac{1}{G} - 1 \approx \alpha_1 (\bar{n})^{-\frac{1}{3}} \gg 1. \tag{11}$$

As a result the reactivity balance equation for the conditions under consideration takes the form

$$K_N \bar{n} + K_W \alpha_1 \bar{n}^{2/3} + K_t (\theta_{in.0} - \theta_{air})\left(\frac{\bar{n}}{\bar{n}_*}\right)^{2/3} = K_N + K_t (\theta_{in.0} - \theta_{air}) - \rho_{ex}. \tag{12}$$

It clearly makes sense to seek its solution for

$$K_N + K_t (\theta_{in.0} - \theta_{air}) - \rho_{ex} < 0, \tag{13}$$

since otherwise, even after cooling to the ambient air temperature, the reactor must go over into a subcritical state. Equation (12) is written here to show that it has a unique solution

Declassified and Approved For Release 2013/02/06 : CIA-RDP10-02196R000300020002-8

Declassified and Approved For Release 2013/02/06 : CIA-RDP10-02196R000300020002-8

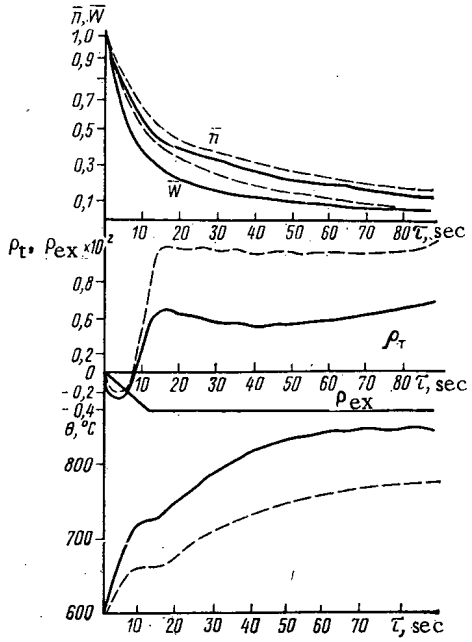

Fig. 2. Variation of BN-600 parameters under self-regulating conditions following shutdown of primary loop pumps for b = 6 sec (———) and b = 10 sec (-----); $\rho_{ex} = -0.4 \times 10^{-2}$.

for $n \geqslant 0$. This becomes clear if in addition to condition (13) we use the fact that $K_N < 0$, $K_W < 0$, $K_t < 0$, and $\theta_{in,o} > \theta_{air}$. Physically this means that the stable reactor state found is the only one possible, and does not depend on the order in which the parameters governing the process are changed.

The estimates presented apply for a final steady state. Actually, pump shutdown during nonstationary operation leads to still larger temperature changes, since a decrease in the reactor power always results in greater heating of the coolant than that which ensures compensation of the reactivity changes resulting from a decrease in power. It is also necessary to take account of the energy release from the decay of fission fragments. The relations we have presented are valid so long as the reactor power exceeds the residual power release. In the transition to natural circulation the neutron component of the power can fall to zero, and the subsequent change in temperature will be determined by the decay of the residual energy release. All this is taken into account in calculating nonstationary processes in a reactor with the ROS-25 program [5]. The results of such a calculation for the BN-600 reactor are shown in Fig. 1. If the pumps break down and the scram system fails, the sodium at the core outlet begins to boil after ∿26 sec. Thus, the existing reactivity feedback here is insufficient for an effective decrease of power. On the other hand, Eq. (7) shows that the introduction of a small negative reactivity can improve the situation considerably. By substituting specific values into Eq. (7), the temperature change at the core outlet is

$$\Delta\theta = 454 - 2\Delta\theta_{in} + 855 \cdot 10^2 \rho_{ex} \tag{14}$$

for the BN-350, and

$$\Delta\theta = 370 - 2.09\Delta\theta_{in} + 860 \cdot 10^2 \rho_{ex} \tag{15}$$

for the BN-600. It is clear from this that the introduction of even the automatic regulator (AR) rods into the core significantly decreases the temperature change. According to the design algorithm, in a relatively FS the safety rods (SR) are introduced into the core at the same time the AR rods are inserted with maximum velocity. The simultaneous failure of all the SR may result from the failure of the electronic system, or from mechanical damage of the core, e.g., misalignments produced by an earthquake or thermal strains. In the latter case it may be difficult to insert the SR into the core by free fall. Here it is assumed that measures taken in the design to make the equipment earthquake proof for some reason turned out to be ineffective. From the very beginning the AR rods are partially inserted into the core, and for a relatively FS are driven in by an electric motor. Therefore, misalignments and deformations

Declassified and Approved For Release 2013/02/06 : CIA-RDP10-02196R000300020002-8

Declassified and Approved For Release 2013/02/06 : CIA-RDP10-02196R000300020002-8

unforeseen in the design which are difficult to overcome for SR do not prevent the insertion of the AR rods. The effectiveness of each of the two AR rods is 0.2×10^{-2} for the BN-350 reactor, and 0.26×10^{-2} for the BN-600 reactor. The emergency rod of the AR is ordinarily located in the upper part of the core. If it is assumed that the working rod of the AR is in the central part of the core, and the positive hydrodynamic reactivity effects ($\sim 0.5 \times 10^{-3}$) are taken into account, the reserve reactivity which can be used to decrease the power is $-(0.25 - 0.4) \times 10^{-2}$. As a result, the temperature change at the core outlet is decreased by 200-300°C. In this case the final temperature is 700°C for the BN-350, and 650°C for the BN-600, independently of the flow rate of natural circulation so long as this flow rate permits the removal of the residual power release without exceeding the indicated temperature. Calculation and operating experience indicate that such a flow rate can be maintained in the primary loop. In nonstationary processes which occur with pump shutdown, a high temperature is reached of course, but nevertheless it remains below the boiling point of sodium. The coolant flow rate decreases rapidly; flywheels on the pumps to prolong their coast-down can be helpful. Figure 2 shows calculated values of nonstationary processes following shutdown of the BN-600 primary loop pumps. The reactor power decreases as a result of temperature reactivity effects and the introduction of AR rods at the rate of 70 mm/sec. The calculations were made for pump coast-down constants of 6 and 10 sec. In the first case the maximum sodium temperature at the core outlet reaches 850°C, and in the second case 775°C. These results show that one AR rod is sufficient to prevent boiling of the sodium in the BN-600 reactor.

The results obtained also permit a new look at a duplicate scram system based on a different physical principle. Proposals of the introduction of such a system are commonly criticized because of technical difficulties. This is actually the case if a large effectiveness of the duplicate system is required, but if, as follows from the calculations presented, the effectiveness can be chosen at a level of $(0.2 - 0.5) \times 10^{-2}$, the possibilities of such a system are very much greater.

Equations (14) and (15) are a good illustration of the effect of changes of the inlet temperature on the core temperature. For each degree the inlet temperature is lowered, the core temperature rises two degrees. This makes clear the role of the system maintaining the coolant temperature at the steam generator outlet, which must function reliably under all conditions. This also shows the advantage of emergency heat removal systems employing air heat exchangers when the inlet temperature is maintained spontaneously.

All the preceding estimates apply to the case of complete pump shutdown with transition of the reactor to natural circulation of the coolant. In this case, as already stated, complete shutdown occurs only when the power supply fails. But the BN-350 and BN-600 installations are provided with independent power supplies — diesel power plants which can keep the motors of the main circulating pumps operating at reduced speeds. Therefore, for these reactors failure of the scram system more likely involves slowdown rather than complete stoppage of the pumps. The temperature of the sodium at the core outlet of the BN-600 reactor does not reach the boiling point, even without the insertion of any absorbing rods (Fig. 1).

LITERATURE CITED

1. A. A. Proshkin et al., At. Energ., 45, No. 2, 98 (1978).
2. Yu. E. Bagdasarov et al., Technical Problems of Fast Reactors [in Russian], Atomizdat, Moscow (1969).
3. V. V. Orlov et al., At. Energ., 42, No. 1, 3 (1977).
4. I. A. Kuznetsov, Preprint FÉI-702, Obninsk (1976).
5. I. A. Kuznetsov and V. N. Leonchuk, Preprint FÉI-834, Obninsk (1978).

Declassified and Approved For Release 2013/02/06 : CIA-RDP10-02196R000300020002-8

Declassified and Approved For Release 2013/02/06 : CIA-RDP10-02196R000300020002-8

MEASUREMENTS OF THE CROSS SECTION OF THE ^{237}Np(n, 2n) REACTION AT NEUTRON ENERGIES OF 14.8 MeV

E. A. Gromova, S. S. Kovalenko,
Yu. A. Nemilov, L. D. Preobrazhenskaya,
Yu. A. Selitskii, B. I. Tarler,
Yu. N. Trofimov, V. B. Funshtein,
and S. V. Khlebnikov

UDC 539.172.484

The cross section of the ^{237}Np(n, 2n) reaction must be known when several practical problems of nuclear power generation are to be solved. The following ^{236}Np nuclides are formed in the ^{237}Np(n, 2n) reaction: the short-lived ^{236}Np(s) nuclides with $T_{1/2} = 22.5 \pm 0.4$ h and the long-lived ^{236}Np(l) with $T_{1/2} = (1.15 \pm 0.12) \cdot 10^5$ yr [1]. Of greatest importance for applications is the reaction in which the short-lived nuclide is formed; the yield of the nuclide is determined in the present work. (For simplifying the notation we will omit the subscript s in what follows). Owing to the ^{236}Np decay, ^{236}Pu and ^{232}U accumulate in the fuel of nuclear reactors. During fuel regeneration and winning of ^{238}Pu in the reactor via the chain ^{237}Np(n, γ) $\rightarrow$ ^{238}Np(β^-) $\rightarrow$ ^{238}Pu for use in isotope power sources, the useful product is contaminated with ^{232}U. In the ^{232}U decay chain there appear nuclei emitting "hard" γ radiation which must be brought into account in the design of biological radiation shields. The data which in [2-5] have been published on the cross sections of the ^{237}Np(n, 2n) reaction were obtained by measuring the α activity of ^{236}Pu produced in the β^- decay of ^{236}Np (α-technique). As shown in Fig. 1, the number of ^{236}Np nuclei can be basically determined not only with the α technique, but also by recording the γ radiation of ^{236}U (γ method). The γ method is hard to employ, because the quantum yield of the radiation is low and the radiation must be picked out from the high intrinsic γ activity of a neptunium sample and from the complicated γ spectrum of the products resulting from the ^{237}Np fission by neutrons. An attempt to record the γ ^{236}U did not lead to the desired results [4].

In order to determine the cross section of the ^{237}Np(n, 2n) reaction at a neutron energy of 14.8 MeV, we developed and used the technique of measuring the γ activity of ^{236}U and comparing the activity with the results obtained under identical irradiation conditions with the aid of the traditional technique of measuring the alpha activity of ^{236}Pu.

The Conditions of ^{237}Np Irradiation. The neutrons were obtained from the low-voltage NG-400 accelerator via the T(d, n)^{4}He reaction in which thick rotating tritium–titanium targets were bombarded with 250 keV deuterons. By rotating the target, the tritium burnout could be substantially reduced. In this way, the average neutron flux could be maintained at the level $2 \cdot 10^{10}$ $1/4\pi \cdot$sec. The irradiated sample in the form of a plane glass vial with a concentrated solution of neptunyl nitrate was placed 20 mm from the neutron source. The amount of neptunium was 100-200 mg and the irradiation time was 20 h.

The flux of neutrons passing through the irradiated neptunium sample was measured in two ways. One of the techniques was based on recording the fission products of natural uranium in an ionization chamber. Corrections for the neutron flux dependence upon the distance were determined via the relative activation of three gold foils placed up against the uranium target and also from two sides of a flat test tube with neptunium. In the other technique, in which no geometrical corrections had to be introduced, the neutron flux was determined from the accumulation of ^{97}Zr (one of the products resulting from the ^{237}Np fission) in the irradiated sample. For this purpose the energy spectrum of γ radiation of the neptunium fission products was measured with a Ge(Li) detector; the lines resulting from ^{97m}Nb (E_γ = 743.4 keV) and ^{97}Nb (E_γ = 657.9 keV), which are in equilibrium with ^{97}Zr, were determined. A correction for the decay of the ^{236}Np and ^{97}Zr nuclei formed during irradiation was introduced, and the variations of the neutron flux were taken into account. The calculation was made on the basis of a periodic recording (every 1000 sec) of the number N_{fi} of uranium-fission events in the ionization chamber.

Translated from Atomnaya Énergiya, Vol. 54, No. 2, pp. 108-111, February, 1983. Original article submitted June 2, 1982.

 0038-531X/83/5402-0116$07.50 © 1983 Plenum Publishing Corporation

Declassified and Approved For Release 2013/02/06 : CIA-RDP10-02196R000300020002-8

Declassified and Approved For Release 2013/02/06 : CIA-RDP10-02196R000300020002-8

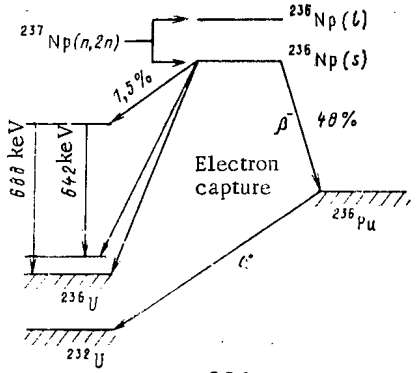

Fig. 1. Decay scheme of ^{236}Np [6] with indications of the α and γ transitions used for determining the cross section of the ^{237}Np(n, 2n) reaction. The probability of the β decay and of electron capture is expressed in percent.

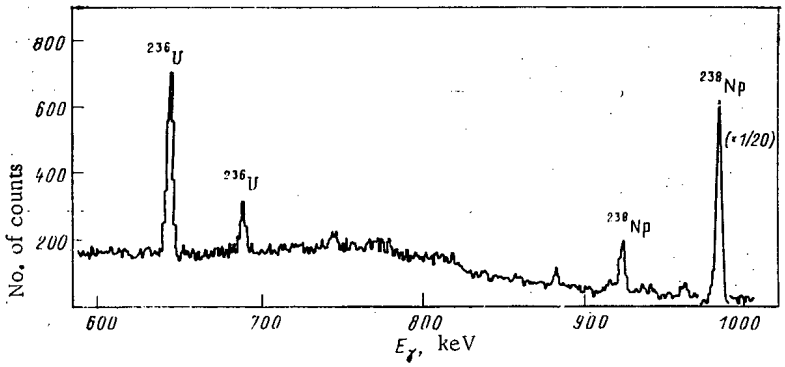

Fig. 2. Spectrum of the γ radiation of irradiated neptunium after purification from the fission products.

Determination of the Cross Section of the ^{237}Np(n, 2n)^{236}Np Reaction Through the γ Activity of ^{236}U. The γ radiation spectra were measured with a Ge(Li) detector (volume 38 cm^3) and the electronics of the "Vektor" system. Under the conditions of the γ measurements, the ^{237}Np sample used created a too high background load on the Ge(Li) detector so that the normal operation of the electronics was disturbed. When the γ radiation of ^{236}U with E_γ = 642 keV was recorded in the presence of an intense but not too "soft" radiation from the ^{237}Np sample, a 6-mm lead–cadmium combination filter absorbing mainly the soft part of the background spectrum with $E_\gamma \leqslant$ 100 keV was used. The harder part of the spectrum corresponding to ^{233}Pa (E_γ = 300 - 416 keV) was removed by chemical purification. The ^{237}Np was purified from the ^{233}Pa immediately before the irradiation of the sample; the purification was made with a sorption column filled with glass wool; the ^{233}Pa was adsorbed on the column from a neptunium solution in 12 N nitric acid. The solution was held in contact with the glass wool for 12 h [7]. The protactinium concentration at the time of the γ measurements was basically determined from the protactinium accumulation in the neptunium sample during the time after purification. The protactinium concentration was under real conditions 30 times smaller than the equilibrium value. The coefficient of background suppression obtained with a thin filter and the chemical purification from ^{233}Pa amounted to $\sim 10^3$. The intensity of the γ radiation with E_γ = 642 keV was decreased only by a factor of 3.

But these operations proved to be insufficient for measuring the cross section of the ^{237}Np(n, 2n) reaction through the intensity of the line with E_γ = 642 keV. Six hours after irradiation of the neptunium sample with neutrons, the peaks of the ^{236}U γ radiation could hardly be separated from the background of the intense radiation from fragments resulting from neptunium fission. By increasing the time interval between the end of the irradiation and the beginning of the γ measurements, an advantage could not be obtained, because the relatively short half-life of the ^{236}Np implies that the intensity ratio of γ line to be

Declassified and Approved For Release 2013/02/06 : CIA-RDP10-02196R000300020002-8

Declassified and Approved For Release 2013/02/06 : CIA-RDP10-02196R000300020002-8

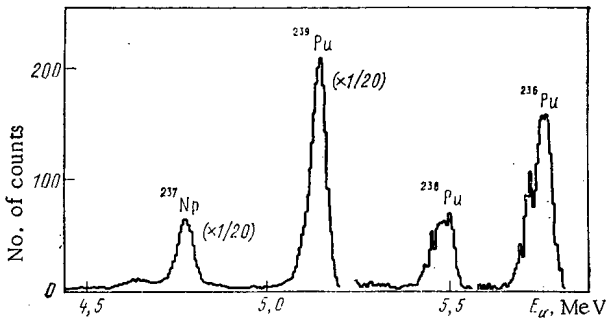

Fig. 3. Energy spectrum of the α particles of the plutonium fraction obtained from irradiated neptunium.

determined and the γ radiation of the fission products does not improve. The necessary reduction of the background was obtained by chemical purification of the neptunium from the fission products. After removing a small portion of the neptunium solution for determining the integral neutron flux through the yield of the ^{97}Zr fragment nuclide, the major part of the solution was subsequently purified on two distributing chromatographic columns with TBF and D2EHPA applied to porous granular Teflon [8].

The γ spectrum obtained after purification from the fission products is shown in Fig. 2 The 642- and 688-keV lines caused by the γ radiation of ^{236}U are clearly visible in the spectrum. In addition, the γ radiation of ^{238}Np produced in the ^{237}Np(n, γ) reaction can be observed. The amount of ^{236}Np was determined through the intensity of the line with E_γ = 642 keV, with a statistical error of 2% and an error of 2% in the efficiency of recording the γ quanta.

The amount of ^{237}Np in the sample which had been irradiated and purified from protactinium and fission products was determined with two techniques. One of the techniques is based on measurements of the α activity of ^{237}Np in some part of the sample, with the half-life $T_{1/2} = (2.14 \pm 0.01)\cdot 10^6$ yr [9] being used in the calculations. In the second technique, the γ activity of some portion of the sample is compared with the γ activity of a standard ^{237}Np source; the comparison is made through the intensity of the 86.5-keV line. The two techniques rendered results which coincided within the error limits of 2%.

Measurements made with an ionization chamber for fission events were the basic technique for determining the neutron flux. The cross section of the ^{237}Np(n, 2n)^{236}Np reaction was calculated with this technique using the formula

$$\sigma_{n,2n}(^{237}\mathrm{Np}) = \sigma_{n,f}(U)\frac{N(\mathrm{U})\,N(^{236}\mathrm{Np})\,K}{N(\mathrm{Np})\sum_i N_{fi}(\mathrm{U})\exp(-\lambda t_i)},$$

where $\sigma_{n,f}$(U) is the cross section of ^{238}U fission assumed as $(1.23 \pm 0.02)\cdot 10^{-24}$ cm^2 [10]; N(U), N(Np), number of ^{238}U and ^{237}Np nuclei, respectively; N(^{236}Np), number of ^{236}Np nuclei determined with the γ measurements for the time at which the measurements begin; t_i, time elapsing between the irradiation interval Δt_i under consideration and the beginning of the measurements; N_{fi}(U), number of fission events in the uranium target during the irradiation interval Δt_i; K, geometrical correction accounting for various distances between the uranium (neptunium) and the neutron source; and λ, decay constant of ^{236}Np [1]. When the absolute quantum yield is used for E_γ = 642 keV and n_γ = 0.98% [11], we obtain $\sigma_{n,2n}(^{237}\mathrm{Np}) = (0.23 \pm 0.05)\cdot 10^{-24}$ cm^2.

The main source of errors in the $\sigma_{n,2n}(^{237}\mathrm{Np})$ measurements with the γ technique is the 20% error of the probability of ^{236}Np decay on the 678.6-keV level of the ^{236}U nucleus, since the γ radiation considered is generated in transitions from this level. Corrections accounting for neutron scattering in the aqueous solution of neptunyl nitrate (2 ± 1%) and at the construction materials (1.5 ± 1%), and accounting also for the neutron multiplication by the (n, 2n) reaction at the components of the ionization chamber and the chamber of the tritium target (1 ± 0.5%) and the replacement of tritium by deuterium in the titanium target (0.2%), were introduced in the calculated cross sections. The error of the coefficient K of geometrical correction amounted to 2%. When the error in the absolute quantum yield was disregarded, the error of the cross section measured amounted to 5%.

Declassified and Approved For Release 2013/02/06 : CIA-RDP10-02196R000300020002-8

Declassified and Approved For Release 2013/02/06 : CIA-RDP10-02196R000300020002-8

TABLE 1. Cross Section of the ^{237}Np(n, 2n)^{236}Np Reaction in the Neutron Energy Range 14-15 MeV

Neutron energy, MeV	$\sigma_{n,2n}$ (^{237}Np), b	Reference
14,5±0,4	0,39±0,07	[2], 1961
14,95±0,31	0,27±0,01	[3], 1973
14,74±0,25	0,28±0,01	[3], 1973
14,39±0,16	0,32±0,01	[3], 1973
14,12±0,05	0,34±0,01	[3], 1973
13,77±0,05	0,40±0,01	[3], 1973
15,0±0,3	0,247±0,022	[4], 1975
		Present work
14,8±0,2	0,23±0,05	γ-technique
14,8±0,2	0,276±0,014	α-technique

When the neutron flux was determined from the concentration of the ^{97}Zr accumulated in the irradiated sample, a certain amount of the solution was stored for 6 h after its irradiation so that equilibrium between ^{97}Zr and the daughter γ emitter ^{97}Nb could be attained. The intensity of the ^{97}Nb and ^{236}U γ lines was determined under identical geometrical conditions. Corrections were introduced for the dependence of the γ quantum recording efficiency upon the quantum energy and for the contribution of γ emitters of close energy values (^{91}Sr with 652.9 keV and ^{128}Sb with 743.3 keV); the $\sigma_{n,2n}$ (^{237}Np) values were calculated with the following published data: ^{97}Zr half life 16.82 h [12], $\sigma_f(^{237}\text{Np}) = (2.50 \pm 0.07)\cdot 10^{-24}$ cm^2 [13], and ^{97}Zr yield (5.43 ± 0.49)% [13]. The result was $\sigma_{n,2n}(^{237}\text{Np}) = (0.24 \pm 0.06)\cdot 10^{-24}$ cm^2 in the determination of the neutron flux through the ^{97}Zr concentration in the irradiated sample. An error of 10% was obtained when the error in the (known) absolute quantum yield of the 642-keV γ quanta was disregarded. It follows from a comparison of the cross section values that the two independent techniques of determining the neutron flux rendered results which are in good agreement. The quantum yield of the γ radiation in the ^{236}Np decay must be measured with greater precision for the further development of the γ technique.

Determination of the Cross Section of the ^{237}Np(n, 2n)^{236}Np Reaction Through the α Activity of ^{236}Pu. The above cross section value of the ^{237}Np(n, 2n) reaction coincides within the error limits with the values obtained by measurements of the α activity of ^{236}Pu in previously published papers. For additionally checking the elements of the $\sigma_{n,2n}(^{237}\text{Np})$ determination technique based on the γ activity of ^{236}U, we made an experiment in which the cross section was determined with the traditional technique of measuring the α activity of ^{236}Pu (see Fig. 1). After irradiation, ^{239}Pu was added to neptunium as a carrier and indicator of the loss of ^{236}Pu in the subsequent chemical treatment. The admixed ^{238}Pu in the label substance did not exceed 10^{-2}% of the ^{239}Pu mass; ^{236}Pu was practically absent. When this technique is used, the initial neptunium sample must be thoroughly purified from plutonium isotopes, and the plutonium must also be purified from neptunium when it is separated from the irradiated sample.

The initial sample of the present work contained admixed ^{239}Pu, ^{238}Pu, and ^{236}Pu in amounts of 10^{-2}, 10^{-4}, and 10^{-9}%, respectively, of the amount of neptunium. The sample was purified from plutonium with the technique described in [14]. The result was that the plutonium concentration was reduced by a factor of 10^5. The admixed ^{236}Pu in the purified neptunium was negligible in comparison with the amount of this nuclide formed after irradiation. The plutonium was separated from the irradiated sample with a chromatographic ion exchange column containing AG^R 1-X2 (BiO-Rad) resin.

The α-spectrometry source prepared from the plutonium fraction by vacuum evaporation contained 40% of the entire ^{236}Pu amount accumulated in the neptunium target. Figure 3 shows the energy spectrum of the α particles, which was measured with a silicon surface-barrier detector. The cross section of the ^{237}Np(N, 2n)^{236}Np reaction was calculated with the formula

$$\sigma_{n,2n}(\text{Np}) = A_\alpha \frac{N_\alpha(^{236}\text{Pu})}{N_\alpha(^{239}\text{Pu})} \frac{1}{N_{\text{nucl}}\Phi_{\text{fl}}\lambda W},$$

where A_α is the α activity of ^{239}Pu introduced into the neptunium sample as a label substance; $N_\alpha(^{236}\text{Pu})/N_\alpha(^{239}\text{Pu})$, intensity ratio of the α radiation from ^{236}Pu and the α radiation of ^{239}Pu in the α spectrum obtained; N_{nucl}, number of ^{237}Np nuclei in the target; Φ_{fl}, integral neutron flux through a unit of area of the neptunium target; λ, decay constant of ^{236}Pu [9]; and W, probability of the β^- decay of ^{236}Np; W was assumed as 0.48 ± 0.01 [1].

Declassified and Approved For Release 2013/02/06 : CIA-RDP10-02196R000300020002-8

Declassified and Approved For Release 2013/02/06 : CIA-RDP10-02196R000300020002-8

The corrections listed above were introduced in the cross section value calculated. The cross section values $(0.268 \pm 0.013)\cdot10^{-24}$ cm^2 and $(0.283 \pm 0.014)\cdot10^{-24}$ cm^2 were obtained after two measurements. The α technique rendered the average value $\sigma_{n,2n}(^{237}Np) = (0.276 \pm 0.014)\cdot 10^{-24}$ cm^2, which, within the error limits, agreed with both the result of the cross section measurements with the γ technique and the published data (see Table 1).

Each of the techniques used in the present work to measure the cross section of the (n, 2n) reaction is characterized by its advantages and shortcomings. More specifically, the γ technique does not require a thorough preliminary purification of the neptunium from plutonium, whereas the α technique allows long-lasting neutron irradiation of the neptunium; this is particularly important when $\sigma_{n,2n}$ is to be measured at low E_n values.

As indicated above, the cross section values determined in our work refer to the formation of the short-lived ^{236}Np nuclide. The total cross section of the (n, 2n) reaction, calculated with proper regard for the yield ratio $^{236}Np(\ell)/^{236}Np(s)$ [15] and with improved probability figures of the β^- decay of ^{236}Np, is $(0.037 \pm 0.02)\cdot10^{-24}$ cm^2.

In conclusion, the authors thank B. K. Seleznev for accelerator operation and A. I. Tarazevich for helping in preparing the irradiation and performing it.

LITERATURE CITED

1. INDC(NDS)-108/N, IAEA, Vienna (1979).
2. J. Perkin and R. Coleman, J. Nucl. Energy, Part A/B, 14, 69 (1961).
3. J. Landrum, R. Nagle, and M. Lindner, Phys. Rev., C8, 1938 (1970).
4. K. Lindeke et al., Phys. Rev., C12, 1507 (1975).
5. C. Paulson and E. Hennely, Nucl. Sci. Eng., 55, 22 (1974).
6. C. Lederer et al., Nucl. Phys., A135, 36 (1969).
7. I. E. Starik and L. D. Sheidina, Radiokhimya, 1, No. 3, 270 (1959).
8. V. N. Ushatskii et al., Radiokhimiya, 21, No. 1, 75 (1979).
9. Yu. V. Khol'nov et al., Characteristic Features of the Radiations from Radioactive Nuclides Used in the National Economy [in Russian], Atomizdat, Moscow (1980).
10. M. Sowerby, B. Patrik, and D. Mather, Ann. Nucl. Sci. Eng., 1, 409 (1974).
11. N. G. Gusev and P. P. Dmitriev, Quantum Radiation of Radioactive Nuclides (Handbook) [in Russian], Atomizdat, Moscow (1977).
12. D. Nethaway et al., Phys. Rev., C16, 1907 (1977).
13. R. Coleman, B. Hawker, and J. Perkin, Inorg. Nucl. Chem., 14, 8 (1960).
14. V. N. Ushatskii, L. D. Preobrazhenskaya, and E. S. Gugel', Radiokhimiya, 15, No. 3, 450 (1973).
15. W. Myers, M. Lindner, and R. Newburg, J. Inorg. Nucl. Chem., 37, 637 (1975).

Declassified and Approved For Release 2013/02/06 : CIA-RDP10-02196R000300020002-8

Declassified and Approved For Release 2013/02/06 : CIA-RDP10-02196R000300020002-8

EFFECTS OF PREVIOUS HEAT TREATMENT AND MECHANICAL WORKING ON THE SWELLING OF 0Kh16N15M3B STAINLESS STEEL

V. A. Krasnoselov, V. I. Prokhorov, A. N. Kolesnikov, and Z. A. Ostrovskii

UDC 621.039:553.3:669.15

According to current theoretical concepts, swelling is largely determined by the absorption kinetics for point defects at sinks, of which the main ones are pores and freely moving dislocations [1-4]. As a result, there is no doubt that swelling is affected by the initial structure of the material and therefore by the preliminary thermomechanical treatment.

Our experiments with the BOR-60 have characterized the swelling of stainless steel 0Kh16N15M3B in four states arising from previous treatments. These are, firstly, the austenitized state with an initial dislocation density of 10^{12}-10^{13} m^{-2}; secondly, the state after cold deformation by stretching by 5, 10, or 20%, when the initial dislocation density may attain 10^{16} m^{-2}; thirdly, the state after thermomechanical treatment under the following conditions: 10% cold deformation and annealing at 1070°K for 1 h or 10% deformation at 920°K and annealing at 920°K for 100 h (according to published data, this treatment produces a polygonal structure with an elevated stability in the subgrain boundaries under thermal fluctuations and with high stability against coagulation in the excess phases [5]); and fourthly,

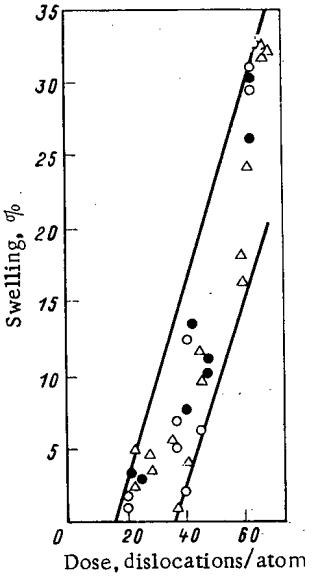

Fig. 1

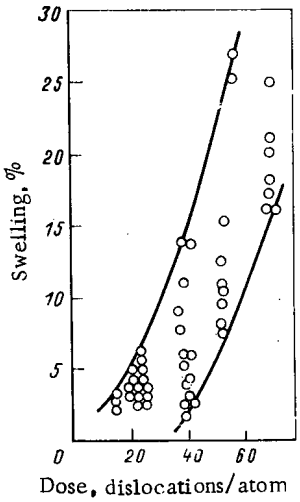

Fig. 2

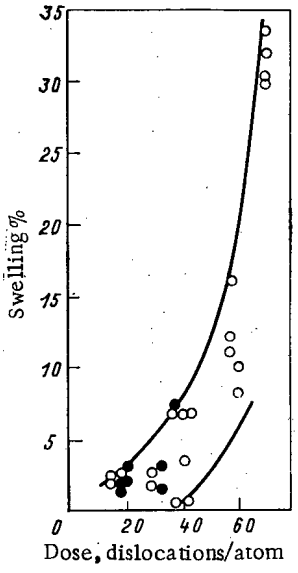

Fig. 3

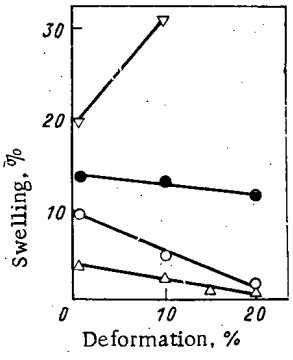

Fig. 4

Fig. 1. Radiation swelling in 0Kh16N15M3B stainless steel at 670-820°K after various previous treatments; ○ — 10% cold deformation and annealing at 1070°K, 1 h; ● — 10% deformation at 920°K and annealing at 920°K, 100 h; Δ) annealing at 920°K, 100 h.

Fig. 2. Radiation swelling in austenitized 0Kh16N15M3B steel at 670-820°K.

Fig. 3. Radiation swelling in 0Kh16N15M3B steel at 670-820°K after 10% (○) or 5% (●) cold deformation.

Fig. 4. Effects of previous cold deformation on the radiation swelling of 0Kh16N15-M3B steel at irradiation temperatures of 720-820°K and doses of 20-30 (Δ); 40-50 (○); 55-60 (●) and 65-70 (▽) displacements/atom.

Translated from Atomnaya Énergiya, Vol. 54, No. 2, pp. 111-114, February, 1983. Original article submitted May 24, 1982.

0038-531X/83/5402-0121$07.50 © 1983 Plenum Publishing Corporation

Declassified and Approved For Release 2013/02/06 : CIA-RDP10-02196R000300020002-8

Declassified and Approved For Release 2013/02/06 : CIA-RDP10-02196R000300020002-8

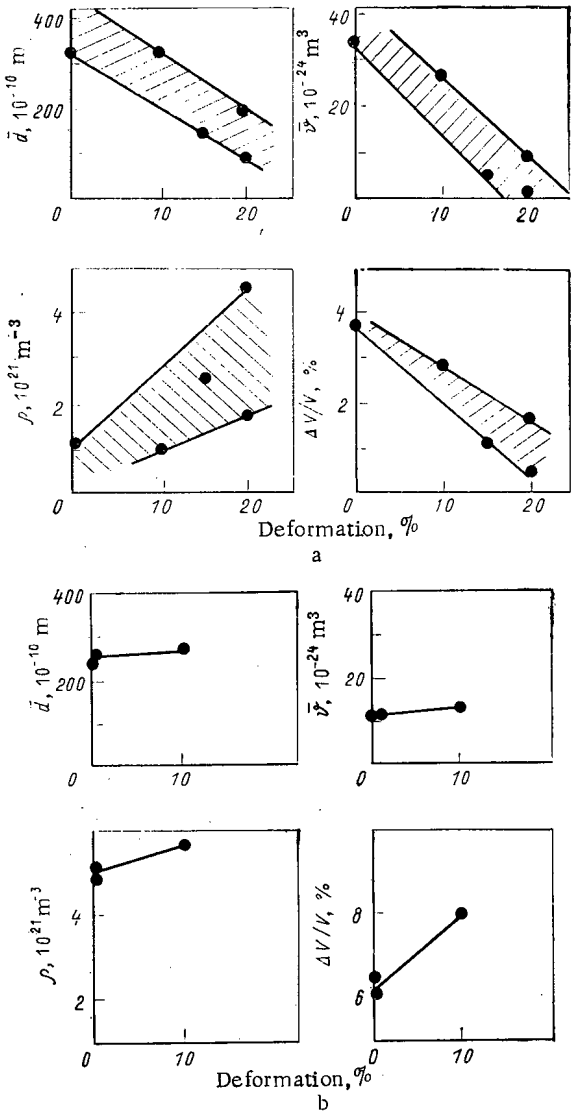

Fig. 5. Effects of previous cold deformation on the porosity and swelling parameters for 0Kh16N15M3B steel for irradiation at 770°K (a) or 720°K (b) up to doses of 30 (a) and 50 (b) displacements/atom (d, average diameter; $\bar{v}$, average volume; ρ, concentration; ΔV/V, swelling).

the state arising from annealing at 920°K for 100 h, which is characterized by the deposition of a large amount of excess phases from the solid solution.

The swelling was determined with an absolute error of ±0.5% from the density reduction. The concentration and average volume of the pores were calculated from data obtained by transmission electron microscopy, with relative errors of 30 and 20%, correspondingly.

Thermomechanical treatment and prolonged annealing do not increase the resistance of the steel to swelling: at doses of 60-70 displacements/atom (on the TRN standard), the maximum swelling was 30-32%, as against 25-27% in the austenitized state (Figs. 1 and 2). This evidently occurs because the solid solution is depleted of alloying components during the deposition of the secondary phases.

Out of the 0Kh16N15M3B steel specimens examined, the minimum swelling occurred in those that had undergone cold deformation (Fig. 3), and the swelling decreased as the deformation increased from 5 to 20% (Fig. 4). However, 10% cold deformation effectively suppresses the swelling only at doses up to 60 displacements/atom, which evidently applies also for 20% cold deformation. This conclusion is confirmed by data from reactor and simulation experiments on

Declassified and Approved For Release 2013/02/06 : CIA-RDP10-02196R000300020002-8

Declassified and Approved For Release 2013/02/06 : CIA-RDP10-02196R000300020002-8

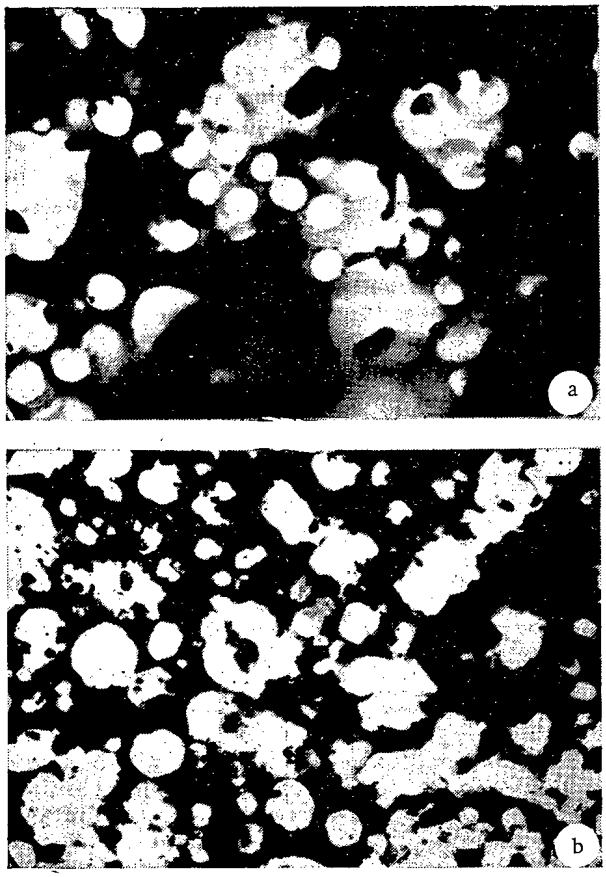

Fig. 6. Pores in OKh16N15M3B stainless steel irradiated at 670-820°K to a dose of 70 displacements/atom with preliminary austenitization (a) and preliminary 10% cold deformation (b).

the similar stainless steels AISI 316 and 304. For example, type 316 stainless steel has been cold deformed by 20% and then bombarded at 920°K by nickel ions of energy 5 Mev, and there was a marked increase in the rate of swelling when a dose of 50-60 displacements/atom was attained [6]. A similar effect has been observed in reactor experiments: on irradiating steel 316 in the EBR II reactor to a dose of 70-75 displacements/atom, low swelling occurred only at 30% cold deformation, while at 10 and 20% deformation the swelling was comparable with that found for austenitized steel [7] or even exceeded it.

The swelling of cold-deformed steels accelerates when sufficiently high doses are reached, which is evidently related to microstructure evolution. During the irradiation, the dislocation density is reduced, and up to doses of 50 displacements/atom there is virtually no difference in this respect between austenitized and cold-deformed steels [8]. Simultaneously, during dislocation glide the impurities are spread along the boundaries of the grains and phases, which may alter the pore nucleation conditions. Also, the poisoning of the dislocation sinks should occur somewhat more slowly in the cold-deformed material than in the austenitized one. At sufficiently high doses, this leads to an excess of unpoisoned dislocation sinks in the cold-deformed steel even at the same dislocation density. Finally, the deposition and coagulation of the excess phases in a cold-deformed material substantially differ from those observed in austenitized steels, which should be appreciably reflected in the swelling.

Therefore, when the dislocation densities are equal, the excess of working dislocation sinks in cold-deformed material leads to an increase in the preference factor and consequently to a higher rate of pore growth, while the depletion of the solid solution in trapping impurities facilitates pore nucleation. As a result, there is an increase in the swelling rate with a certain increase in the length of the transitional (incubation) period.

This is confirmed by electron microscopy. In OKh16N15M3B steel at not excessively high doses, there is a reduction in the size of the pores as the degree of cold deformation in-

Declassified and Approved For Release 2013/02/06 : CIA-RDP10-02196R000300020002-8

Declassified and Approved For Release 2013/02/06 : CIA-RDP10-02196R000300020002-8

creases (i.e., the growth rate is reduced), while the pore concentration is appreciably higher (Fig. 5). As a result, there is an increase in the overall number of point-defect sinks in the early stages of irradiation and the swelling is reduced.

Raising the dose (50 displacements/atom) produces a qualitative alteration in the picture of porosity growth: the pore sizes in cold-deformed steels are the same as or larger than those in austenitized ones, while the pore concentration, as previously, increases with the previous deformation (Figs. 5, 6). As a result, the swelling in a cold-deformed steel increases appreciably.

Accelerated pore growth indicates elevated vacancy supersaturation in the cold-deformed material, while the increase in pore concentration as the cold deformation increases is due to the reduction in the trapping-atom concentration, as these atoms migrate along the dislocations at interphase and intergrain boundaries during the irradiation.

These experiments have shown that stainless steels of the austenite class have a resistance to radiation swelling dependent on the previous treatment. None of the states of OKh16N15M3B steel that have been examined provides reasonable stability in the sizes of reactor components at doses of 100 displacements/atom or more. Cold deformation stretching by 10% and evidently also by 20% is an effective means of suppressing the swelling in chrome–nickel steels only at doses of up to 50-70 displacements/atom.

LITERATURE CITED

1. A. Brailskford and R. Bullough, J. Nucl. Mater., 69-70, 434 (1978).
2. I. A. Akhiezer and A. N. Davydov, Metallofizika, 3, No. 1, 3 (1978).
3. Yu. V. Konobeev and V. A. Pechenkin, in: Radiation Defects in Metal Crystals [in Russian], Nauka, Alma Ata (1978), p. 187.
4. R. Bullough, B. Eyre, and G. Kulcinski, J. Nucl. Mater., 68, No. 2, 168 (1977).
5. V. S. Ivanova et al., The Role of Dislocations in the Hardening and Failure of Metals [in Russian], Nauka, Moscow (1965).
6. F. Garner and G. Guthrie, in: Proc. Int. Conf. on Radiation Effects and Tritium Technology for Fusion Reactors, Oak Ridge, Vol. 1, ORNL (1976), p. 491.
7. W. Appleby et al., in: Proc. Int. Conf. on Radiation Effects in Breeder Reactor Structure Materials, Met. Soc. AIME, New York (1977), p. 509.
8. W. Wolfer, J. Nucl. Mater., 90, 175 (1980).

CORROSION OF ZIRCONIUM ALLOYS IN THE SUPERHEATED STEAM OF A POWER REACTOR

B. V. Samsonov, S. V. Seredkin,
V. N. Shulimov, V. K. Shamardin,
and G. I. Maĭrshina

UDC 621.039.553.36:669.296

High corrosion resistance in superheated steam is one of the requirements on fireproof zirconium alloys for the RBMK power reactors. A study of the corrosion kinetics without withdrawing samples from a reactor channel allows a more complete judgment about the mechanism of the process, in particular about the effect of irradiation, the composition of the medium, etc. Of two zirconium alloys studied, Zr + 2.5% Nb (No. 1) and Zr + 1% Fe + 1% Cr + 0.4% W (No. 2), the first one is of special interest, as in irradiation conditions its corrosion rate decreases at temperatures above 350°C.

Procedure for Conducting the Experiment. In order to study the corrosion a resistometric method was used [1]. The sensor is an insulated casing on which two wires of identical length are wound, but of different diameter from the material being investigated, and it forms part of a bridge measurement circuit. During corrosion, in consequence of the formation of an oxide film, the electrical resistance of the samples R_1 and R_2 varies, and the ratio $\varkappa = R_1/R_2$ is related with the thickness of the film δ by the relation

Translated from Atomnaya Énergiya, Vol. 54, No. 2, pp. 114-116, February, 1983. Original article submitted July 23, 1981; revision submitted February 8, 1982.

 0038-531X/83/5402-0124$07.50 © 1983 Plenum Publishing Corporation

Declassified and Approved For Release 2013/02/06 : CIA-RDP10-02196R000300020002-8

Declassified and Approved For Release 2013/02/06 : CIA-RDP10-02196R000300020002-8

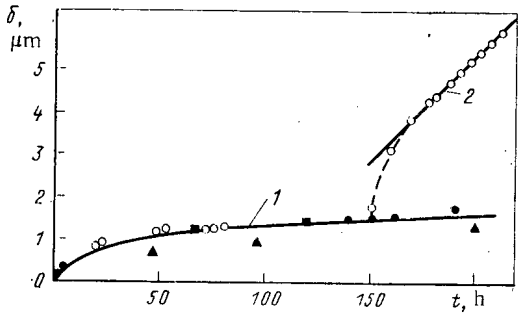

Fig. 1

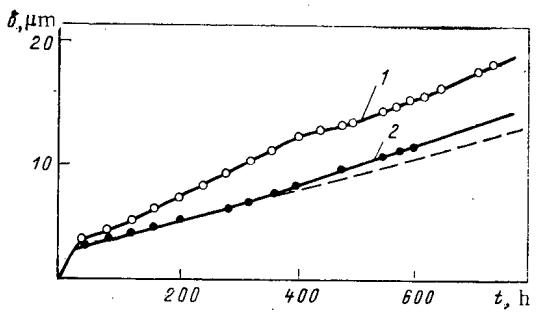

Fig. 2

Fig. 1. Oxidation kinetics of alloy No. 1 in superheated steam: 1) with T = 410°C; 2) with T = 550°C (K = 16 mg/(dm^2·day); ○ first sensor, annealed at 600°C, 2 h; ● second sensor, annealed at 600°C, 2 h; ■ Zr + 2.5% Nb + 0.5% Ta, 400°C, annealed at 580°C, 2 h; ▲ Zr + 2.5% Nb, 400°C, steam from water, $\sigma = 5 \cdot 10^6$ Ω/cm, p = 12 MPa, annealed 580°C, 16 h.

Fig. 2. Effect of irradiation on the oxidation kinetics of alloy No. 1: 1) without irradiation, T = 530°C; 2) with irradiation, $3.8 \cdot 10^{13}$ neutrons/(cm^2·sec) ($E \geqslant 0.8$ MeV) at 510°C (---) and 530°C (——).

$$\delta = \frac{S_1}{\Pi_1} \frac{\varkappa - S_2/S_1}{\varkappa - \Pi_2/\Pi_1}, \qquad (1)$$

where S_1, S_2, Π_1, and Π_2 are the initial cross sections and perimeters of the wire samples. A sensor of similar design had been used already in similar investigations [2]. The accuracy of the method is independent of the intensity of the neutron flux and temperature variations during irradiation. However, at high temperature (≥700°C) the electrical resistance changes not only in consequence of the formation of the oxide film, but also because of the dissolution of oxygen in the metal. In addition, the relation (1) was obtained for plane geometry of the sample. In the case of experiments at a temperature of ∿500°C, the resulting measurement error caused by these two factors amounts to ∿10% and can be estimated by means of monitored metallographic analysis of the wires after completion of the experiment.

Wire samples of alloys Nos. 1, 2 with a diameter of 0.39 and 0.19 mm were prepared for the investigations; after repeated deformation during rolling, these were annealed in vacuo for 2 h at 600°C. The texture of the wires was not determined. It is relevant to note here that in the majority of the published data the effect of this factor on the corrosion of samples of different configuration is not taken into consideration.

The ampul with the sensor was irradiated in a channel of the RBT-6 reactor. At the same time, a similar sensor was tested in an autoclave without irradiation. The autoclave and the ampul were connected by pipelines; the rate of supply of superheated water vapor with a low oxygen content (<0.02 mg/kg) amounted to 100 g/day at a pressure of up to 2 MPa.

Results and Discussion. In order to verify the efficiency of the sensor, experiments were conducted beforehand in the autoclave without irradiation. A comparison of the results of the corrosion tests of the wire samples of alloy No. 1 with the existing experimental data [3, 4], obtained by a gravimetric method, confirms the significant deviations and reproducibility of the experimental points (Fig. 1). The somewhat lower values of the weight increase with respect to the results of [3] can be explained [5] by the more prolonged annealing of the samples at 580°C. The inclusion of data for the alloy Zr + 2.5% Nb + 0.5% Ta (see Fig. 1) is justified by the existing information about the similar effect of alloying tantalum and niobium on the corrosion resistance of zirconium [5]. A slight variation of pressure and flow rate of the steam did not alter the rate of corrosion, which also had been noted earlier [6].

The metallographic investigation of the sample cross section showed a uniform distribution of hydride inclusions in the wires of different diameter.

After oxidation of the wire on the first sensor at 410°C during 150 h, the temperature was increased to 550°C (see Fig. 1, curve 2). The break in the oxidation curve, which occurred with a film thickness of δ = 3 - 4 μm, is seen clearly.

Declassified and Approved For Release 2013/02/06 : CIA-RDP10-02196R000300020002-8

Declassified and Approved For Release 2013/02/06 : CIA-RDP10-02196R000300020002-8

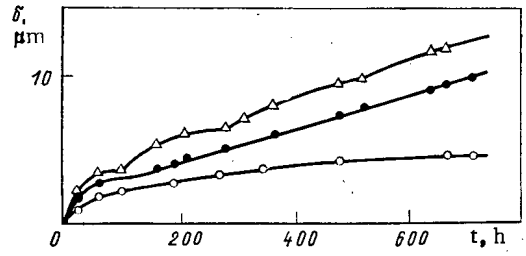

Fig. 3

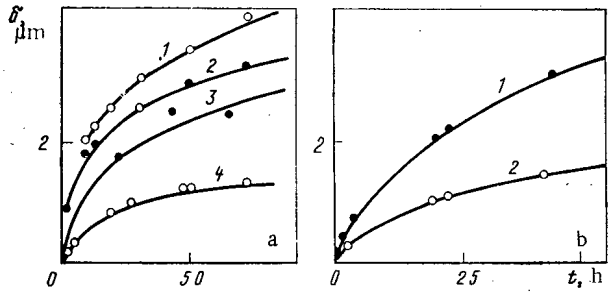

Fig. 4

Fig. 3. Effect of irradiation on the oxidation kinetics of the alloys at 480°C; Δ) alloy No. 2, with irradiation; ● alloy No. 1, with irradiation; ○ alloy No. 2 without irradiation.

Fig. 4. Oxidation kinetics of alloys No. 1 (a) and No. 2 (b) in the initial period of time [○ without irradiation; ● with irradiation, $3.8 \cdot 10^{13}$ neutrons/($cm^2 \cdot sec$)]. Temperature: a) 510°C (1, 2), 465°C (3), 410°C (4); b) 465°C.

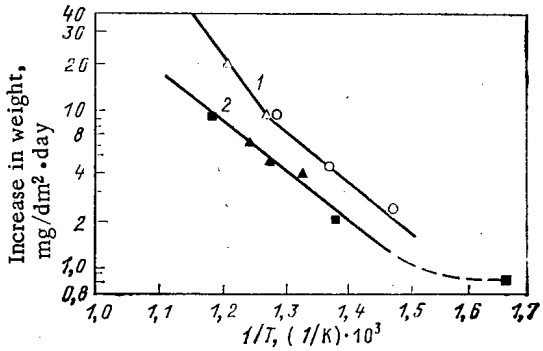

Fig. 5. Variation of the rate of corrosion of alloy No. 1 vs temperature: 1) without irradiation; 2) with irradiation, $3.8 \cdot 10^{13}$ neutrons/($cm^2 \cdot sec$); ○ [7]; Δ, ▲ corrosion sensor; □ gravimetric method.

The second and third experiments were conducted for the appearance of the effect of reactor irradiation on the corrosion kinetics of alloys Nos. 1, 2. The kinetic curves for alloy No. 1 (Fig. 2) show that irradiation with a flux of fast neutrons with an intensity of $3.8 \cdot 10^{13}$ neutrons/($cm^2 \cdot sec$) reduces corrosion by a factor of 1.3-1.7, but an increase of temperature from 510 to 530°C increases the corrosion after 300 h of testing from 4.5 to 5.7 mg/($dm^2 \cdot day$), and the average rate of corrosion of the alloy in extra-reactor conditions at 510-530°C amounted to 8.2 mg/($dm^2 \cdot day$), which coincides well with the data of [7].

The data from the metallographic analysis of the wires oxidized in the autoclave serve as additional confirmation. Within the limits of the measurement error the values of the thickness of the oxidized layer on the wires coincide, and they coincide with values found by measuring the electrical resistance. The reduction of the corrosion rate of alloy No. 1 under irradiation is explained by the radiation aging and further stabilization at a temperature >350°C [8, 9].

Similar relationships of the corrosion kinetics of alloy No. 2 are shown in Fig. 3. Two sensors were installed in the ampul (with wire of alloys Nos. 1, 2) irradiated at ∿480°C. The control sample was prepared from alloy No. 2. The graph shows the significant (by a factor of ∿2) acceleration of corrosion of alloy No. 2 and the reduction of corrosion of alloy No. 1 by the action of the radiation. The extrapolated value of the thickness of the oxide film coincides with the value measured metallographically. Figure 4 shows the oxidation kinetics of the alloys in the initial testing period (up to ∿80 h). Even with a film thickness of ∿1 μm irradiation reduces the rate of corrosion of alloy No. 1, whereas for alloy No. 2 the reverse effect is observed.

Declassified and Approved For Release 2013/02/06 : CIA-RDP10-02196R000300020002-8

Declassified and Approved For Release 2013/02/06 : CIA-RDP10-02196R000300020002-8

The kinetics of the initial stage of corrosion (up to ∿10 h) of alloy No. 1 (see Fig. 4a, curves 1, 4) are described quite accurately by the quadratic relation $\Delta m^2 = kt$, where Δm is the increase in weight, mg/dm²; $k = 3.54 \times 10^2 \exp\left(-\frac{30220}{RT}\right)$ is the calculated constant of the rate of oxidation, mg²/(dm⁴·sec); and t, time, sec. The value obtained for the activation energy coincides with the data on the diffusion of oxygen through an anion-defect oxide film [5]. The curves constructed for the rate of corrosion of alloy No. 1 vs the reciprocal of the temperature (Fig. 5) show the excellent agreement with the data determined by the gravimetric method on ring samples.

Irradiation with a flux of fast neutrons with an intensity of $3.8 \cdot 10^{13}$ neutrons/(cm²·sec) ($E \geqslant 0.8$ MeV) at a temperature of >350°C reduces the corrosion of alloy No. 1 by a factor of 1.3-1.7, but increases the corrosion of alloy No. 2 by a factor of 2 at 480°C during 100-800 h.

LITERATURE CITED

1. Corrosion and Protection of Chemical Equipment (Reference Handbook) [in Russian], Vol. 1, Khimiya, Leningrad (1969).
2. E. E. Fedyushin, V. P. Gol'tsev, and V. F. Korotov, in: Report of the All-Union School on Intrareactor Methods of Investigations [in Russian], Dimitrovgrad (1978), p. 169.
3. Corrosion Resistance of Reactor Materials (Reference Handbook) [in Russian], Atomizdat, Moscow (1976).
4. E. Tolksdorf, J. Nucl. Mater., 51, No. 3, 330 (1974).
5. V. G. Parfenov, V. V. Gerasimov, and G. I. Venediktova, Corrosion of Zirconium and Its Alloys [in Russian], Atomizdat, Moscow (1967).
6. R. Ronald et al., A study of Zircaloy-4 — Steam Oxidation. Reaction Kinetics. EPRI NP-225 (Research Project 249-1, September 1976).
7. A. S. Zaimovskii, At. Energ., 45, No. 6, 430 (1978).
8. M. G. Golovachev, At. Energ., 42, No. 5, 409 (1977).
9. V. Urbanic, The Effect of Aging on the Corrosion of Zr + 2.5% Nb. Presented at the NASA National Meeting, California, March 19-23, 1973.

EFFECT OF BOMBARDMENT WITH DEUTERIUM IONS ON THE STRUCTURE OF POLYCRYSTALLINE NIOBIUM

A. A. Pisarev, A. I. Evstyukhin, Yu. A. Perlovich, and V. G. Tel'kovskii

UDC 539.2:539.12.04:548.73

The effect of intense plasma radiation, including fast ions, can result in substantial changes in the surface layers of the material of the first wall; in particular, there may be a change in the microstructure, which to a significant degree determines the physicomechanical properties of the metal.

In the work reported here, in order to investigate how bombardment with deuterium ions affects the structure of annealed niobium, we employed the method of x-ray diffraction analysis. An x-ray photograph was taken on a URS-50IM diffractometer by the standard procedure [1]. The error in the measurement of the x-ray line intensities and half-widths was ∿10% and 2-3', respectively.

A 10 × 10-mm specimen of commercially pure niobium was cut from a 1-mm rolled plate, polished to a smoothness number of 8 and annealed in a vacuum of $\sim 10^{-3}$ Pa at 1000°C for 1 h. The initial structure formed by the rolling and subsequent recrystallization is characterized by comparatively fine complete grains and a highly developed texture, i.e., a preferential crystallographic orientation of grains.

The specimen was bombarded with 25-keV D^+ ions in a mass monochromator [2]. The mass and energy resolution of the ions was ∿200, the dose of the bombarding particles was $5 \cdot 10^{17}$

Translated from Atomnaya Énergiya, Vol. 54, No. 2, pp. 116-118, February, 1983. Original article submitted June 2, 1981; revision submitted September 23, 1982.

0038-531X/83/5402-0127$07.50 © 1983 Plenum Publishing Corporation

Declassified and Approved For Release 2013/02/06 : CIA-RDP10-02196R000300020002-8

Declassified and Approved For Release 2013/02/06 : CIA-RDP10-02196R000300020002-8

TABLE 1. Results of X-Ray Diffraction Measurements

Indices of x-ray lines	Intensity, arb. units: structureless standard [3]	Intensity, arb. units: unirradiated side	Intensity, arb. units: irradiated side	Line shift $\Delta\theta$, ang. min.	$\frac{\Delta d}{d} \cdot 10^3$	Increase $\Delta\beta$ in line width, ang. min.
011	100	63	123	−23	8,7	10
002	20	110	23	+9	−1,8	16
112	32	155	240	+9	−0,9	11
013	10	30	38	0	0	9

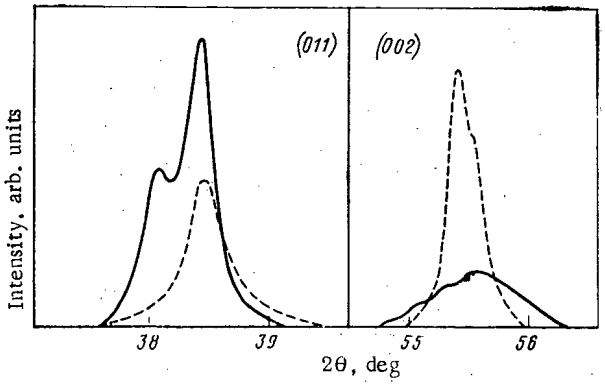

Fig. 1. (011) and (002) x-ray lines from a niobium specimen bombarded with deuterium ions. The dashed and solid lines, respectively, are for the unirradiated and irradiated sides of the specimens.

deuterons/cm^2, and the vacuum was $\sim 10^{-3}$ Pa. The temperature of the specimen during bombardment, monitored with a Pt–PtRh thermocouple, was 300°K. The effect of the bombardment was assessed by comparing the data for the irradiated and unirradiated sides of the target.

The position of the specimen in the holder of the goniometer was in accordance with the Bragg–Brentano x-ray focusing condition [1]. The normal to the surface of the flat specimen in this case is the bisector of the angle between the directions of the incident and recorded beams. Crystallographic planes parallel to the surface, therefore, are also in the reflecting position. Using an x-ray tube with a copper anode (K_α radiation), we were able to record (011), (002), (112), (013), (222), and (123) reflections for niobium. Each reflection was due to different groups of grains in which the {011}, {001}, {112}, {013}, {111}, and {123} crystallographic planes, respectively, were parallel to the surface. The relative number of grains of each orientation is determined by the character of the texture formed during the plastic strain, heat treatment, and irradiation and can be estimated from the ratio of the intensities of the various x-ray reflections [3]. According to the theory of x-ray diffraction [4], the position and shape of an x-ray line depends on the degree of distortion of the crystal lattice and the dispersion of its perfect blocks along the normal to the reflecting plane, i.e., in our case along the direction of bombardment. Accordingly, from the x-ray reflections we can estimate the change in the state of the crystal lattice only along the direction of the beam of bombarding ions, perpendicular to the surface of the specimen. During the photography the specimen was rotated around the normal to the surface, thus averaging the influence of certain inhomogeneities in the dose over the area of the specimen and eliminating effects caused by the grain size. The most significant information can be obtained by studying the intensities and angular positions of the lines.

Figure 1 shows the change in the profile of the (011) and (002) x-ray lines as a result of bombardment with deuterium ions. Table 1 gives data about the changes in the recorded characteristics of the main x-ray lines. The (002) reflection becomes weaker while the (011) and (112) reflections increase sharply. The observed broadening of the x-ray lines indicates

Declassified and Approved For Release 2013/02/06 : CIA-RDP10-02196R000300020002-8

Declassified and Approved For Release 2013/02/06 : CIA-RDP10-02196R000300020002-8

distortion of the structure of the specimen as a result of the bombardment. At the same time, bearing in mind that the irradiated specimens were in an annealed state, the increase in the intensity of the (011) and (112) lines can be explained only by the development of the process of grain reorientation under the action of the irradiation. The pronounced initial texture, characterized by the predominance of grains with a {001} rolling plane, becomes weaker and goes over into a texture with the predominance of grains in which the {112} and {011} planes are parallel to the surface of the specimen. Clearly, the redistribution of defects formed in the surface layer of the specimen under bombardment is accompanied by a rotation of the crystal lattice of the grains.

The thickness of the layer of half-attenuation of x rays with a wavelength $\lambda = 0.154$ nm is ~6 μm in niobium [5]. It is in this layer that the effects detected during x-ray analysis of the specimen are mainly localized. The scales of the observed changes in the x-ray scattering indicate that the action of the bombarding ions on the structure of the metal target is not limited to a layer with a thickness of several hundred interplanar spacings, but extends beyond the limits of the ion-stopping zone deep inside the specimen. A similar effect was also detected when molybdenum was bombarded with 55-keV He^+ ions [6]: distorted layers of metal are observed in a surface layer 3-4 μm thick, whereas the range of the ions is substantially shorter [7].

It must be pointed out that the recrystallization that occurs in the surface layers of the metal under bombardment with deuterium ions results in a considerable structural inhomogeneity over the thickness of the specimen and this should have a substantial effect on the strength properties of the metal.

The observed shift in the angular positions of the lines for the bombarded specimens attests to a change in the interplanar spacings (see Table 1). The lattice constant can change as a result of several processes, e.g., because of the intrusion of deuterons into interstices, the formation of intrinsic interstitials and vacancies, vacancy clusters, and complexes of deuterium atoms and vacancies, and purification or contamination of the surface layer during bombardment.

Comparing the position of the various x-ray lines recorded from opposite sides of the specimen, we can conclude that the predominance of one tendency or another depends on the direction of the bombardment. Indeed, the (002) and (112) lines are shifted to higher angles, while the position of the (130) line does not change.

The shift of the x-ray lines is accompanied by an increase in their overall angular half-width and by splitting. The latter can be caused by the inhomogeneity of the structure formed as a result of the bombardment. The deep-lying layers give x-ray reflections at the same angles as before, while the layers which have undergone changes reflect at slightly different angles. The splitting may also be due to tetragonal distortion in the lattice of the metal as a result of ordering of interstitials in the lattice [8].

This shift effect is observed most clearly for the (011) line, which is displaced to smaller angles by 25' after bombardment. This shift corresponds to an increase of approximately 1% in the interplanar spacing d_{011}. An increase in the lattice constant by 1% as a consequence of the rise in deuterium concentration corresponds to the formation of niobium hydrides [9]. Splitting of the x-ray lines as the hydrogen content in Nb–H alloy increases was observed earlier [10] and was attributed precisely to the formation of hydrides and the gradual transition from a bcc to a rhombic lattice.

It must be pointed out, however, that there are significant differences between the distortions of the crystal lattice under implantation of deuterium ions and under deuteration from the gaseous phase. In the first case they are considerably more complicated. The decrease in the interplanar spacings indicates that the effect of the irradiation on the crystal lattice of the metal is highly anisotropic. Existing model representations [11, 12], however, are inadequate for explaining all of the observed manifestations of such anisotropy and, in particular, the differences in the change in the position and shape of various x-ray lines as a result of bombardment. Moreover, the reproducibility of the changes in the lines is indicative of their random nature.

LITERATURE CITED

1. D. M. Kheiker and L. S. Zevin, X-Ray Diffraction Analysis [in Russian], Fizmatgiz, Moscow (1963).

Declassified and Approved For Release 2013/02/06 : CIA-RDP10-02196R000300020002-8

Declassified and Approved For Release 2013/02/06 : CIA-RDP10-02196R000300020002-8

2. V. A. Kurnaev, V. M. Sotnikov, and V. G. Tel'kovskii, in: Plasma Physics [in Russian], Atomizdat, Moscow (1967), p. 65.
3. G. Wasserman and I. Griven, Texture of Metallic Materials [Russian translation], Metallurgiya, Moscow (1969).
4. A. Guinier, Théorie et Technique de la Radiocristallographie, Dunod, Paris (1956).
5. L. I. Mirkin, X-Ray Diffraction Analysis Handbook [in Russian], Metallurgizdat, Moscow (1961).
6. V. N. Bykov et al., Fiz. Met. Metalloved., 34, 666 (1972).
7. H. Schitt, Rad. Effects, 6, 107 (1970).
8. V. N. Bykov et al., Ukr. Fiz. Zh., 15, 136 (1970).
9. H. J. Goldschmidt, Interstitial Alloys, Plenum Publ. (1968).
10. C. Wainwright et al., J. Less-Common Met., 6, 362 (1964).
11. S. T. Konobeevskii, Effect of Irradiation on Materials [in Russian], Atomizdat, Moscow (1967).
12. M. W. Thompson, Defects and Radiation Damage in Metals, Cambridge Univ. Press (1969).

BEHAVIOR OF TITANIUM DIBORIDE UNDER IRRADIATION AND POST-RADIATION ANNEALING

L. M. Murzin, V. V. Ogorodnikov, and V. D. Kelim

UDC 620.1:546.821/83:621.039

Irradiation of titanium diboride in a nuclear reactor leads to great changes in its properties, due to radiation damage by fast neutrons, which are responsible for accumulation of cascades of atomic displacements, as well as by slow neutrons, which cause (n, α) reactions on boron nuclei [1-3]. The increase in internal stresses also leads to formation and opening ofmicrocracks. The process of accumulation of radiation defects and formation of cracks can be easily inferred by measuring the electric resistance [2, 3]. This makes possible direct remote monitoring of radiation resistance of titanium diboride and other refractory compounds during irradiation.

For the investigations we used the method of synchronous measurement of electrical resistance, elongation, and thermo-emf of the specimen in a special setup loaded in the VVR-M channel. We placed hot-pressed specimens of titanium diboride with composition $TiB_{1.95}$ and dimensions 2.6 × 2.6 × 20 mm vertically at the center of the active zone. The flux density of the thermal neutrons constituted $8.6 \cdot 10^{13}$ neutrons/($cm^2 \cdot sec$) with a reactor power of 10 MW. The starting electrical resistance ρ_0 = 26.3 $\mu\Omega \cdot cm$, porosity P = 7%, and bending strength σ_0 = 300 ± 10 MPa; the chemical composition (mass %) was: 68.5 Ti; 29.5 B; 0.8 C.

The specimens were irradiated in a helium environment at a temperature ~500°C. We measured the electrical resistance with R-306 and V7-21 potentiometers and the elongation with an induction sensor; the results of the measurements were recorded on a modified ÉPR-09 M3 automatic plotter. A stainless steel rod served as a transmission element between the specimen and the sensor. The sensitivity of the measuring system was 0.1 μm, the error did not exceed 1%, and the range of the measurements was 3 mm.

To study the influence of periodic startup and shutdown of the reactor, the experiment on irradiation was performed at a temperature of 500°C with intermediate isochronous—isothermal annealing in the range 500-1250°C, with fluences $3 \cdot 10^{19}$, $6 \cdot 10^{19}$, and $1 \cdot 10^{20}$ neutrons/cm^2. To determine the bending strength, we irradiated the specimens to a fluence of $2 \cdot 10^{19}$ neutrons/cm^2 at 50°C in an ampul filled with argon, and annealed them in a TGV-1m furnace for 2 h at 500, 1000, and 1500°C. We performed the measurements at room temperature on an MM-150d setup.

RESULTS

Figure 1 shows the results of synchronous measurements of electrical resistance, elongation, thermo-emf, and temperature of titanium diboride during irradiation to a fluence of

Translated from Atomnaya Énergiya, Vol. 54, No. 2, pp. 118-122, February, 1983. Original article submitted June 30, 1980; revision submitted July 8, 1982.

 0038-531X/83/5402-0130$07.50 © 1983 Plenum Publishing Corporation

Declassified and Approved For Release 2013/02/06 : CIA-RDP10-02196R000300020002-8

Declassified and Approved For Release 2013/02/06 : CIA-RDP10-02196R000300020002-8

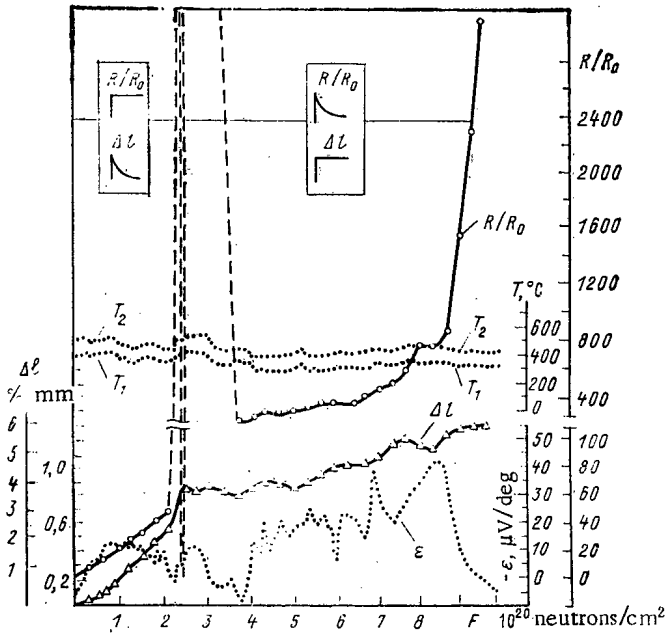

Fig. 1. Results of combined measurements of electrical resistance, elongation (Δl), thermo-emf (ε), and temperature (T_1 and T_2 are the temperatures at the ends of the specimen) for irradiation of titanium diboride (the elongation measurements shown were performed with the reactor shut down).

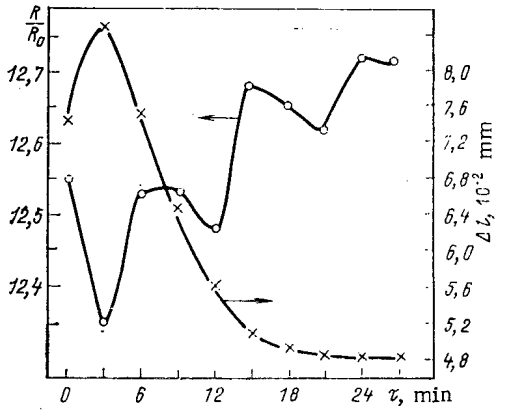

Fig. 2. Relaxation phenomena in titanium diboride accompanying a change in irradiation temperature at τ_{irr} = 185 h.

$1 \cdot 10^{21}$ neutrons/cm^2. The electrical resistance and elongation change nonmonotonically. But they first increase linearly, and then at a fluence of $2.1 \cdot 10^{20}$ neutrons/cm^2 there is a jump in elongation by 1.5%, which is accompanied by sharp jumps in electrical resistance. The duration of the period of sharp jumps $\sim 3.5 \cdot 10^5$ sec. At a fluence of $2.4 \cdot 10^{20}$ neutrons/cm^2, slow oscillations of the electrical resistance and elongation begin, and at $3.7 \cdot 10^{20}$ neutrons/cm^2 the ratio of electrical resistances R/R_0 decreases to 250, while with further irradiation the values of both parameters oscillate with an overall tendency to increase. The period of this oscillatory process is $\sim 1.7 \cdot 10^6$ sec. At a fluence above $8.1 \cdot 10^{20}$ neutrons/cm^2, the rate of increase in electrical resistance increases, while the nature of the increment to the elongation does not change. It should be noted that at $1 \cdot 10^{21}$ neutrons/cm^2 the specimen does not spontaneously decompose, but with any mechanical action transforms into microscopic dust. The coefficient of thermo-emf changes nonmonotonically during irradiation. At the jumps in electrical resistance and elongation, as well as at the predecomposition stage, it decreases

Declassified and Approved For Release 2013/02/06 : CIA-RDP10-02196R000300020002-8

Declassified and Approved For Release 2013/02/06 : CIA-RDP10-02196R000300020002-8

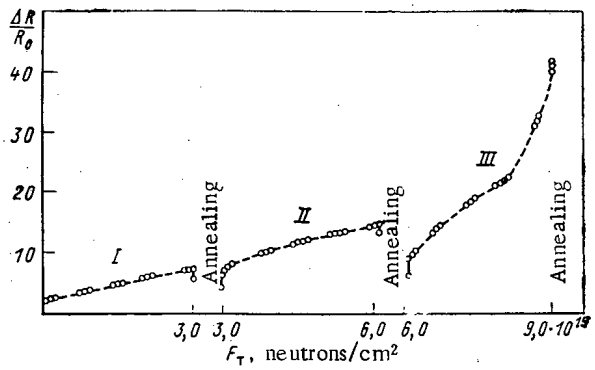

Fig. 3. Change in electrical resistance of titanium diboride under irradiation with intermediate annealing.

to the starting value. The temperature oscillations during irradiation are insignificant, but the average value of the temperature decreases monotonically, and at a fluence $1 \cdot 10^{21}$ neutrons/cm^2, this drop is 50°C. The change in the electrical resistance and elongation of the specimen while cooling during reactor shutdown is characteristic. The operational cycle of the reactor constitutes $3.6 \cdot 10^5$ sec. Up to fluence $2.1 \cdot 10^{20}$ neutrons/cm^2 (i.e., before the stage with the jumps), while cooling the specimen, a sharp jump is observed in the electrical resistance upwards, and it subsequently does not change until the reactor starts up again. The elongation in this case decreases exponentially. Under further irradiation (above $2.4 \cdot 10^{20}$ neutrons/cm^2), the electrical resistance increases rapidly after the reactor is shut down, and then decreases exponentially; the elongation sharply increases and remains at this level until the next startup of the reactor. The changes noted are shown in Fig. 1 (inserts). While cooling the specimen during reactor operation, the elongation decreases exponentially after increasing initially, while the electrical resistance in this case increases in jumps. The periods of the increasing and decreasing cycles constitute 350-400 sec (Fig. 2), while the total time for establishing an equilibrium state is $1.5 \cdot 10^3$ sec.

The results of a special experiment on irradiation with intermediate annealing are presented in Figs. 3-5. The values of $\Delta R/R_0$ after irradiation stages I-III constituted 5.25, 13.8, and 40.8, respectively (see Fig. 3). The bending strength for irradiated specimens decreased by 60%. The minimum strength after annealing at 1000°C is shown (see Fig. 4, curve 1). An increase in fluence leads to more significant changes under annealing (Fig. 4). During annealing after the third stage of irradiation, the specimen decomposed at 1000°C.

DISCUSSION OF RESULTS

According to the data on thermal stability of radiation defects in refractory compounds [1], we can assume that at 500°C ($0.23\,T_{melt}$) vacancies are immobile and are present in the form of single defects, while interstitial atoms are sufficiently mobile to form accumulations. In addition to the defects indicated, in cascade displacements, vacancy clusters can also form. Radiation defects increase internal stresses and they increase scattering of conduction electrons. The linear growth in electrical resistance at the first stage of irradiation (see Fig. 1 up to fluences $2.1 \cdot 10^{20}$ neutrons/cm^2 and Fig. 3 up to $3 \cdot 10^{19}$ neutrons/cm^2) indicate the additivity of the contribution of defects to such scattering, i.e., they indicate the absence of interactions between defects. For a stress sufficient to form microcracks, avalanche fracturing occurs, which sharply increases the electrical resistance at $2.1 \cdot 10^{20}$ neutrons/cm^2 (see Fig. 1). Elongation of the speciemn in this case increases by $\sim$1.5%. Since burnup of the isotope ^{10}B and the resulting stress decrease exponentially from the surface into the bulk of the specimen, it may be assumed that fracturing occurs mainly in a surface layer with thickness $\sim$0.1 mm. Since fracturing cannot occur with compressive stresses [4], cessation of crack development indicates equalization of compressive (created by the mass of the unit for measuring the deformation) and tensile stresses. The decrease in elongation and electrical resistance beyond the jump (see Fig. 1) indicates higher density of the specimen, which can occur by means of partial healing of microcracks. The microcracks formed are not completely healed due to the limited plasticity and further growth of radiation stresses. Competition between external compressive and tensile radiation stresses leads to periodic oscillatory variations in elongation and electrical resistance during further irradiation,

Declassified and Approved For Release 2013/02/06 : CIA-RDP10-02196R000300020002-8

Declassified and Approved For Release 2013/02/06 : CIA-RDP10-02196R000300020002-8

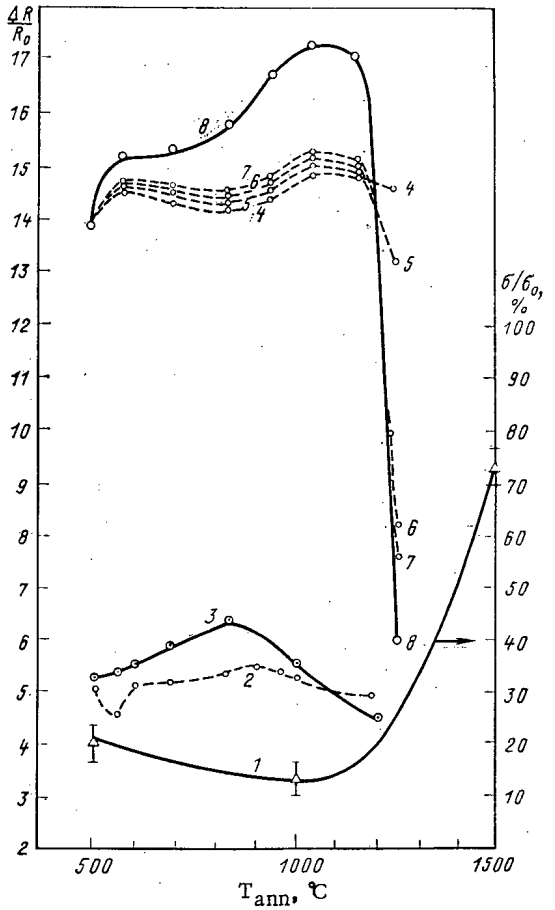

Fig. 4. Dependence of the relative strength and electrical resistance of titanium diboride on the annealing temperature: 1) σ/σ_0, $F = 2 \cdot 10^{19}$ neutrons/cm^2, $T_{irr} = 50°C$; 2, 3) $\Delta R/R_0$, $F = 3 \cdot 10^{19}$ neutrons/cm^2, $T_{irr} = 500°C$; 4-8) $\Delta R/R_0$, $F = 6 \cdot 10^{19}$ neutrons/cm^2, $T_{irr} = 500°C$; curves 3, 8 were obtained after cooling, curve 2 was obtained after holding for 15 min, and curves 4-7 were obtained after holding for 5, 15, 30 and 40 min, respectively (the data are referred to room temperature).

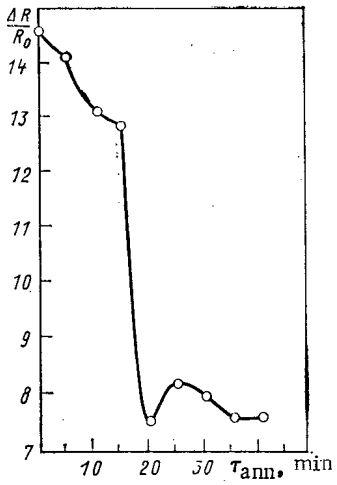

Fig. 5. Dependence of the electrical resistance on the annealing time at 1250°C for titanium diboride irradiated with a fluence of $6 \cdot 10^{19}$ neutrons/cm^2.

Declassified and Approved For Release 2013/02/06 : CIA-RDP10-02196R000300020002-8

Declassified and Approved For Release 2013/02/06 : CIA-RDP10-02196R000300020002-8

but the total increase in both parameters indicates the dominant role of tensile stresses, as well as ordering of the material capable of accepting external stress. Deformation of the specimen during radiation swelling proceeds via microplastic displacements, which is indicated by the jump-like growth in electrical resistance with a change in irradiation temperature (see Fig. 2). The large increase in electrical resistance and insignificant increase in elongation with fluence above $8.1 \cdot 10^{20}$ neutrons/cm^2 give a basis for assuming that pore-type volume defects are practically not formed at this stage of irradiation, while the concentration of two-dimensional defects increases, among which the most likely are disruptions along grain boundaries, resulting in decreased linkage between grains. Transformation of the specimen into microscopic powder with weak mechanical action (a push, shaking during disassembly of the ampul) proves the validity of this interpretation of the results obtained. Therefore, we can speak about the destruction of titanium diboride during prolonged irradiation (burnup of the isotope ^{10}B on the specimen surface at $1 \cdot 10^{21}$ neutrons/cm^2 constitutes ~95%). Compressive stresses slow down the development of microcracks on the surface and practically eliminate spontaneous destruction of the specimen. Under such conditions the kinetics of variations of electrical resistance differs from the kinetics obtained for freely suspended specimens with comparable irradiation temperatures [2]. Since compressive stresses slow down the process of radiation swelling, fracturing of the specimen begins at a relatively higher concentration of defects and at higher stresses.

Phenomena that occur with thermal cycling during shutdown and startup of the reactor play an important role in the change in structure and related properties and kinetics of radiation swelling. Titanium diboride is characterized by high brittleness and low heat resistance [5]. The heat resistance of brittle materials increases with increasing porosity due to an increase in the capability of the material to relax stresses, although some specialists explain this increase in heat resistance by irradiation-induced strengthening of carbides [6]. We should expect that hot-pressed titanium diboride with insignificant porosity will have low heat resistance with small fluences, when the structural changes are still small, while as the porosity increases and the structure becomes more open, its capability to relax and its heat resistance will increase. The absence of jumps in electrical resistance and elongation with shutdown of the reactor for specimens irradiated by high fluences (exceeding $3.6 \cdot 10^{20}$ neutrons/cm^2, see Fig. 1) proves the validity of this conclusion.

Analysis of the results of a special experiment on irradiation with intermediate annealing permitted specifying the mechanism of formation and healing of microcracks and separating radiation and thermal effects. The effects of annealing on the irradiated material involves considerable changes in the defect structure. From an analysis of the results of annealing and published data [1], it follows that the expansion of the crystal lattice with heating is accompanied by a decrease in local distortions caused by interstitial atoms, as a result of which the electrical resistance decreases. The liberation of helium atoms from traps and their capture by vacancy clusters increases microdistortions, masking the effect of lattice expansion and the total growth of electrical resistance in the region above 500°C (see Fig. 4, curve 2). When the specimen is cooled, local distortions surrounding gas-filled pores increase and the electrical resistance increases (see Fig. 4, curve 3). The electrical resistance can also increase due to the formation of microcracks from vacancy clusters and pores, where the gas pressure reached a critical level. The stress at which microcracks open can be estimated from the data presented in Fig. 1 and in [1]. At a fluence of $2.1 \cdot 10^{20}$ neutrons/cm^2, when microcrack formation is observed, the stress constituted 5 GPa (0.01 E, where E is Young's modulus), and, in addition, macroscopic swelling (see Fig. 1) exceeds by a factor ~5 the expansion of the crystal lattice [1]. As vacancies begin to move and form complexes, the number of sinks for helium atoms increases, as a result of which the microdistortions decrease. This causes a decrease in the electrical resistance accompanying heating above 900°C. The same effect could result from partial healing of microcracks as excess helium atoms leave the cracks. The strength of the material in this case increases (see Fig. 4, curve 1). The development of a defect structure with further irradiation intensifies the effects described above, but the general nature of the changes in the electrical resistance remains the same. The displacement of the peak electrical resistance with repeated annealing up to 1100°C (see Fig. 1, curves 4-7) indicates that with increasing concentration of defects, the critical pressure necessary for opening microcracks increases; the intensity of healing of pores and microcracks increases. The increase in gas pressure in pores when the temperature increases to 1100°C and decrease in pressure at higher temperatures can be judged from the change in the electrical resistance during the holding process (see Fig. 4, curves 4-7) and from the inversion of curves after reaching the maximum. The

Declassified and Approved For Release 2013/02/06 : CIA-RDP10-02196R000300020002-8

Declassified and Approved For Release 2013/02/06 : CIA-RDP10-02196R000300020002-8

threshold nature of microcrack healing appears with isothermal annealing. As a result of helium atoms leaving pores and microcracks, the pressure in them decreases, after which there is a partial closure of the microcracks, accompanied by a decrease in the electrical resistance after annealing for 15-20 min (see Fig. 5). Further change in electrical resistance is related with the viscoelastic aftereffect until equilibrium is established.

The change in electrical resistance at irradiation stages II and III (see Fig. 3) is explained by the interaction of newly forming radiation defects with the defect structure arising after annealing. At some concentration of defects, avalanche formation of microcracks and increase in electrical resistance at a fluence $8.1 \cdot 10^{19}$ neutrons/cm^2 are observed. The validity of the proposed mechanism of structural changes is supported by the destruction of the specimen with heating during annealing stage III.

LITERATURE CITED

1. M. S. Koval'chenko et al., Radiation Damage of Refractory Compounds [in Russian], Atomizdat, Moscow (1979).
2. V. V. Ogorodnikov, L. M. Murzin, and A. G. Krainii, in: Radiation Induced Changes in Mechanical Properties of Structural Materials and Methods for Studying Them [in Russian], Naukova Dumka, Kiev (1977), p. 116.
3. L. S. Topchyan et al., At. Energ., 42, No. 3, 226 (1977).
4. V. A. Stepanov, in: Problems of Strength and Plasticity of Solids [in Russian], Nauka, Leningrad (1979), p. 13.
5. G. N. Tret'yachencko, "Carrying capacity of structural elements of machines with nonstationary thermal loads," Doctoral Dissertation, Kiev (1964), p. 380.
6. R. A. Andrievskii, A. G. Lanin, and G. A. Rymachevskii, Strength of Refractory Compounds [in Russian], Metallurgiya, Moscow (1974).

Declassified and Approved For Release 2013/02/06 : CIA-RDP10-02196R000300020002-8

Declassified and Approved For Release 2013/02/06 : CIA-RDP10-02196R000300020002-8

VACUUM FISSION CHAMBER WITH COMPENSATION OF γ-INDUCED CURRENT

Yu. P. Bakulin, E. K. Malyshev,
S. V. Chuklyaev, and O. I. Shchetinin

UDC 539.1.074.8

Many experiments performed with pulsed nuclear reactors (PNR) [1, 2] require determining the time dependence of the flux density of fast neutrons with an error not exceeding 30%. One of the most promising pulsed neutron flux detectors is a vacuum fission chamber (VFC).

The temporal resolution of a VFC is $\leqslant 5 \cdot 10^{-9}$ sec; the radiation resistance is limited by the fluence $\sim 10^{19}$ neutrons/cm^2, and the linearity of the amplitude characteristics by $\sim 10^{20}$ neutrons/(cm^2·sec). In addition, a VFC is convenient in that depending on the substance used for the fission fragment radiator, the same construction can be used to assemble detectors with different energy sensitivity to neutrons.

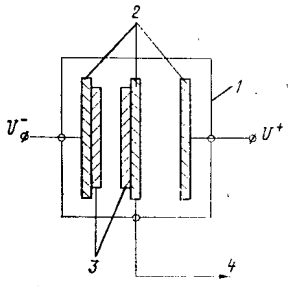

Fig. 1

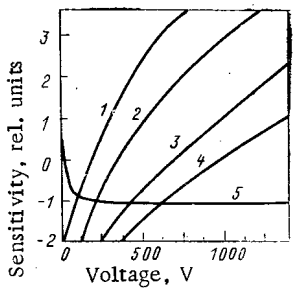

Fig. 2

Fig. 1. Diagram of the VFCC: 1) housing; 2) electrodes; 3) radiator of fission products; 4) electrical outlet to recorder.

Fig. 2. Sensitivity of the VFCC to γ quanta of the isotopic source ^{60}CO as a function of voltage U^+, with the voltage U^- equal to −100 (1), −200 (2), −400 (3), −600 V (4), and $U^- = -U^+ < 0$ (5).

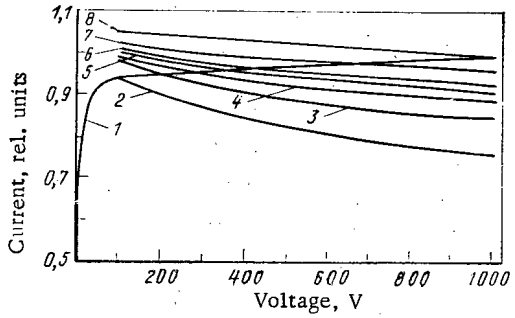

Fig. 3. Dependence of the sensitivity of the VFCC with a ^{235}U radiator to thermal neutrons on the voltage U^+ with the voltage U^- equal to −100 (2), −200 (3), −300 (4), −400 (5), −500 (6), −700 (7), and −1000 V (8), and $U^- = -U^+ < 0$ (1).

Translated from Atomnaya Énergiya, Vol. 54, No. 2, pp. 123-124, February, 1983. Original article submitted February 26, 1981; revision submitted July 5, 1982.

 0038-531X/83/5402-0136$07.50 © 1983 Plenum Publishing Corporation

Declassified and Approved For Release 2013/02/06 : CIA-RDP10-02196R000300020002-8

Declassified and Approved For Release 2013/02/06 : CIA-RDP10-02196R000300020002-8

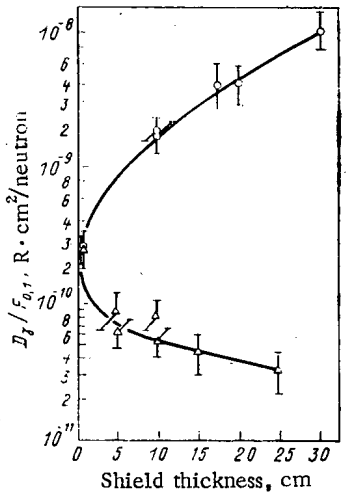

Fig. 4. The ratio $D_\gamma/F_{0.1}$ as a function of the thickness of the cylindrical guards made of granulated polyethylene (○) and lead (Δ).

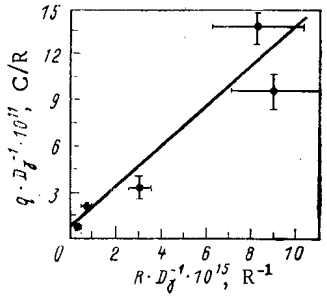

Fig. 5. qD^{-1}_γ as a function of RD^{-1}_γ with a voltage of ±500 V on the VFCC.

An important disadvantage of two-electrode VFC designs described in [3-5] is their high sensitivity to γ radiation.

In this paper we describe a three-electrode VFC design with compensation of the current from γ radiation (VFCC) with a ^{235}U radiator. The detector consists of 15 plane-parallel electrodes, forming seven sections sensitive to neutrons and γ radiation and the same number of sections sensitive only to gamma radiation. The sections are assembled in pairs so that the emitter of the γ-sensitive section is a collector for the section sensitive to neutrons (Fig. 1), and are confined in an evacuated housing which fulfills the function of a protective electrode. The total area of the U_3O_8 radiator (90% ^{235}U) of the VFCC is 175 cm². The VFCC construction is similar to the construction of a type KNV-1 VFC [4]. When a signal is recorded, the electrical potential U^+ on the electrodes of the γ-sensitive section and U^- on the electrode section sensitive to neutrons have opposite signs, which ensures compensation of the current formed by slow electrons created by γ quanta in the signal electrode circuit. The fast electron current is compensated partially by properly selecting the materials for the elements of the structure.

Figure 2 shows the characteristic of the sensitivity of VFCC, obtained using the isotopic γ source ^{60}Co. Its characteristic feature is the existence of points of total current compensation, and, in addition, the slope at the compensation points η_γ does not exceed 10^{-13} C/(R·V). In addition, up to 10^7 R/sec (1 R = $2.58 \cdot 10^{-4}$ C/kg), the combined relative error in detecting the signal from neutrons δ at points of compensation is determined by the expression

$$\delta \approx \eta_\gamma R_L P_\gamma \ll 1,$$

where R_L is the load resistance.

Figure 3 shows the sensitivity characteristic obtained in the thermal neutron field. It is evident that its slope depends weakly on the potentials U^+ and U^- with $\min\{|U^+|, |U^-|\} >$

Declassified and Approved For Release 2013/02/06 : CIA-RDP10-02196R000300020002-8

Declassified and Approved For Release 2013/02/06 : CIA-RDP10-02196R000300020002-8

100 V and does not exceed 0.04%/V. As follows from Figs. 2 and 3, compensation of the current from γ rays in the detector is possible without appreciable distortions of the signal from the neutrons.

The sensitivity of the VFCC to neutrons K_n under the condition of complete collection of electrons from secondary emission is related to the characteristics of the detector by the relation

$$K_n = \frac{\alpha S N_A \rho e \bar{\sigma}}{A}, \quad (1)$$

where α = 370 is the coefficient of secondary emission of electrons [6]; S = 87.5 cm^2, area of the radiator surface generating the secondary electrons; $N_A = 6.02 \cdot 10^{23}$, Avogadro's number, $mole^{-1}$; $e = 1.6 \cdot 10^{-19}$, charge on the electron, C; $\rho = 10^{-3}$, surface density of the ^{235}U radiator, g/cm^2; A = 235 amu, atomic mass of ^{235}U; and $\bar{\sigma}$, average cross section of neutron fissioning of ^{235}U. From here we calculated $K_n/\bar{\sigma} = 1.3 \cdot 10^4$ C.

The signal of the VFCC I on a pulsed nuclear reactor is related to the density of the neutron flux φ_n and intensity of the γ dose P_γ by the relation

$$I = K_n \varphi_n + K_\gamma P_\gamma, \quad (2)$$

where K_γ is the sensitivity of the VFCC to γ radiation.

Substituting (1) into relation (2), we obtain

$$I = K \bar{\sigma} \varphi_n + K_\gamma P_\gamma, \quad (2a)$$

where $K = \frac{\alpha S N_A \rho e}{A} = \text{const}.$

We determined the constant K on a pulsed nuclear reactor by varying the ratio of the γ dose D_γ and the neutron fluence F with cylindrical guards made of granulated polyethylene and lead. The characteristics of the γ–neutron field inside the guard are presented in Fig. 4. We obtained the fluence of neutrons with energy exceeding 0.1 MeV ($F_{0.1}$) from indications of track detectors with ^{238}Pu and ^{237}Np radiators and an activation ^{32}S detector using the technique in [7], and we found D_γ from the indications of solid-state luminescent IKS-type dosimeters. The neutron fluence F is related to the indications of track detectors with radiator ^{235}U (number of nuclei N_n is known), which were placed in the same screen made of ^{10}B with a thickness of 1.8 g/cm^2 as in the VFCC, by the relation

$$F = \frac{R}{\bar{\sigma}} = \frac{N_{tr}}{\bar{\sigma} N_n 0{,}92}, \quad (3)$$

where N_{tr} is the number of tracks of fission fragments recorded by the detector. It follows from (2a) and (3) and $qD_\gamma^{-1} = KRD_\gamma^{-1} + K_\gamma$, where q is the electric charge passing in the circuit of the signal electrode of the VFCC in one pulse of the pulsed nuclear reactor.

A graph of qD_γ^{-1} as a function of RD_γ^{-1} is shown in Fig. 5. From the graph we determine $K_\gamma = (0.7 \pm 0.4) \cdot 10^{-11}$ C/R; $K = (1.3 \pm 0.8) \cdot 10^4$ C.

Thus, as a result of the calculation, we obtain the value $K_n \bar{\sigma}^{-1} = 1.3 \cdot 10^4$ C. This quantity, measured on a pulsed nuclear reactor, turned out to equal $(1.3 \pm 0.8) \cdot 10^4$ C. The value of K_γ for ^{60}Co constituted $(0.8 \pm 0.1) \cdot 10^{-11}$ C/R; for the radiation from the PNR $K_\gamma = (0.7 \pm 0.3) \cdot 10^{-11}$ C/R.

The ratio K_n/K_γ (for $\bar{\sigma} = (1.21 \pm 0.02) \cdot 10^{-24}$ cm^2 [8]) constitutes $2.3 \cdot 10^{-9}$ R·cm^2/neutron, which results in a contribution of the signal from the γ radiation in the total signal from the VFCC on the PNR of not greater than 10%, which can be decreased by increasing the potential U^+ to values ensuring complete compensation of the current from the γ radiation.

LITERATURE CITED

1. A. I. Smirnov et al., Preprint IAÉ-1200, Moscow (1966).
2. Research Pulsed Reactors, AINF-125(OB), Atomizdat, Moscow (1972).
3. E. K. Malyshev, A. B. Dmitriev, and V. G. Belozerov, At. Energ., 27, No. 4, 347 (1969).
4. A. B. Dmitriev, E. K. Malyshev, and O. I. Shchetinin, ibid., 47, No. 2, 108 (1979).
5. K. Friddell and A. Lowrey, IEEE Trans. Nucl. Sci., 6, NS-18, 190 (1971).
6. J. Anno, J. Appl. Phys., 33, No. 5, 1678 (1962).

Declassified and Approved For Release 2013/02/06 : CIA-RDP10-02196R000300020002-8

Declassified and Approved For Release 2013/02/06 : CIA-RDP10-02196R000300020002-8

7. S. Yu. Nozdrachev and V. N. Sinev, in: Abstracts of Reports at the 3rd All-Union Conference on Metrology of Neutron Radiation in Reactors and Accelerators, Moscow (1982), p. 107.
8. S. N. Kraitor, T. V. Kuznetsova, and K. K. Kushnereva, in: Proceedings of the First All-Union School on Metrology of Neutron Measurements in Nuclear Physics Apparatus, Vol. 2, TsNIIatominform, Moscow (1976), p. 79.

NEUTRON FIELDS FOR RESEARCH IN THE IR-100 REACTOR

S. A. Barabanov, G. A. Borisov,
E. I. Grigor'ev, I. N. Martem'yanov,
V. D. Sevast'yanov, G. B. Tarnovskii,
and V. P. Yaryna

UDC 621.039.51

The modified version of the IR-100 [1] is a water-moderated, graphite-reflected research reactor developing up to 200 kW. A large number of experimental channels and cavities in the core, in its immediate vicinity, and in the reflector permits scientific and technological research in the fields of radiation effects on materials and nuclear power in neutron fields of various spectral compositions. Current research in this reactor assumes the existence of detailed information on the characteristics of these radiation fields, in particular the neutron spectrum over a wide energy range.

In this article we have selected a central experimental channel (CEC) at the core center, and an outer experimental channel (OEC-4) in the graphite reflector at the level of the core center. The study was designed to provide constant characteristics of these neutron fields and to determine with a standardized accuracy the relation between quantities which depend on the power level and readings of a special monitor.

As a constant characteristic of the neutron field we used the neutron spectrum $\varphi_0(E)$ — the energy dependence of the differential neutron flux — with the normalization condition $\int_{0.5\,eV}^{18\,MeV} \varphi_0(E)\,dE = 1$. The thermal neutron field was described by integral characteristics: the relative neutron flux Φ_0, defined as the number of neutrons per cm^3 times the velocity $v_0 = 2.2 \times 10^5$ cm/sec with normalization as for $\varphi_0(E)$; the epithermal parameter r characterizing the ratio of the epithermal and thermal components of the neutron field; and the parameter β in the expression $E^{-(1-\beta)}$ representing the epithermal neutron spectrum.

During a specific measurement procedure the neutron flux in these channels was determined by the scale factor K_M calculated from the monitor readings:

$$\Phi = K_M \Phi_0, \text{ neutrons/cm}^2 \cdot \text{sec}; \quad (1)$$

$$\varphi(E) = K_M \varphi_0(E), \text{ neutrons/cm}^2 \cdot \text{sec} \cdot \text{MeV}. \quad (2)$$

Neutron fields in the IR-100 are monitored with standardized sulfur detector-monitors based on the $^{32}S(n, p)^{32}P$ reaction, using the standard procedure [2] for determining the reaction rate R_S in a standard field. In this case $K_M = R_S/R_S^0$, where R_S^0 is the reaction rate corresponding to $\varphi_0(E)$.

Thermal-neutron-activation, resonance, threshold, and combination detectors of both standard [3] and special types (~30 types) were employed. In making measurements in the CEC, miniature boron screens were used.

The neutron spectrum was determined by using the PROSPEKT [4] procedure and computer program, and the characteristics of the thermal neutron field were found by following the procedure in [5].

Translated from Atomnaya Énergiya, Vol. 54, No. 2, pp. 124-125, February, 1983. Original article submitted September 7, 1981.

0038-531X/83/5402-0139$07.50 © 1983 Plenum Publishing Corporation

Declassified and Approved For Release 2013/02/06 : CIA-RDP10-02196R000300020002-8

Declassified and Approved For Release 2013/02/06 : CIA-RDP10-02196R000300020002-8

TABLE 1. Differential Neutron Spectra in OEC-4 and CEC of IR-100 Reactor

Energy (MeV)	φ(E), neutrons/cm² · sec · MeV		Energy (MeV)	φ(E), neutrons/cm² · sec · MeV	
	OEC-4	CEC		OEC-4	CEC
$5 \cdot 10^{-7}$	$1{,}57 \cdot 10^{5}$	$5{,}53 \cdot 10^{4}$	2,4	$2{,}48 \cdot 10^{-2}$	$7{,}31 \cdot 10^{-2}$
$1 \cdot 10^{-6}$	$7{,}45 \cdot 10^{4}$	$2{,}88 \cdot 10^{4}$	2,6	$2{,}27 \cdot 10^{-2}$	$6{,}50 \cdot 10^{-2}$
$5 \cdot 10^{-6}$	$1{,}37 \cdot 10^{4}$	$6{,}59 \cdot 10^{3}$	2,8	$2{,}00 \cdot 10^{-2}$	$5{,}80 \cdot 10^{-2}$
$1 \cdot 10^{-5}$	$6{,}56 \cdot 10^{3}$	$3{,}38 \cdot 10^{3}$	3,0	$1{,}77 \cdot 10^{-2}$	$5{,}35 \cdot 10^{-2}$
$5 \cdot 10^{-5}$	$1{,}18 \cdot 10^{3}$	$7{,}14 \cdot 10^{2}$	3,2	$1{,}58 \cdot 10^{-2}$	$4{,}97 \cdot 10^{-2}$
$1 \cdot 10^{-4}$	$5{,}69 \cdot 10^{2}$	$3{,}67 \cdot 10^{2}$	3,4	$1{,}4 \cdot 10^{-2}$	$4{,}63 \cdot 10^{-2}$
$5 \cdot 10^{-4}$	$1{,}08 \cdot 10^{2}$	[illegible]7	3,6	$1{,}3 \cdot 10^{-2}$	$4{,}71 \cdot 10^{-2}$
$1 \cdot 10^{-3}$	54,0	[illegible]1	3,8	$1{,}1 \cdot 10^{-2}$	$3{,}80 \cdot 10^{-2}$
$5 \cdot 10^{-3}$	10,7	[illegible]84	4,0	$9{,}6 \cdot 10^{-3}$	$3{,}31 \cdot 10^{-2}$
$1 \cdot 10^{-2}$	5,35	4,68	4,5	$7{,}19 \cdot 10^{-3}$	$2{,}47 \cdot 10^{-2}$
$2 \cdot 10^{-2}$	2,81	2,41	5,0	$5{,}10 \cdot 10^{-3}$	$1{,}77 \cdot 10^{-2}$
$4 \cdot 10^{-2}$	1,55	1,24	5,5	$3{,}74 \cdot 10^{-3}$	$1{,}05 \cdot 10^{-2}$
$6 \cdot 10^{-2}$	1,08	0,838	6,0	$2{,}55 \cdot 10^{-3}$	$6{,}42 \cdot 10^{-3}$
$8 \cdot 10^{-2}$	0,825	0,636	7,0	$1{,}41 \cdot 10^{-3}$	$3{,}11 \cdot 10^{-3}$
0,1	0,695	0,514	8,0	$6{,}95 \cdot 10^{-4}$	$1{,}61 \cdot 10^{-3}$
0,2	0,364	0,340	9,0	$3{,}09 \cdot 10^{-4}$	$8{,}22 \cdot 10^{-4}$
0,4	0,179	0,273	10,0	$1{,}39 \cdot 10^{-4}$	$4{,}21 \cdot 10^{-4}$
0,6	0,117	0,236	11,0	$6{,}93 \cdot 10^{-5}$	$2{,}10 \cdot 10^{-4}$
0,8	$8{,}87 \cdot 10^{-2}$	0,196	12,0	$3{,}45 \cdot 10^{-5}$	$1{,}04 \cdot 10^{-4}$
1,0	$7{,}33 \cdot 10^{-2}$	0,169	13,0	$1{,}66 \cdot 10^{-5}$	$5{,}01 \cdot 10^{-5}$
1,2	$5{,}96 \cdot 10^{-2}$	0,142	14,0	$7{,}82 \cdot 10^{-6}$	$2{,}35 \cdot 10^{-5}$
1,4	$4{,}86 \cdot 10^{-2}$	0,122	15,0	$3{,}64 \cdot 10^{-6}$	$1{,}09 \cdot 10^{-5}$
1,6	$3{,}99 \cdot 10^{-2}$	0,106	16,0	$1{,}69 \cdot 10^{-6}$	$5{,}08 \cdot 10^{-6}$
1,8	$3{,}43 \cdot 10^{-2}$	$9{,}57 \cdot 10^{-2}$	17,0	$7{,}74 \cdot 10^{-7}$	$2{,}33 \cdot 10^{-6}$
2,0	$3{,}06 \cdot 10^{-2}$	$8{,}88 \cdot 10^{-2}$	18,0	$3{,}57 \cdot 10^{-7}$	$1{,}06 \cdot 10^{-6}$
2,2	$2{,}73 \cdot 10^{-2}$	$7{,}96 \cdot 10^{-2}$			

Neutron fields in the IR-100 have been studied systematically since 1976, and the spectral characteristics obtained from these measurements show good reproducibility. We present below the results of these studies based on data taken during these years.

1. The errors in the determination of the neutrons spectrum φ_0 (E) in the CEC and OEC-4 (Table 1) are as follows (confidence coefficient P = 0.95) for the various neutron energy ranges: 0.5 eV-1 keV, no more than 10%; 1 keV-0.3 MeV, 20%; 0.3-10 MeV, 7%; 10-18 MeV, 15%. Application of the procedure in [5] to the integral measurements gave $\beta = 0.06 \pm 0.015$ for the CEC and $\beta = 0.04 \pm 0.015$ for the OEC-4, which agree with the spectrum $\varphi_0(E)$.

2. The epithermal parameter in the form $r\sqrt{T/T_0}$, where T is the effective temperature of the thermal neutrons and $T_0 = 293.4°K$, is equal to 0.056 for the CEC and 0.0094 for the OEC-4. The error was estimated as 7% (P = 0.95).

3. The normalized relative neutron flux Φ_0 is 0.447 and 7.17 neutrons/cm² sec for the CEC and OEC-4, respectively. The error of the determination does not exceed 5%.

4. The scale factor for use with the sulfur detector-monitors is 3.75×10^{25} R_S for the CEC and 1.18×10^{26} R_S for the OEC-4. The random error in the determination of K_M does not exceed 1% (P = 0.95).

From studies of the neutron fields in the IR-100 reactor, standard neutron sources OI-R-3 and OI-T-12 were constructed, forming the basis of the system of standardizing neutron measurments in this reactor.

LITERATURE CITED

1. Yu. M. Bulkin et al., At. Energ., 21, 363 (1966).
2. R. D. Vasil'ev, E. I. Grigor'ev, and V. P. Yaryna, in: Metrology of Neutron Measurements at Nuclear Physics Facilities [in Russian], Vol. 2, TSNIIatominform, Moscow (1976), p. 43.
3. E. I. Grigor'ev and V. P. Yaryna, Izmer. Tekh., 9, 61 (1980).
4. E. I. Grigor'ev et al., Techniques, Technology, Economics. Interindustrial Handbook, Ser. T, No. 49, RD-16/110 [in Russian], (1980).
5. V. P. Yaryna, [2], p. 17.

Declassified and Approved For Release 2013/02/06 : CIA-RDP10-02196R000300020002-8

Declassified and Approved For Release 2013/02/06 : CIA-RDP10-02196R000300020002-8

KINETICS OF TWO STRONGLY COUPLED PULSED REACTORS

A. V. Lukin

UDC 621.039.51

A point approximation has been developed for describing neutron transition processes in coupled reactor systems [1-3]. The kinetics of two coupled pulsed reactors has been considered by many researchers [4, 5] in a two-point approximation. An attempt to derive applicability criteria of the single-point approximation for analyzing the kinetics of such a system was made for the first time in [3]. The goal of the present work is to derive and establish the applicability limits of the single-point model of neutron transition processes in two strongly coupled pulsed reactors.

Let us consider transition processes of prompt neutrons. The processes are assumed to occur in two coupled pulsed reactors, the kinetics of each of which can be described in the single-point approximation. The fission intensity $n_i(t)$ (i = 1, 2) in the reactor satisfies the following equations [3]:

$$l_{i0}n_i(t)=\Delta K_i(t)\,n_i(t)+\sum_{j=1}^{2}K_{ij}\int_0^t dt' f_{ij}(t-t')\,n_j(t')+K_i q_i(t);\ n_i(t=0)=n_{i0},\quad i=1,\ 2 \tag{1}$$

where $\Delta K_i = K_i(1-\beta_i)-1$; l_{i0} and K_i are the lifetime of the prompt neutrons and the effective neutron multiplication coefficient for the i-th isolated reactor; K_{ij}, coupling parameter of the i-th and j-th reactors, the parameter resulting from the prompt neutrons only; $f_{ij}(\tau)$, functions normalized to unity and describing the intensity of the neutron interaction of the i-th and j-th reactors; and β_i, $q_i(t)$, effective fraction of delayed neutrons and the independent neutron source in the i-th reactor.

According to [3], the straight and conjugated conditionally critical problems can be stated as follows:

$$(\Delta K_i-\delta K)\,g_i+\sum_{j=1}^{2}K_{ij}g_j=0;\quad i=1,\ 2; \tag{2}$$

$$(\Delta K_i-\delta K)\,g_i^{+}+\sum_{j=1}^{2}K_{ji}g_j^{+}=0;\quad i=1,\ 2, \tag{3}$$

where

$$\sum_{i=1}^{2}g_i=1;\quad \sum_{i=1}^{2}g_i^{+}g_i=1. \tag{4}$$

The subcriticality δK of the coupled system is defined as the maximum-magnitude root of the equation

$$\delta K^2-(\Delta\bar{K}_1+\Delta\bar{K}_2)\,\delta K+\Delta\bar{K}_1\Delta\bar{K}_2-K_{12}K_{21}=0, \tag{5}$$

where $\Delta\bar{K}_i = \Delta K_i + K_{ii}$. When the deviation of the system from the state of criticality is small, δK is defined in the following fashion within the theory of small perturbations [6] at unchanged K_{ij} values:

$$\delta K=\sum_{i=1}^{2}g_{i0}^{+}\delta K_i g_{i0}=\frac{L_0^{-1}K_{21}\delta K_1+L_0K_{12}\delta K_2}{L_0K_{12}+L_0^{-1}K_{21}}. \tag{6}$$

The notation is interpreted as follows: $L_0 = g_{20}/g_{10}$; $\delta K_i = \Delta K_i - \Delta K_{i0}$ is the perturbation of the subcriticality of the i-th reactor; and the subscript "0" denotes the state of criticality of the coupled system ($\delta K = 0$).

Translated from Atomnaya Énergiya, Vol. 54, No. 2, pp. 125-127, February, 1983. Original article submitted October 22, 1981; revision submitted September 23, 1983.

0038-531X/83/5402-0141$07.50 © 1983 Plenum Publishing Corporation

Declassified and Approved For Release 2013/02/06 : CIA-RDP10-02196R000300020002-8

Declassified and Approved For Release 2013/02/06 : CIA-RDP10-02196R000300020002-8

Let us assume that when the integrals on the right side of Eq. (1) are calculated, the form of the functions $f_{ij}(\tau)$ makes it possible to limit the expansion of $n_j(t')$ in a Taylor series of the variable $t - t'$ to two terms. In this approximation Eq. (1) assumes the form

$$l_i n_i(t) = \Delta\bar{K}_i(t)\, n_i(t) + K_{ij} n_j(t) + K_i q_i(t), \quad j \neq i, \quad j = 1, 2; \tag{7}$$

$$l_i = l_{i0} + K_{ii}\tau_{ii} + K_{ij}\tau_{ij}\dot{n}_j(t)/\dot{n}_i(t), \quad j \neq i, \quad i = 1, 2;$$

$$\tau_{ij} = \int_0^\infty d\tau\tau f_{ij}(\tau), \quad j, i = 1, 2.$$

We represent the fission intensity in the reactors in the form of products $n_i(t) = p_i(t)n(t)$ $(i = 1, 2)$, where $n(t) = n_1(t) + n_2(t)$ is the total fission intensity in the coupled system. By subtracting the sum of Eqs. (3) (the first one of which was first multiplied by $n_1(t)$, and the second by $n_2(t)$) from the sum of Eqs. (7) (the first of which was multiplied by $g_1^+(t)$, and the second by $g_2^+(t)$) and assuming that the inequality $|\dot{p}_i(t)/p_i(t)| \ll |\dot{n}(t)/n(t)|$, $(i = 1, 2)$ holds we obtain equations for the kinetics of the coupled system in the single-point approximation:

$$l\dot{n}(t) = \delta K n(t) + q(t). \tag{8}$$

When we ignore in Eqs. (7) the independent sources and the initial conditions within the assumptions used in the derivation of Eq. (8), we obtain equations for the determination of $p_i(t)$:

$$(l_i^{-1}\Delta K_i - l^{-1}\delta K)\, p_i + \sum_{j=1}^{2} l_i^{-1} K_{ij} p_j = 0, \quad i = 1, 2. \tag{9}$$

When the deviation of the coupled system from the state of criticality is small, we can assume in accordance with Eqs. (2), (3), and (9):

$$g_i^+(t) \approx g_{i0}^+; \quad g_i'(t) \approx g_{i0}; \quad p_i'(t) \approx g_{i0}; \quad i = 1, 2. \tag{10}$$

In this case the single-point reactor characteristics l and A (quasistatic feedback coefficient [7]), the initial conditions n_0, and the independent sources q(t) for Eq. (8) are defined as follows:

$$l = \sum_{i=1}^{2} g_{i0}^+ l_i g_{i0} = \frac{L_0^{-1}K_{21}l_1 + L_0 K_{12} l_2}{L_0 K_{12} + L_0^{-1} K_{21}}; \tag{11a}$$

$$l_i = l_{i0} + K_{ii}\tau_{ii} + K_{ij}\tau_{ij}\frac{g_{j0}}{g_{i0}}, \quad j \neq i, \quad i = 1, 2; \tag{11b}$$

$$A = \sum_{i=1}^{2} g_{i0}^+ g_{i0} A_i g_{i0} = \frac{L_0^{-1}K_{21}A_1 + L_0^2 K_{12} A_2}{(1 + L_0)(L_0 K_{12} + L_0^{-1} K_{21})}; \tag{11c}$$

$$q(t) = \sum_{i=1}^{2} g_{i0}^+ K_i q_i(t) = (1 + L_0)\frac{L_0^{-1}K_{21}K_1 q_1(t) + K_{12}K_2 q_2(t)}{L_0 K_{12} + L_0^{-1} K_{21}}; \tag{11d}$$

$$n_0 = l^{-1}\sum_{i=1}^{2} g_{i0}^+ l_i n_{i0} = (1 + L_0)\frac{L_0^{-1}K_{21}l_1 n_{10} + K_{12}l_2 n_{20}}{L_0 K_{12} l_2 + L_0^{-1} K_{21} l_1}. \tag{11e}$$

We introduce the ratios

$$\frac{g_2(t)}{g_1(t)} = L_k(t) = L_0[1 + z_k(t)]; \tag{12a}$$

$$\frac{p_2(t)}{p_1(t)} = L_\lambda(t) = L_0[1 + z_\lambda(t)]. \tag{12b}$$

Equation (8) and the formulas (11) are applicable when the equalities of Eq. (10) hold. This means that according to Eqs. (12), the inequalities

$$\tau_{ij} \ll |\dot{n}(t)/n(t)|^{-1}; \quad j, i = 1, 2; \quad |z_k(t)| \ll 1; \; |z_\lambda(t)| \ll 1 \tag{13}$$

must be fulfilled during the transition process under consideration.

The first inequality in (13) makes it possible to switch from Eqs. (1) to the simpler Eqs. (7); the second and third inequalities indicate that the functions $g_i(t)$ and $p_i(t)$ do not change during the transition process. The system of the two reactors satisfying conditions (13) is termed "strongly coupled."

Declassified and Approved For Release 2013/02/06 : CIA-RDP10-02196R000300020002-8

Declassified and Approved For Release 2013/02/06 : CIA-RDP10-02196R000300020002-8

It follows from Eqs. (2), (9) that in the approximation which is linear in $\xi_{k,\lambda}$

$$z_k(t)=\frac{\xi_k(t)}{L_0K_{12}+L_0^{-1}K_{21}},\quad \xi_k(t)=\delta K_2(t)-\delta K_1(t);$$

$$z_\lambda(t)=\frac{\xi_\lambda(t)}{l_1^{-1}L_0K_{12}+l_2^{-1}L_0^{-1}K_{21}},\quad \xi_\lambda(t)=l_2^{-1}\delta K_2(t)-l_1^{-1}\delta K_1(t).$$

When a fission pulse takes place in the coupled system, it suffices to set $|\xi_{k,\lambda}(t)| \leqslant |\xi_{k,\lambda}(t=0)|$ as an estimate. It can be shown for reactors with quasistatic feedback [7] that $\delta K_i(t=0)=0.5A_iN_i$ (N_i is the total number of fission events during the pulse in the i-th reactor); in this case, $N_2=L_0N_1$. Then the formula relating the characteristic change in $p_i(t)$ during the pulse to the reactor characteristics assumes the form

$$|z_\lambda(t)| \leqslant |z_\lambda(t=0)|=\frac{0.5N_1|l_2^{-1}L_0A_2-l_1^{-1}A_1|}{l_1^{-1}L_0K_{12}+l_2^{-1}L_0^{-1}K_{21}}. \tag{14}$$

For example, in the case of two separate but coupled reactors, it follows from Eq. (14) that $\max_{L_0}|z_k(t)| \approx \max_{L_0}|z_\lambda(t)| \leqslant 0.21\delta K_1(t=0)/K_{12}$ at $L_0 \approx 0.41$.

Assume that the particular reaction system is strongly coupled. In this case, according to Eqs. (12) and (13), the integral parameters N_i, n_{mi}, and θ_i (total number of fissions per pulse, maximum fission intensity, and half-width of the pulse, respectively) of the fission pulses in the reactors are coupled among themselves and with the respective single-point parameters N, n_m, and θ by the following equations:

$$N_i=g_{i0}N,\ n_{mi}=g_{i0}n_m,\ \theta_i=\theta,\ t_{mi}=t_m,\ i=1,2; \tag{15}$$

$$\frac{N_2}{N_1}=\frac{n_{m2}}{n_{m1}}=\frac{g_{20}}{g_{10}}=L_0,\ \theta_1=\theta_2,\ t_{m1}=t_{m2}, \tag{16}$$

where t_{mi} and t_m are the times at which the fission intensities $n_i(t)$ and $n(t)$, respectively, reach their maximum values.

It is interesting to establish how Eq. (16) behaves at increasing $|z_\lambda|$, i.e., when the third of the limit inequalities (13) is disturbed. By substituting the formula for $p_i(t)$ in the approximation which is linear in $z_\lambda(t)$ into the formulas for the fission pulse parameters N and n_m, we obtain

$$\frac{N_2}{N_1} \approx L_0[1-0.5\dot{z}_\lambda(t_m)\theta(N_+-N_-)/N]; \tag{17}$$

$$\frac{n_{m2}}{n_{m1}} \approx L_0\left[1+\frac{L_0-1}{2(1+L_0)}\dot{z}_\lambda(t_m)\theta\right]; \tag{18}$$

$$\frac{\theta_2-\theta_1}{\theta} \approx \frac{L_0-1}{2(1+L_0)}\left[\frac{N_+-N_-}{N}+\dot{z}_\lambda(t_m)\tau_m\right]; \tag{19}$$

$$\tau_m=t_{m2}-t_{m1} \approx -\dot{z}_\lambda(t_m)\frac{\theta^2}{4}; \tag{20}$$

$$N_\pm=\int_0^\infty dx\, n(t_m \mp x).$$

In the case of coupled reactors with quasistatic feedback we have

$$\tau_m \approx \frac{A_1l_2-L_0A_2l_1}{L_0^{-1}K_{21}A_1+L_0K_{12}A_2}. \tag{21}$$

It follows from Eqs. (17)-(20) that in a system of coupled reactors with $\max_t|z_\lambda(t)| \leqslant \dot{z}_\lambda(t_m)\theta| \leqslant 1$ (almost strong coupling), the relations between the integral parameters of the fission pulses in the reactors differ only slightly from similar relations (see Eq. (16)) of a strongly coupled system. In this way, contrary to the conclusions of [4], the kinetics of a system of coupled reactors can be described with the single-point approximation under the specific conditions of Eq. (13).

LITERATURE CITED

1. R. Aiveri, in: Trans. 2nd Geneva Conf., Selected Reports of Western Scientists [Russian translation], Vol. 3, Atomizdat, Moscow (1958), p. 321.
2. A. Belleni-Morante, Nukleonik, 10, No. 4, 217 (1967).

Declassified and Approved For Release 2013/02/06 : CIA-RDP10-02196R000300020002-8

Declassified and Approved For Release 2013/02/06 : CIA-RDP10-02196R000300020002-8

3. A. V. Lukin, At. Energ., 50, No. 3, 205 (1981).
4. V. F. Kolesov, Yu. V. Petrov, and S. K. Shtarev, At. Energ., 39, No. 6, 392 (1975).
5. G. Thayer, G. Miley, and B. Jones, Nucl. Technol., 25, No. 1, 56 (1975).
6. E. A. Stumbur, Application of Perturbation Theory to the Physics of Nuclear Reactors [in Russian], Atomizdat, Moscow (1976).
7. E. P. Shabalin, Pulsed Fast-Neutron Reactors [in Russian], Atomizdat, Moscow (1976).

RADIATION DAMAGE TO TUNGSTEN SINGLE CRYSTALS BY AN ARG N ION BEAM

V. N. Bugrov and S. A. Karamyan

UDC 539.2:539.12.04

Research on the radiation damage produced in single crystals by heavy ions is of interest in solid-state physics and in certain parts of modern materials science. The interaction of heavy ions and single crystals has been studied in experiments in which the lifetime of composite nuclei was measured with the shadow effect in nuclear reactions occurring in single-crystal targets [1, 2]. It was established that the single-crystal structure of tungsten is conserved up to doses in excess of 10^{16} heavy ions with an energy of 6-8 MeV/nucleon per cm^2. The shadow technique has been used to investigate damage produced in tungsten single crystals by 24-MeV ^{40}Ar ions. The shadow technique was also used in modeling the influence of radiation damage upon measurements of the lifetime of a nucleus.

Experiment and Results. A thick tungsten single crystal was irradiated at room temperature with a collimated beam of ^{40}Ar ions (beam diameter 1 mm) from the U-300 cyclotron of the Laboratory of Nuclear Reactions of the Joint Institute of Nuclear Research. At a flux intensity of 10^{10} ions/sec, the heating of the irradiated volume by the beam did not exceed 1°C (according to theoretical estimates). The beam axis did not coincide with specific crystallographic directions. The two <111> crystallographic axes of the target formed the angles 90° and 161° with the direction of the beam. Track detectors of glass, which recorded the elastically scattered ^{40}Ar ions, were placed 120 mm from the target at scattering angles ranging

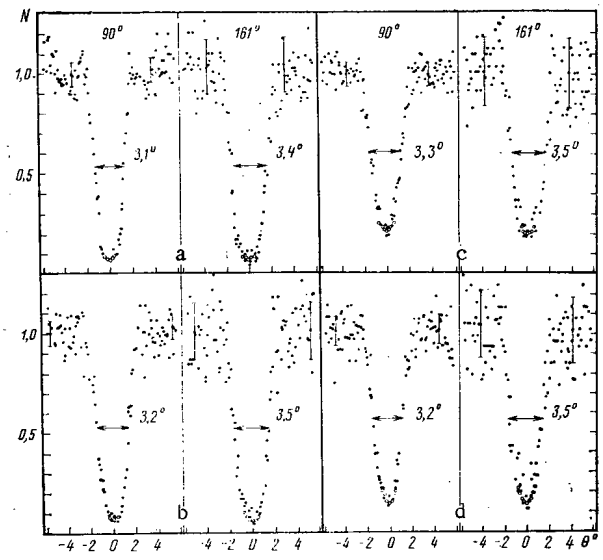

Fig. 1. Comparison of pairs of shadow minima determined for the angles 90° and 161° of the crystallographic <111> axis of a tungsten single crystal relative to the beam direction; ^{40}Ar ion doses of a) $7.4 \cdot 10^{13}$, b) $2.9 \cdot 10^{13}$, c) $7.8 \cdot 10^{14}$, and d) $4.5 \cdot 10^{14}$ cm^{-2}; ●, ○) results of transverse and annular scanning (with the error not exceeding the diameter of a point).

Translated from Atomnaya Énergiya, Vol. 54, No. 2, pp. 127-129, February, 1983. Original article submitted November 25, 1981.

 0038-531X/83/5402-0144$07.50 © 1983 Plenum Publishing Corporation

Declassified and Approved For Release 2013/02/06 : CIA-RDP10-02196R000300020002-8

Declassified and Approved For Release 2013/02/06 : CIA-RDP10-02196R000300020002-8

TABLE 1. Degree of Radiation Damage to Single Crystals

Target	Ion	Energy, MeV	Layer thickness, mg·cm^{-2}	r (±25 %), 10^{-18} cm^2	$r/Z_1^2Z_2^2E^{-1}\gamma$, 10^{-20} cm^2·MeV
UO_2	^{12}C	81	5,8	3,0	1,58
W	^{22}Ne	174	3,3	10,0	2,70
W	^{40}Ar	24	1,1	81	0,52 *
			2,3	196	1,21 †

*Using the range–energy relation on the basis of the results of [3].
†Using the range–energy relation on the basis of the results of [4].

from 75 to 170°. The density of the tracks produced by ^{40}Ar ions on the surface of the detector was $\sim 10^4$ mm^{-2} and therefore the shadow pattern could be visually observed. The shadow minima were scanned with an optical microscope to obtain the dependence of the track density upon the angle reckoned from the crystallographic axis. In this fashion the shadow profile, the shadow intensity χ in the minimum, and the angular width $\Psi_{1/2}$ at half the minimum were determined.

During a continuous irradiation of a single crystal, the glass detectors were repeatedly exchanged to follow the influence of the heavy-ion dose upon the form of the shadow minimum. According to Fig. 1, when the ion dose increases, the shadow minima for the crystallographic <111> axis become shallower. The angular width $\Psi_{1/2}$ was 3.2° for the 90° axis and 3.5° for the 161°; the difference is related to the dependence of the ion energy on the angle of scattering in the laboratory system. A substantial change in $\Psi_{1/2}$ does not occur at increasing radiation doses.

The number of ions which are incident on the target was obtained from the track density of the ions scattered under a certain angle in a direction not coinciding with a crystallographic direction. The yield of scattered particles for the thick target was determined by calculations. A range–energy relation in the form $E = \left(\frac{CR}{2}\right)^n$ was assumed, and the parameters C and n were selected from the condition of best fit to the range–energy relation of [3] or [4]. The thickness of the effective target layer in the direction of the beam can be obtained with the formula

$$d = \frac{k^{1/n}R(E_0) - R(\Pi)}{k^{1/n} + P(\theta)_L}, \qquad (1)$$

where E_0 is the initial particle energy in the laboratory system; Π, threshold energy of recording a particle with the detector; and $p(\theta_L)$, depth ratio of the point of scattering in the direction l of scattering and in the direction s of the incident particle ($p = l/s$). The function $k(\theta_L)$ relates the energy of the scattered particle and the incident particle in the laboratory system, i.e., $E(\theta_L) = Ek(\theta_L)$ [5]:

$$k(\theta_L) = (1+\gamma)^{-2}\left[1 + \gamma^2 - 2\gamma^2\sin^2\theta_L + 2\gamma\cos\theta_L\sqrt{1-\gamma^2\sin^2\theta_L}\right], \qquad (2)$$

where $\gamma = A_1/A_2$ is the ratio of the mass numbers of the ion and the target.

By integrating the Rutherford cross section over the interval of the effective target layer, the yield of the scattered ions can be determined in dependence upon the angle θ_c in the center-of-mass system:

$$N(\theta_c) = \Delta\Omega J \frac{\rho 6{,}02\cdot 10^{23}}{A_2} M(\theta_c)\frac{1}{(2n-1)}\left(\frac{2}{C}\right)^{2n}\left[\frac{1}{(R_0-d)^{2n-1}} - \frac{1}{R_0^{2n-1}}\right], \qquad (3)$$

where $\Delta\Omega$ is the solid angle of recording in the laboratory system (sr); J, total number of ions incident on the target; ρ, target density (g/cm^3); and $R_0 = R(E_0)$ (cm). The $M(\theta_c)$ value can be calculated with the formula of [5]:

Declassified and Approved For Release 2013/02/06 : CIA-RDP10-02196R000300020002-8

Declassified and Approved For Release 2013/02/06 : CIA-RDP10-02196R000300020002-8

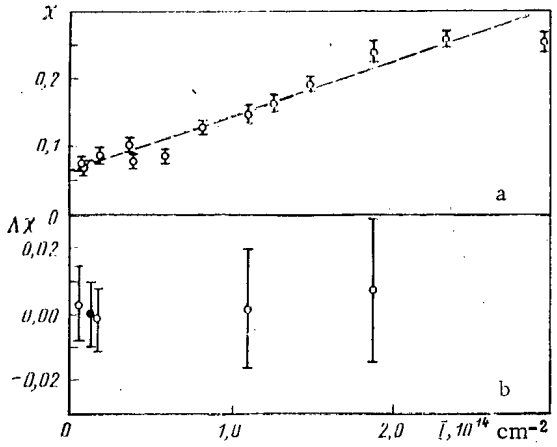

Fig. 2. Dependence of a) the depth $\chi = \chi_{161^\circ}$ and b) the depth difference $\Delta\chi$ of the shadow minima upon the irradiation dose; ● obtained for the purpose of checking, performed on a second sample of single-crystal tungsten.

$$M(\theta_c) = \frac{0{,}814 Z_1^2 Z_2^2 (1+\gamma^2+2\gamma\cos\theta_c)^{3/2}(1+\gamma)^2}{2\pi \sin^4 \theta_c/2\,|1+\gamma\cos\theta_c|}\, 10^{-26} \text{cm}^2 \cdot \text{MeV}^2 \cdot \text{sr}^{-1}, \quad (4)$$

where Z_1 and Z_2 denote the atomic numbers of the ion and the target, respectively.

The results of the calculation depend upon the parameters selected in the range–energy relation. For the argon energy range $\leqslant$ 0.6 MeV/nucleon, the range obtained in tungsten by employing the measured results of [4] is greater than that of [3] by a factor of 2. Such discrepancies are occasionally encountered at small ion energies and can be explained by Z fluctuations of the stopping power due to the shell structure of the stopping atom or the atoms of the medium. Therefore, two versions of the results obtained with the ion-range figures of [3] and [4] are listed in Table 1.

Discussion of the Results. Figure 2 shows the dependence of the depth χ_{161° of the shadow minimum and the depth differences $\Delta\chi = \chi_{90^\circ} - \chi_{161^\circ}$ of the two minima upon the dose density imparted to the single crystal. Dose values obtained under the assumption that the ion range corresponds to the measured values [4] were used. When the dose is increased to 10^{15} cm^{-2}, the χ value increases to 0.3. The $\chi(I)$ function can be approximated to some extent by a straight line $\chi(I) = rI + \chi_0$, where the coefficient r characterizes the damaging effect of the ion on the single crystal. The function $\chi(I)$ can be used to calculate the dependence of the defect concentration upon the dose, taking into account that the heavy ions do not move along a channel in a layer of finite thickness and making certain assumptions on the depth distribution of the defects.

Let us consider the damaging influence r of the heavy ions upon the single crystal. Table 1 lists the r values and the thickness of the effective target layer in the direction of the normal to the surface for the case of the W + ^{40}Ar (24 MeV) interaction, and the UO_2 + ^{12}C ^{12}C (81 MeV) and W + ^{22}Ne (174 MeV) interactions of [6]. The measurements of [6] were made with a similar technique when the fission products of nuclei but not elastically scattered ions were recorded. The damaging effect of the ^{40}Ar ions is greater than that of the ^{12}C and ^{22}Ne ions. This observation leads to the conclusion that r is correlated with the nuclear stopping power of the ion in the target material; in a simple fashion the nuclear stopping power can be estimated as $\sim Z_1^2 Z_2^2 E^{-1}\gamma$. Table 1 lists the $r/Z_1^2 Z_2^2 E^{-1}\gamma$ ratio, which does not strongly vary for the cases under consideration. This means that a certain correlation between the damage to a single crystal and the nuclear stopping power of the ion must exist. The remaining change in the $r/Z_1^2 Z_2^2 E^{-1}\gamma$ ratio must be ascribed to differences between the single crystals and the particles recorded.

The experiment can be considered a model experiment as far as the use of the shadow effect for measuring the time during which a nuclear reaction occurs is concerned. The geometry of the experiment precisely reproduces the geometry used in such measurements (see, e.g., [6]). The difference $\Delta\chi = \chi_{90^\circ} - \chi_{161^\circ}$ of the depth of the two shadows is measured under conditions

Declassified and Approved For Release 2013/02/06 : CIA-RDP10-02196R000300020002-8

Declassified and Approved For Release 2013/02/06 : CIA-RDP10-02196R000300020002-8

corresponding to a specific radiation damage of the single crystal. But in the present case the measurements were made for elastic ion scattering, the time delay of which is negligibly small (of the order of the collision time). Therefore, the results of our experiment can be used to determine whether an effect simulating a finite lifetime of a nuclear system results from technical reasons or from radiation damage to a single crystal. It should be noted that not only the geometrical conditions coincide, but that also the model experiment resembles the basic experiment, as far as the angular width values of the shadow minima and their ratio at the two angles of observation, the particle energy changes in dependence upon the angle of recording and the identical scales of those changes, and the thickness of the effective target layer are concerned. In this fashion the conditions of close modeling were conserved. Differences exist insofar as the time delay of the nuclear reaction does not exist in the model experiment.

Figure 2b displays the measured $\Delta\chi$ values in dependence upon the dose density of the ^{40}Ar ions. The $\Delta\chi$ values are close to zero in the model experiment. Since in the case of a reaction with a small time delay the $\Delta\chi$ values do not differ from zero (within the limits of measurement errors) up to high doses corresponding to a considerable damage to single crystals, nonvanishing $\Delta\chi$ values observed in a fission reaction of nuclei [6] must be associated with a time delay of the nuclear reaction rather than with some technical details.

The authors thank G. N. Flerov and Yu. Ts. Oganesyan for their interest in the present work, G. Otto for providing the tungsten single crystal, L. V. Dzholos for help in the chemical preparation of the track detectors, and the group of the U-300 cyclotron operators for providing the beams with the required parameters.

LITERATURE CITED

1. S. A. Karamyan et al., Yad. Fiz., 13, 944 (1971).
2. S. A. Karamyan, Yu. Ts. Oganesyan, and F. Normuratov, Yad. Fiz., 14, 499 (1971).
3. L. Northcliffe and R. Schilling, Nucl. Data Tables, A7, 233 (1970).
4. H. Pape, H. Clerc, and K. Schmidt, Z. Phys., A286, 159 (1978).
5. Experimental Nuclear Physics [Russian translation], Vol. 1, p. 212; Vol. 2, p. 9, IL, Moscow (1955).
6. V. N. Bugrov and S. A. Karamyan, Yad. Fiz., 35, 558 (1982).

COMPARATIVE NEUTRON-PHYSICS CALCULATIONS OF FAST REACTORS

I. D. Iordanov and N. A. Antonov

UDC 621.039.526:621.039.516.23

Nuclear power stations with fast reactors are aquiring even greater importance in the development of nuclear power generation. Work on fast reactors and the expansion of international cooperation in this field leads to the necessity for standarizing reactor calculations, i.e., to the development of a unified approach and to the need for determining reactor characteristics and their accuracy. In connection with this, experiments are being developed for the calculation of different test models of fast reactors. This will allow different sets of nuclear data to be compared, and will also allow different program combinations to be compiled for the neutron-physics analysis of fast power reactors.

An important stage of the neutron-physics analysis of fast reactors is the determination of the effective multigroup cross section [1]. Based on the formalism of self-screening factors [2], the PRIDAN program has been developed in the Institute of Nuclear Research and Nuclear Power (IYaIYaÉ), preparing the effective cross-sections of media which are characteristic for fast reactors. The starting data [3, 4] are obtained using the library of multigroup constants for fast reactors, BNDL [5].

The dilution cross section for the energy group i and element j is determined by the formula

Institute of Nuclear Research and Nuclear Power, Bulgarian Academy of Sciences, Sofia.
Translated from Atomnaya Énergiya, Vol. 54, No. 2, pp. 129-132, February, 1983. Original article submitted January 8, 1982.

0038-531X/83/5402-0147$07.50 © 1983 Plenum Publishing Corporation

Declassified and Approved For Release 2013/02/06 : CIA-RDP10-02196R000300020002-8

Declassified and Approved For Release 2013/02/06 : CIA-RDP10-02196R000300020002-8

TABLE 1. Concentration of Elements and Reactor Dimensions

Parameters	Core	Shield
Concn. of elements, 10^{-24} cm^3		
Pu + U + FP *	0,0072	—
^{239}Pu	—	0,00012
^{238}U	—	0,012
Ni	0,00088	0,00088
Fe	0,00814	0,00814
Cr	0,00198	0,00198
Na	0,0123	0,0069
O	0,0144	0,024
Reactor: radius, cm	84,196	—
shield thickness, cm	—	45,72
number of reference intervals	14	8
length of intervals, cm	6,014	5,715

*FP indicates fission products.

TABLE 2. Fuel Composition, 10^{-24} cm^3

Element	Version A	Version B	Version C
^{239}Pu	0,000999	0,00106	0,00101
^{240}Pu	—	—	0,000507
^{238}U	0,006201	0,00542	0,00496
^{239}Pu fission products	—	0,00072	0,00072

TABLE 3. Values of k_{eff}

System of constants	Version A	Version B	Version C
BNDL	1,0825	1,0754	1,0714
BNDL-M	1,0076	1,0021	1,0019

TABLE 4. Neutron Balance

Element		Version A			Version B			Version C		
		P	F	C	P	F	C	P	F	C
Core	^{239}Pu	801,0	81,2	273,1	818,0	78	278	750,6	71,0	255,2
	^{240}Pu							78,3	50,5	25,9
	FP ^{239}Pu					58,5			54,5	
	^{238}U	120,4	275,8	42,8	105,1	231,8	37,2	96,0	203,4	34,2
	Ni		3,1			3,1			3,0	
	Fe		8,5			8,2			7,8	
	Cr		2,6			2,5			2,4	
	Na		3,0			2,8			2,7	
	O		2,6			2,6			2,6	
Shield	^{239}Pu	41,3	7,1	14,1	40,8	6,8	14,0	39,6	6,3	13,3
	^{238}U	37,3	222,0	13,0	36,2	218,0	13,3	35,5	211,0	13,1
	Ni		0,9			0,9			0,9	
	Fe		3,7			3,6			3,5	
	Cr		1,2			1,1			1,1	
	Na		0,9			0,87			0,8	
	O		0,7			0,66			0,6	
Total		1000,0	613,4	343,0	1000,0	612,0	342,7	1000,0	622,3	341,7
Leakage		35,9573			35,2644			34,0736		
k_{eff}		1,0076			1,0021			1,0019		

$$\sigma^i_{0,j} = \frac{1}{N_j} \sum_{m \neq j}^{NI} N_m \bar{\sigma}^i_{t,m}, \qquad (1)$$

where N_m is the concentration of the element m; NI, number of isotopes of given composition; and $\bar{\sigma}^i_{t,m}$, total effective microscopic cross section for the energy group i and element j.

The total effective cross section of each element of composition necessary for the calculation of the dilution cross section is determined by iteration. At the start of the iteration, instead of the unknown effective cross section in Eq. (1), the fundamental (unscreened) microscopic cross section is used. By means of this dilution cross section, the self-screening factors for the total cross section are determined, which are necessary for the correction of the preceding cross section, etc. The iteration process converges rapidly [6].

The total effective microscopic cross section is determined by two methods:

$$\bar{\sigma}^i_{t,j}(\sigma^i_{0,j}) = f^i_{t,j}(\sigma^i_{0,j})\langle\sigma^i_{t,j}\rangle; \qquad (2)$$

Declassified and Approved For Release 2013/02/06 : CIA-RDP10-02196R000300020002-8

Declassified and Approved For Release 2013/02/06 : CIA-RDP10-02196R000300020002-8

TABLE 5. Plutonium Breeding Characteristics

Parameter	Version		
	A	B	C
G_{core}	−0,239	−0,357	−0,091
G_{shield}	0,587	0,568	0,55
G	0,338	0,211	0,459
B_{core}	0,72	0,611	0,732
B_{shield}	0,591	0,579	0,613
B	1,311	1,19	1,345
BF	1,34	1,21	1,37

TABLE 6. Effect of the Fission Product Capture Cross Section for ^{239}Pu, b

Parameter	B-1			B-2			B-3		
	zone	shield	reactor	zone	shield	reactor	zone	shield	reactor
k_{eff}			1,0021			1,0051			1,002
Δk_{eff}, %			0			0,3			−0,001
G	−0,357	0,568	0,211	−0,357	0,567		−0,355	0,568	
B	0,611	0,579	1,19	0,610	0,577		0,611	0,579	
BF			1,213			1,21			1,213
^{238}U									
$\langle\sigma_c\rangle$	0,293	0,371		0,293	0,371		0,293	0,371	
^{239}Pu									
$\langle\sigma_f\rangle$	1,792	2,395		1,796	2,398		1,792	2,395	
$\langle\sigma_c\rangle$	0,501	1,161		0,504	1,164		0,501	1,161	
$\bar{\alpha}$	0,28	0,485		0,281	0,485		0,28	0,485	
^{240}Pu									
$\langle\sigma_f\rangle$	0,354	0,207		0,354	0,207		0,354	0,207	
$\langle\sigma_c\rangle$	0,813	1,984		0,817	1,988				
ω_0	0,0354	−0,334		0,0342	−0,335		0,0354	−0,334	

$$\bar{\sigma}^i_{t,j}(\sigma^i_{0,j}) = \sum_h f^i_{h,j}(\sigma^i_{0,j})\langle\sigma^i_{h,j}\rangle, \tag{3}$$

where summing is carried out over all reactions of the element j.

The transport microscopic cross section of the isotope j is calculated by the formula

$$\bar{\sigma}^i_{tr,j}(\sigma^i_{0,j}) = [\bar{\sigma}^i_{t,j}(\sigma^i_{0,j}) - \bar{\sigma}^i_{f,j}(\sigma^i_{0,j}) - \bar{\sigma}^i_{c,j}(\sigma^i_{0,j}) - \bar{\sigma}^i_{in,j}(\sigma^i_{0,j})](1-\mu^i_j) + \bar{\sigma}^i_{c,j}(\sigma^i_{0,j}) + \bar{\sigma}^i_{f,j}(\sigma^i_{0,j}) + \bar{\sigma}^i_{in,j}, \tag{4}$$

where $\bar{\sigma}^i_{c,j}$ and $\bar{\sigma}^i_{f,j}$ are the effective microscopic cross sections of capture and fission, respectively; $\bar{\sigma}^i_{in,j}$, effective inelastic scattering microscopic cross section; and μ^i_j, average cosine of the elastic scattering angle.

The effective macroscopic cross section for the reactions x (capture; elastic and inelastic scattering or fission) is determined by the formula

$$\Sigma_x = \sum_m^{NI} N_m \bar{\sigma}^i_{m,x}, \tag{5}$$

where $\bar{\sigma}^i_{m,x}$ is the effective microscopic cross section for the energy group i and the reaction x of the element m.

In order to determine the fission spectrum it is necessary to find the average number of neutrons formed during a single fission event:

$$\bar{\nu} = \frac{\sum_{c=1}^{NI}\sum_{k=1}^{NOG}\bar{\nu}^k_i\Sigma^k_{f,i}\Phi^k}{\sum_{j=1}^{NI}\sum_{k=1}^{NOG}\Sigma^k_{f,i}\Phi^k}, \tag{6}$$

where NOG is the number of energy groups; $\bar{\nu}^k_i$, average number of fission neutrons in the energy group k, formed during fission of the isotope i; Φ^k, neutron flux; and $\Sigma^k_{f,i}$, effective macroscopic fission cross section of the element i.

The flux Φ^k depends on the fission spectrum, and therefore in order to determine $\bar{\nu}$ the iteration process is used. Iteration is started for the spectrum which corresponds to the

Declassified and Approved For Release 2013/02/06 : CIA-RDP10-02196R000300020002-8

Declassified and Approved For Release 2013/02/06 : CIA-RDP10-02196R000300020002-8

TABLE 7. Some Results of the Calculation of the MASURCA Reactor*

No. of points	B^2, cm^{-2}	ANALIT			Method of finite central differences			Check data	
		k_{eff}	R_z, cm	t	k_{eff}	R_z cm	t	k_{eff}	R_z, cm
30	0,00000	0,9992	13,4601	6 min 43 sec	0,99995	13,3359	8 min 07 sec	0,99999	13,5040
50			33,6799			33,5556			33,7238
80			64,1596			64,0354			64,2035
30	0,00245	1,0.0029	27,1530	6 min 42 sec	1,00009	28,0802	8 min 07 sec	1,00002	27,2030
50			47,3728			48,2999			47,4028
80			77,8525			78,7796			77,9025

*R_z is the critical radius of the zone; t is the calculation time.

initial data and $\bar{\nu} = 2.8$. The flux Φ^k is found for this spectrum, and a new value of $\bar{\nu}$ is determined by formula (6), etc. The fission spectrum for ν is found by linear interpolation of the tabulated values corresponding to the values assigned as the starting data for $\bar{\nu}$.

The output data of the PRIDAN program can be formulated in the form of input data for different programs for the neutron-physics calculation of fast reactors: MED, FAST, ANALIT, etc. These programs, like PRIDAN, are written in FORTRAN IV language.

A standard fast reactor [7, 8] was investigated, which is a simplified spherical model of a fast power reactor with sodium coolant and oxide fuel. The volume of the core is 2.5 m^3. The isotopic composition of the reactor, geometrical dimensions, and number of points of the spatial network of the calculations are given in Table 1, and the fuel composition for versions A, B, and C are given in Table 2. In addition to the BNDL constants [5], the same library was used in the calculations, but with the recalculated data for ^{239}Pu and ^{238}U (BNDL-M) [8].

The effective neutron multiplication coefficients k_{eff} and the integrated neutron flux over the zones were calculated by the MED program [9]. The maximum number of energy groups in the program was 26, the maximum number of spatial points was 170, and they were distributed in seven zones.

The critical masses for the plutonium isotopes, contribution to the reactivity of ^{240}Pu and ^{241}Pu, normalized integrated spectra, reaction velocities, neutron balance, and plutonium breeding characteristics were calculated by the FAST program [10].

It can be seen from the data of Table 3 that the values of k_{eff} calculated using the BNDL constants are markedly higher than those obtained by means of the BNDL-M constants. The results of the calculation of the neutron balance, using the BNDL-M constants, are given in Table 4 for P, F, and C — the production, fission, and capture reaction velocities, respectively. In order to estimate the effect of sodium losses on the reactivity, k_{eff} was calculated for version A with a reduction of the amount of sodium in the core and shield by a factor of 2. As a result, $\Delta k/k = -0.43\%$.

The calculated critical masses of ^{239}Pu for versions A, B, and C amount to 991.4, 1051.9, and 1002.3 kg, respectively. The parameters defining the plutonium breeding — the excess breeding coefficient C_j for the zone j, the physical breeding coefficient B_j, and breeding factors BF — are given in Table 6. In order to study the effect of the neutron fission spectrum on k_{eff}, the spectrum corresponding to $\bar{\nu} = 2.9$ for the core and $\bar{\nu} = 2.88$ for the shield was replaced by the spectrum corresponding to $\bar{\nu} = 2.4$. For all versions and systems of constants BNDL and BNDL-M, k_{eff} was reduced by almost 0.4%. In order to estimate the effect of the multigroup constants, version C was also calculated using the UKNDF constants [11] for ^{240}Pu. Although the principal results of the calculations proved to be quite close (critical mass of ^{239}Pu = 947.7 kg, BF = 1.35; according to BNDL: 1002.3 kg, 1.37, respectively), it was was advantageous to correct the BNDL data for ^{240}Pu.

The calculations for version B were performed with different fission product capture cross sections (Table 6): with cross sections from BNDL (B-1), with cross sections from RCN [12] system of constants (B-2), and with cross sections obtained from BNDL with the addition of the long-lived fission product cross sections for ^{113}Cd, ^{149}Sm, ^{151}Sm, ^{155}Gd, ^{157}Gd (B-3). From a comparison of the versions B-1 and B-3 it can be seen that the capture and fission product cross sections for energies below 160 eV have no significant effect on the neutron parameters of the reactor. This is explained by the fact that there are almost no neutrons in this energy range [3].

Declassified and Approved For Release 2013/02/06 : CIA-RDP10-02196R000300020002-8

Declassified and Approved For Release 2013/02/06 : CIA-RDP10-02196R000300020002-8

The results of the calculations of version A showed that k_{eff} increases by 2.0 and 2.9%, with increase of the temperature of the medium from 300 to 2100°K, when using the BNDL-M and BNDL systems of constants, respectively.

Calculations using the procedure of [13] for the LADY GODIVA fast reactor, performed for two zones in four-group diffusion approximation, showed the excellent agreement between the experimental and calculated data for k_{eff} and the critical radius of the reactor.

The use of different finite-difference methods [14] for the solution of multigroup diffusion equations is accompanied by the appearance of errors, due to the approximation of the analytical differntial operators by finite differences. With specified conditions, the multigroup diffusion equation can be solved analytically by means of a relatively uncomplicated method [13], which is also suitable for practical application. Based on this method, the ANALIT program has been developed for the calculation of criticality in plane geometry. Calculations of the French fast reactor MASURCA were performed by this procedure. The results of calculations by the ANALIT program are compared in Table 7 with the results obtained with the program developed on the basis of the finite-central-differences program, for which the errors are shown to be minimal.

LITERATURE CITED

1. I. D. Iordanov, Yad. Energ., 15, No. 8 (1981).
2. R. Kidman et al., Nucl. Sci. Eng., 48, 189 (1972).
3. I. D. Iordanov and N. A. Antonov, Yad. Energ., 18 (1982).*
4. I. D. Iordanov and N. A. Antonov, Yad. Energ., 18 (1982).*
5. L. P. Abagyan et al., Group Constants for the Calculation of Nuclear Reactors [in Russian], Atomizdat, Moscow (1964).
6. G. Cecchini, M. Cosimi, and M. Salvatores, The Pravda Code for the Generalization of Effective Capture Cross Sections [in Italian], RT/FI (72) 48, CNEN-Rome.
7. A. Baker and A. Hammond, Calculations for a Large Fast Reactor, A Comparision of Results Organized by the IWG on Fast Reactors of the IAEA. TRG Report 2133 (R) (1971).
8. L. P. Abagyan et al., Calculations of the Characteristics of a "Standard" Fast Reactor, Preprint FEI-525, Obninsk (1974).
9. I. D. Iordanov, Yad. Energ., 6, No. 5 (1978).
10. I. D. Iordanov and N. A. Antonov, Yad. Energ., 18 (1982).*
11. E. Menapace, M. Motta, and G. Panini, A 26-Group Library and Self-Shielding Factors for Fast Reactor Calculations from the UK Nuclear Data File. RT/FI (73)15, CNEN-Rome.
12. H. Gruppelar, RCN-1 Pseudo Fission Product Capture Group Cross Section. RCN-205 (1974).
13. I. D. Iordanov and N. A. Antonov, Yad. Energ., 18 (1982).*
14. I. D. Iordanov, "Analytical solution of the multigroup diffusion equation," Doctoral Thesis, Bucharest (1975).

*As in the Russian original — Publisher.

Declassified and Approved For Release 2013/02/06 : CIA-RDP10-02196R000300020002-8

Declassified and Approved For Release 2013/02/06 : CIA-RDP10-02196R000300020002-8

A UNIVERSAL NEUTRON IRRADIATOR WITH A ^{252}Cf SOURCE

M. A. Bak*, A. S. Krivokhat-skii,
V. A. Nikolaev, B. D. Stsiborskii,
and B. M. Shiryaev

UDC 543.53

The widespread use of the method of activation analysis using neutrons of various energies requires sources with different neutron energy spectra. A more efficient and convenient method is the use of a single irradiator whose average energy and shape of energy spectrum in the region of irradiation of the specimens can be changed fairly rapidly and simply.

In order to obtain such a source of neutrons, we have developed and constructed a laboratory irradiator with a ^{252}Cf source.

The energy spectrum of the neutrons in the irradiation cavity is shaped by choosing the necessary combination of hydrogenous moderator around the ampoules with californium and the irradiated specimen and regulating the distance between them.

Figure 1 shows the construction of the irradiator. It consists of three coaxially arranged right circular cylinders. The inner cylinder and the spaces between the cylinders can be filled with a neutron moderator, and we chose water for this purpose. The moderating properties of water are slightly less favorable than those of materials such as polyethylene, but water has a number of advantages for this type of construction: accessibility, simple introduction into the irradiator cavity and removal from it, and the possibility of shifting the sources in it. Six metal ampoules with ^{252}Cf are placed on special holders in the inner cylinder. The total mass of the californium may be as much as 100 μg. The purpose of distributing it into six ampoules is to produce a more uniform neutron field at the center of the irradiator; in addition, it is more convenient to handle lower-intensity sources when they are being transported and loaded into the irradiator. The placement of the ampoules into the irradiator and their removal from it can be accomplished without dismantling it. The limiting amount of californium used is determined by the conditions of radiation safety of the service personnel; the radiation shielding for them consists of the outer layer of moderator in the irradiator, which weakens the neutron flux, and the layer of lead, which weakens the γ radiation. When low-power neutron sources are used, the lead layer between the inner and outer cylinders may be removed, and the space thus left may be filled with moderator or left empty. This reduces the mass of the apparatus. The ampoules containing the californium can be brought closer to the center or moved away from it symmetrically within the limits of the inner cylinder. They can be moved into a rigorously fixed calibrated position by using a mechanical control to rotate the axial tube, which bears a rotation indicator. At the center of the inner cylinder, at the lower end of the axial tube, there is a polyethylene chamber for the material being irradiated. The axial tube, together with the chamber, can easily be inserted into the irradiator and removed from it. The dimensions of the central region of the moderator are chosen with due regard for the requirement that the radius of the inner cylinder must be larger than the slowing-down length of the source neutrons (in our case this is 5-6 cm) and the diffusion length of the thermal neutrons (of the order of 3 cm). Under these conditions, leakage of neutrons from the moderator should not lead to any substantial attenuation of the neutron flux at the center of the irradiator. On the basis of this, the diameter of the inner cylinder was chosen to be 30 cm. The total diameter and height of the irradiator may be as much as 1 m. In order to reduce its mass, the shape of the external tank may be made nearly spherical.

The irradiator was tested with ^{235}U and ^{238}U targets. The fissions were recorded with solid-state detectors. We measured the fissionability of the ^{235}U and ^{238}U (as the fissionability characteristic we took the number of fissions taking place in specimens of fission-

*Deceased.

Translated from Atomnaya Énergiya, Vol. 54, No. 2, pp. 132-133, February, 1983. Original article submitted February 8, 1982.

 0038-531X/83/5402-0152$07.50 © 1983 Plenum Publishing Corporation

Declassified and Approved For Release 2013/02/06 : CIA-RDP10-02196R000300020002-8

Declassified and Approved For Release 2013/02/06 : CIA-RDP10-02196R000300020002-8

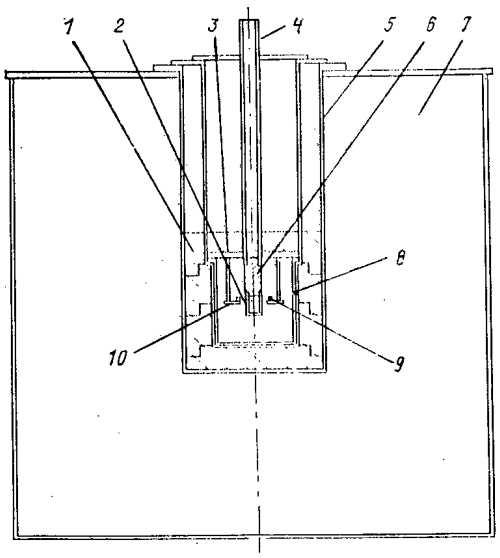

Fig. 1. Schematic diagram of the construction of the irradiator: 1) lead shielding; 2) chamber for the specimen being irradiated; 3) cover of the inner tank in which the mechanism for moving the sources is placed; 4) central rotatable tube; 5) middle tank; 6) polyethylene packing; 7) outer layer of moderator; 8) inner tank; 9) isotope sources; 10) isotope-source holders.

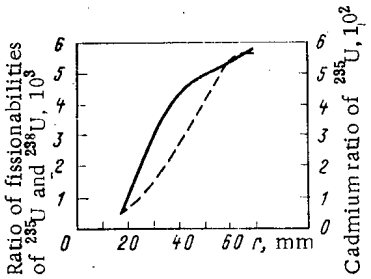

Fig. 2. Cadmium ratio for ^{235}U (– – –) and ratio of the fissionabilities of ^{235}U and ^{238}U (———) as functions of the distance r between the center of the chamber and the neutron sources.

able material with unit mass per unit of time), the cadmium ratio for the ^{235}U (the ratio of the fissionability of the ^{235}U without shielding of the target with a cadmium layer to its fissionability when the cadmium was used), and the fissionability of the ^{235}U and ^{238}U by fast neutrons when the moderator was removed, so that the lead cavity was left empty, and the neutron sources were inserted until they touched the chamber. Figure 2 shows the results of some of the measurements. To estimate the possibilities of using the irradiator in neutron activation analysis, we may use the measured fissionability of the ^{235}U. When neutron sources with a total of 100 μg of ^{252}Cf (neutron flux of $3 \cdot 10^8$ sec^{-1}) are placed at an optimal distance of r = 2.5 cm from the center of the chamber and all the cavities of the irradiator are filled with water, the fissionability of the ^{235}U is $1.7 \cdot 10^5$ $mg^{-1} \cdot min^{-1}$.

The ratio of the fissionability of the ^{235}U and ^{238}U increases with increasing r, from 450 (for r = 17.5 mm) to 6000 (for r = 75 mm) when all the cavities are filled with water. When the water is removed from the inner cavities of the irradiator, this ratio decreases to about 5. When the water was removed from the central and intermediate cylinders, the fissionability of the ^{238}U and the cadmium ratio for it varied according to a law close to $1/r^2$, which indicated that the flux of fast neutrons does not play a significant role after it is scattered by the various structural components. The fissionability of ^{235}U shielded with cadmium was found to be lower under these conditions than in the case when the space was filled with water; this was evidence of the considerably larger contribution of ^{235}U

Declassified and Approved For Release 2013/02/06 : CIA-RDP10-02196R000300020002-8

Declassified and Approved For Release 2013/02/06 : CIA-RDP10-02196R000300020002-8

fissions caused by supercadmium neutrons when the space was filled with water. If the space between the inner and intermediate cylinders was not filled with water, the flux of slowed-down neutrons for large values of r was about 10% less than with a water filling, while the flux of supercadmium neutrons remained unchanged.

The measurements showed that an irradiator constructed on the basis of an isotopic neutron source makes it possible to form neutron fields in which the effective neutron energy may vary considerably. Such an irradiator can be used not only as a stationary device, but also as a transportable apparatus for activation analysis using neutrons of various effective energies. The total mass of the irradiator is about 1 ton.

EFFECTS OF HYDROGEN-ION BOMBARDMENT ON THE STRUCTURE AND COMPOSITION OF A NICKEL-RICH ALLOY

M. I. Guseva, A. N. Mansurova,
O. S. Naftulin, Yu. V. Nikol'skii,
P. A. Fefelov, and O. I. Chelnokov

UDC 539.12.04:621.039.616

We have examined the effects of hydrogen-ion bombardment on the structure and chemical composition of a nickel-rich alloy (18-20% Cr, 53-56% Ni) containing molybdenum and tungsten. The alloying elements make this alloy considerably superior in properties to an austenitic stainless steel of type Kh16N15 and Kh18N10, and in particular it has much higher long-term strength and plasticity.

Targets were bomarded at 750°C by scanning a monoenergetic beam of hydrogen ions of energy 10 keV over the surface, the intensity being 6×10^{15} ions·cm^{-2}·sec^{-1} at the dose range from 10^{19} to 5×10^{20} ions·cm^{-2}, these values corresponding to the working lives of certain proposed large fusion systems. The experiments were performed with the ILU ion-beam accelerator [1].

Auger spectroscopy was used to examine the effects of hydrogen-ion bombardment on the chemical composition of the surface. Serial etching with argon ions of energy 2 keV was used to determine the depth distributions of the major components.

The surface topography was examined in a scanning electron microscope for various doses of these hydrogen ions of energy 10 keV, and it was found that there were pores of size about 100-200 nm, as well as sharp grain boundaries appearing as a result of the ion etching. The pores occurred within the bodies of the grains and at the grain boundaries. The pore density in the grain bodies increased with the dose and at 5×10^{20} ions·cm^{-2} was about 10^9 cm^{-2}. Fusion of the pores at the grain boundaries produced continuous cracks, and at a dose of 10^{19} ions·cm^{-2} the cracks occurred only in individual parts, whereas at 5×10^{20} ions·cm^{-2} the cracking at the grain boundaries occurred virtually throughout the irradiated surface.

It has previously been observed [2] that a porous surface is produced by implantation of high doses of helium ions in nickel-rich alloys, and the same has been observed for high-temperature helium blistering at $T_{irr} > 0.5 - 0.6T_{mp}$ [3]. Das and Kaminsky [4] irradiated polycrystalline Nb with D ions (energy 250 keV) to a dose of 1.25×10^{19} ions·cm^{-2} at 700°C and found that blisters were formed at the surface. In the case of a nickel-rich alloy exposed to H^+, the effects were as in the bombardment with He^+ at high temperatures, in that a spongy structure was produced by diffusion of the implanted ions and defects, which led to diffuseness in the distribution curves, and also to virtually identical stresses throughout the thickness of the implanted layer from the surface. In that case the gas bubbles were also uniformly distributed over the thickness of the layer and linked up at high doses to form channels emerging from the surface, along which the gas was released from the target. One assumes that this extensive branched porous surface will favor reduced tritium loss from the volume.

Translated from Atomnaya Énergiya, Vol. 54, No. 2, pp. 134-135, February, 1983. Original article submitted April 9, 1982.

 0038-531X/83/5402-0154$07.50 © 1983 Plenum Publishing Corporation

Declassified and Approved For Release 2013/02/06 : CIA-RDP10-02196R000300020002-8

Declassified and Approved For Release 2013/02/06 : CIA-RDP10-02196R000300020002-8

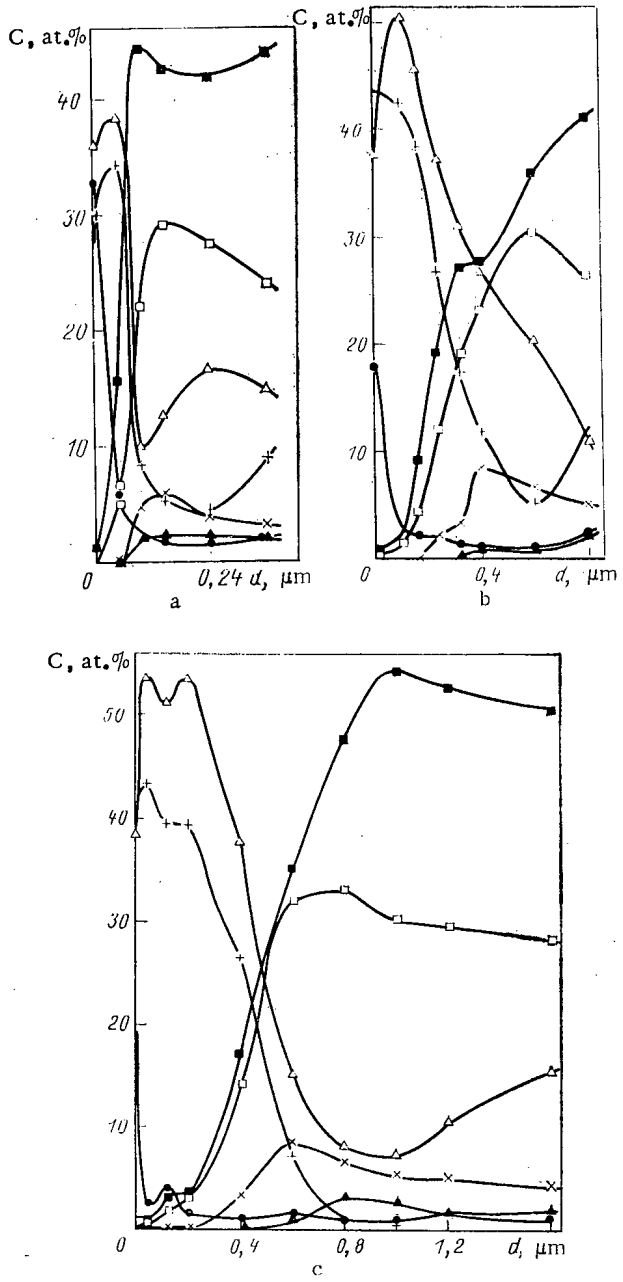

Fig. 1. Distributions of the major components in a nickel-rich alloy after irradiation by hydrogen ions of energy 10 keV (T_{irr} = 750°C) at doses of 10^{19} (a), $5 \cdot 10^{19}$ (b), and 10^{20} ions·cm^{-2} (c); △ — Cr; □ — Fe; ■ — Ni; × — Mo; ▲ — W; +) O; ● — C.

Figure 1 shows distribution curves for the major components and the alloying ones after various hydrogen-ion doses at 750°C obtained by Auger spectroscopy with sequential etching. The bombardment increases the chronium concentration in the surface by a factor of 2-3 as the dose increases from 10^{19} to 10^{20} ions·cm^{-2}, while the thickness of this chromium-enriched layer increases by a factor of about five. At the same time, there is a reduction in the chromium content in the deeper parts of the specimen, and the thickness of this depleted region increases with the dose. This is characteristic of radiation-induced segregation associated with nonequilibrium impurity vacancies [5, 6]. The complexes between vacancies and impurity atoms move to the surface, where one gets a nonequilibrium but reasonably stable segregation of the impurity atoms after vacancy annihilation [6]. The surface contains a considerable amount of oxygen on account of the oxidation of the chromium.

Declassified and Approved For Release 2013/02/06 : CIA-RDP10-02196R000300020002-8

Declassified and Approved For Release 2013/02/06 : CIA-RDP10-02196R000300020002-8

Figure 1 shows that the surface layer lacks tungsten and molybdenum atoms, and the thickness of this depleted layer increases with the dose. The irradiation times at 750°C varied from about 1.5 to 15 h. The lack of W and Mo in the surface layer cannot be explained as due to sputtering by ion bombardment, because Fe and Ni sputter preferentially, i.e., they are components having higher sputtering coefficients [7]. Also, on increasing the dose from 10^{19} to 5×10^{19} or 10^{20} ions·cm^{-2} (Fig. 1), the thickness of the sputtered layer is substantially less than the observed displacement of the distribution curves for W and Mo.

This surface depletion for large impurity atoms whose concentrations do not exceed the solubility limit is in agreement with concepts on radiation-induced impurity segregation in fcc metals [8, 9] as derived from the Okamoto–Widersich model [10]. On this model, large atoms in substitution positions diffuse in the opposite sense to the radiation vacancies and leave the surface zone.

Therefore, the redistribution of the major components and alloying elements produced by ion bombardment in this nickel-rich alloy is favorable as regards preventing the plasma from contamination by heavy elements such as tungsten and molybdenum, whose permissible concentrations in a deuterium–tritium plasma are 0.1 and 1%, correspondingly [11]. The W and Mo have a favorable effect on the heat resistance of the nickel-rich alloy, which opens up prospects for using it as a material of the first wall in a fusion reactor instead of expensive molybdenum alloys.

LITERATURE CITED

1. V. M. Gusev, N. P. Busharov, and S. M. Naftulin, Prib. Tekh. Eksp., 64, 19 (1969).
2. V. M. Gusev et al., Rad. Effects, 40, 37 (1979).
3. V. M. Gusev et al., Preprint IAE-3133, Moscow (1979).
4. S. Das and M. Kaminsky, "Radiation blistering in metals and alloys," in: Rad. Effects on Solid Surf., Washington (1976), p. 119.
5. V. F. Zelenskii et al., Nuclear Science and Engineering: Series Radiation-Damage Physics and Radiation Materials Sciences [in Russian], Issue 3 (14), Moscow (1980), p. 48.
6. R. Hanneman and T. Anthony, Acta Metalurgica, 17, No. 9, 1133 (1969).
7. G. Wehner, in: Proc. 2 Coll. Int. de Pulver. Cathodique, Nice (1976), p. 1.
8. L. Rehn et al., J. Nucl. Mater., 74, 242 (1978).
9. R. Piller and A. Marwick, J. Nucl. Mater., 71 309 (1978).
10. P. Okamoto and H. Widersich, ibid., 53, 336 (1974).
11. N. V. Pleshivtsev, Physical Problems in Cathode Sputtering: IAE Survey [in Russian], Moscow (1979), p. 23.

Declassified and Approved For Release 2013/02/06 : CIA-RDP10-02196R000300020002-8

Declassified and Approved For Release 2013/02/06 : CIA-RDP10-02196R000300020002-8

REMOVAL OF MONO-2-ETHYLHEXYLPHOSPHORIC ACID FROM SOLID EXTRACTION AGENTS WITH DI-2-ETHYLHEXYLPHOSPHORIC ACID

V. B. Dedov, P. S. Trukhlyaev,
B. S. Kalinichenko, and I. K. Shvetsov

UDC 543.544.4

When solid extraction agents are used with di-2-ethylhexylphosphoric acid (D2EHPA), the organic phase accumulates the destruction product from the extractant: mono-2-ethylhexylphosphoric acid (M2EHPA), which has higher extraction performance and thus hinders the solvent-extraction and chromatographic separation of the transplutonium, rare-earth, and other elements (V. S. Smelov et al., Atomnaya Énergiya, 51, No. 4, 231 (1981)).

One can remove the M2EHPA from the solid extraction agent containing D2EHPA to regenerate it by washing the column with distilled water. Figure 1 shows that the content of the M2EHPA and also that of the D2EHPA in the matrix decreases when the matrix is chloromethylated styrene and distilled water is passed through the column. Clearly, washing with 100 column volumes of water can reduce the M2EHPA content in the extraction agent to 0.6% from an initial concentration of 6%, and at that level the effects of the component will be inappreciable, while the loss of D2EHPA will not exceed 10-12%. To remove the M2EHPA from a solid extraction agent prepared on a polysorb matrix it is sufficient to wash with 10 column volumes of water.

The elution of the extraction agent from the matrix no matter what the method of production indicates that the bond between these two components is not strong. This has been established qualitatively for all solid extraction agents.

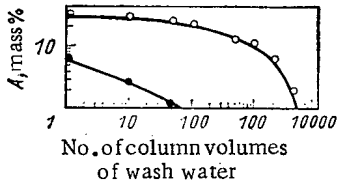

Fig. 1. Dependence of the content A of a component in the solid extraction agent on washing with water: ○ – D2EHPA: ● – M2EHPA.

Translated from Atomnaya Énergiya, Vol. 54, No. 2, p. 135, February, 1983. Original article submitted June 14, 1982.

0038-531X/83/5402-0157$07.50 © 1983 Plenum Publishing Corporation

Declassified and Approved For Release 2013/02/06 : CIA-RDP10-02196R000300020002-8

Declassified and Approved For Release 2013/02/06 : CIA-RDP10-02196R000300020002-8

NEUTRON ACTIVITY OF THE EARTH AND THE Cl—Ar NEUTRINO EXPERIMENT

I. R. Barabanov, V. N. Gavrin,
G. T. Zatsepin, I. V. Orekhov,
and L. P. Prokop'eva

UDC 539.12.164

In connection with radiochemical experiments for the detection of solar neutrinos which have already been conducted [1] as well as those being planned [2], the urgency of the experimental investigation of the flux of fast neutrons from rocks has increased. Incident on a detector, fast neutrons give by means of the two-stage reaction (n, p), (p, n) the very same isotope as do neutrinos as the result of the reaction $(Z, N) + \nu \rightarrow (Z + 1, N - 1) + e^-$.

The results obtained in more than 10 years with a chlorine—argon detector of solar neutrinos at the Brookhaven National Laboratory of the USA have shown that the flux of solar neutrinos is at least 3-4 times less than the expected value, and the questions of background effects require attentive study. The results of an investigation of the flux of fast neutrons from the ground are supplied in this article, and their possible background contribution to the neutrino experiment is discussed.

Approximate estimates show [3] that the flux density of fast neutrons from rocks with the usual uranium and thorium content should be $\sim$1 neutron/(cm^2·day) but can vary greatly depending upon the content of light elements (Li, Be, B) and water in a rock. The main source of neutrons are (α, n) reactions with the elements C, N, O, Mg, Al, and Si under the action of α particles of the uranium and thorium series. Fast neutrons arising as a result of the spontaneous fission of ^{238}U still make approximatley a 10% contribution.

The isolation and measurement of such a small flux density of fast neutrons as 1.5 neutron/(cm^2·day) is scarcely possible with the help of the usual neutron detectors (scintillators, helium (^{3}He) counters, etc. [4]) against an emission background greater by a factor of 10^6. Therefore, the radiochemical method using the reaction ^{40}Ca(n, α)^{37}Ar was selected for measurement of the flux of fast neutrons from rocks. This reaction is convenient in that its cross section [5] increases sharply at E = 3 MeV and is actually of a threshold nature. The technique for the extraction of the small amount of ^{37}Ar formed (right down to tens of atoms) and the measurement of its activity has been well developed. People usually use an aqueous solution of some calcium salt or other in detectors of this kind, and they extract the ^{37}Ar formed by blowing a gas through the liquid, e.g., helium. However, water is a good moderator of fast neutrons, which leads to a decrease in the sensitivity of such detectors. Taking account, moreover, of the fact that the detector must contain $\sim$100 kg of Ca to achieve the required sensitivity, it would be difficult to work with such a detector under subterranean conditions. Therefore, a different way was selected to create the detector.

It has been shown previously [6] that the ^{37}Ar formed as the result of neutron irradiation can be extracted with practically 100% efficiency from some solid compounds of calcium organic compounds, e.g., from CaC_2O_4 (calcium oxalate), by a trap with activated carbon at a temperature of —196°C.

A radiochemical detector of fast neutrons [7] was created on the basis of this result. The detector consists of a hermetically sealed cylinder 60 cm in diameter and 120 cm in height filled with CaC_2O_4 dried in advance, containing 60 kg of Ca. A valve is mounted on the top end of the cylinder to evacuate the detector and extract the ^{37}Ar formed. A manometer tube is mounted in the lower part of the cylinder to control the pressure.

After exposure of the detector in the neutron flux being measured, a trap with activated carbon ($\sim$1 g) at a temperature of —196°C, in which the ^{37}Ar formed is adsorbed, is connected to the upper valve. Subsequent purification of the ^{37}Ar and measurement of its activity are described in [8]. Calibration measurements with neutrons from a Pu—Be source have shown that the process of extracting ^{37}Ar from the detector is subject to the law $Q = Q_0[1 - \exp(-t/t_0)]$, where t_0 = 1.42 h. Thus, 95% of the ^{37}Ar is extracted in 4 h.

Translated from Atomnaya Énergiya, Vol. 54, No. 2, pp. 136-137, February, 1983. Original article submitted June 16, 1982.

 0038-531X/83/5402-0158$07.50 © 1983 Plenum Publishing Corporation

Declassified and Approved For Release 2013/02/06 : CIA-RDP10-02196R000300020002-8

Declassified and Approved For Release 2013/02/06 : CIA-RDP10-02196R000300020002-8

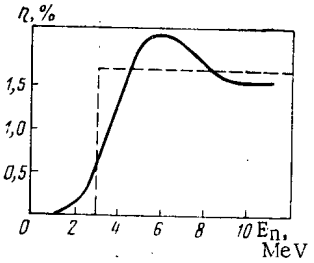

Fig. 1

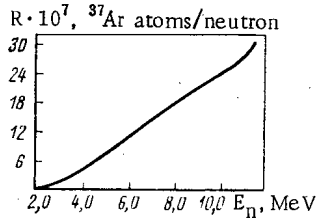

Fig. 2

Fig. 1. Dependence of the efficiency of the calcium detector on the neutron energy (a monoenergetic isotropic source distributed uniformly over the detector surface).

Fig. 2. Dependence of the ^{37}Ar yield per neutron R on neutron energy in the detector of R. Davis.

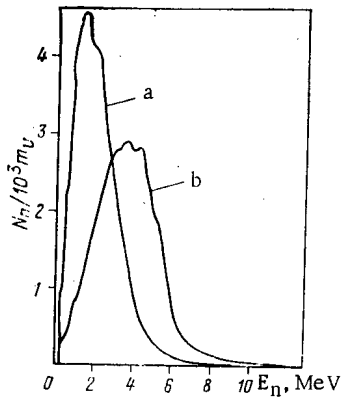

Fig. 3. Cumulative energy spectrum of neutrons in granite from (α, n) reactions and spontaneous fission of uranium; a, b) contributions of the (α, n) reactions are obtained with assumptions 1 and 2, respectively. The spectra were calculated for the concentration ratio ($m_{Th} : m_U = 5 : 1$).

The dependence of the detector efficiency on the neutron energy has been calculated by the Monte Carlo method. The computational results are presented in Fig. 1. The sensitivity of the detector created to the flux density of fast neutrons is $\sim 3 \times 10^{-3}$ neutrons/(cm^2·day) [7] and is sufficient, with a large reserve, for measurement of neutrons from terrestrial soil. Measurements have been made with the help of this detector in subterranean rooms of the Baksansk Neutrino Observatory [9] at a depth of ~1000 m below sea level. The average rate of formation of ^{37}Ar in the equipment turned out to be (0.89 ± 0.09) ^{37}Ar atoms/h. If one approximates the detector efficiency as shown in Fig. 1 by the value 1.7% for $E \geq 3$ MeV and 0% for $E < 3$ MeV, then we obtain $N = 0.045$ day^{-1}·cm^{-2} for the flux of neutrons with $E \geq 3$ MeV.

The data obtained were used to estimate the background of a radiochemical detector of solar neutrinos from the neutrons of rocks. The Brookhaven chlorine detector is a tank 10 m long and 6 m in diameter filled with 610 tons of C_2Cl_4 (perchloroethylene). The reaction recorded is $^{37}Cl(\nu, e^-)^{37}Ar$. The background under the action of fast neutrons arises mainly as a result of the chain of reactions $^{35}Cl(n, p)^{35}S$ and $^{35}Cl(p, n)^{37}Ar$. The efficiency of formation of ^{37}Ar in this detector by neutrons of different energies was calculated by the Monte Carlo method. The elastic and inelastic cross sections of neutrons as well as the nuclear reactions by all the nuclei making up the detector were taken into account in the calculation. All necessary neutron cross sections were taken from [5].

Declassified and Approved For Release 2013/02/06 : CIA-RDP10-02196R000300020002-8

Declassified and Approved For Release 2013/02/06 : CIA-RDP10-02196R000300020002-8

The spectrum of the protons generated as a result of the (n, p) reaction were calculated from the statistical model developed in [10]. According to this model, the spectrum of the protons emitted from a compound nucleus is described by the Weiskopf formula

$$P(E)=\frac{gm}{\pi^2\hbar^3}\sigma E\,[W(f)/W(i)]; \tag{1}$$

as recommended in [10], the empirical dependence

$$\sigma=\sigma_q(1+C)(1-KV/E) \tag{2}$$

is taken as the cross section σ of the inverse reaction, where σ_q is the geometric cross section, C and K are constants dependent on the charge of the nucleus, and V is the coulomb barrier. For the nuclei of interest to us C = 0.368 and K = 0.516 in accordance with [10]. The yield of ^{37}Ar per proton (I, nucleus/proton) was calculated from the formula

$$I=n_0\int_{E_{\text{thr}}}^{E_{\max}}W(E)\int_{E_{\text{thr}}}^{E}\frac{\sigma_{pn}(\varepsilon)}{|d\varepsilon/dx|}\,d\varepsilon\,dE, \tag{3}$$

where W(E) is the proton spectrum and $\sigma_{pn}(E)$ is the perturbation function of the (p, n) reaction with ^{37}Cl (taken from [11]). The criterion for the correctness of the calculation was a comparison of the calculated ^{37}Ar yield under the action of neutrons with the spectrum of a Ra—Be source with the experimentally obtained yield upon irradiation of the detector by the Ra—Be source. The experimentally obtained value is equal to $(7.5 \pm 0.4) \times 10^{-7}$ ^{37}Ar atoms/neutron, and the calculated value was 5.2×10^{-7} ^{37}Ar atoms/neutron. Taking account of the indeterminacy of the neutron constants and the error of the experimental value, such agreement should be considered to be rather good. But one can achieve absolute agreement by selecting the constant K in formula (2). With K = 0.634 ± 0.03 agreement is obtained between the calculated and experimental yields. The value K = 0.634 was used in the subsequent calculations.

The calculated dependence of the ^{37}Ar yield on neutron energy is presented in Fig. 2. It is evident from a comparision of Figs. 1 and 2 that the dependence of the effective formation of ^{37}Ar in perchloroethylene and CaC_2O_4 under the action of neutrons is different, generally speaking, and it is necesary to use data on the spectrum of neutrons from the ground based on the data of the calcium detector to calculate the background from fast neutrons in the chlorine detector.

Neutron generation spectra in granite were calculated in [12] with two assumptions regarding the energy carried off by the neutron from a compound nucleus:

1. The emitted neutrons have a Maxwellian energy distribution in the center-of-mass system.

2. The neutrons carry off energy in the center-of-mass system equal to the energy of the output channel.

The first case is evidently similar to the actual one, whereas the second case gives an extremely "hard" spectrum. The spectra in Fig. 3 were normalized to the results obtained with the calcium detector; the integral of the product of the spectrum normalized by the efficiency of formation of ^{37}Ar in the chlorine detector (see Fig. 2) gives the desired background of the chlorine detector under the action of fast neutrons. The results of the integration for spectra *a* and b, respectively, are equal to 0.079 and 0.098 ^{37}Ar atoms/day.

Thus, the amount of background in the chlorine experiment depends weakly on the assumption about the fast neutron spectrum. Even with extreme assumptions about the spectrum, the results differ by only 20%. One should compare the values obtained to the rate of ^{37}Ar formation under the action of neutrinos obtained by R. Davis (0.40 ^{37}Ar atoms/day), i.e., the background from fast neutrons of granite without shielding in the detector of R. Davis should amount to 20% of the effect. According to the estimates of R. Davis, the background from fast neutrons was ∿10% prior to installation of shielding in the chamber where the detector is located.

Declassified and Approved For Release 2013/02/06 : CIA-RDP10-02196R000300020002-8

Declassified and Approved For Release 2013/02/06 : CIA-RDP10-02196R000300020002-8

LITERATURE CITED

1. R. Davis, D. Hammer, and K. Hoffman, Phys. Rev. Lett., 20, 1205 (1968).
2. G. Zatsepin, in: Proc. Int. Conf. on Neutrino Physics and Neutrino Astrophysics, Vol. 1, Baksansk Valley (1978), p. 20.
3. I. A. Arshinov, V. I. Glotov, and G. T. Zatsepin, in: Proc. Int. Conf. on Low Radioact. Meas. Appl., Bratislava (1977), p. 29.
4. G. V. Gorshkov, V. A. Zyabkin, and R. N. Yakovlev, Yad. Fiz., 13, No. 4, 791 (1971).
5. D. Gullen et al., The LLL Evaluation Nuclear Data Library (ENDL), UCRL-50400 (1976), p. 15.
6. I. R. Barabanov et al., Izv. Akad. Nauk SSSR, Ser. Fiz., 40, 1050 (1976).
7. I. R. Barabanov et al., At. Energ., 47, No. 4, 273 (1979).
8. I. R. Barabanov et al., At. Energ., 37, No. 6, 503 (1974).
9. I. R. Barabanov et al., At. Energ., 50, No. 1, 59 (1981).
10. I. Dostrovsky et al., Phys. Rev., 116, No. 3, 683 (1959).
11. R. Kishore et al., ibid., 12 , No. 1, 21 (1975).
12. V. I. Glotov, Kr. Soobshch. Fiz., No. 7, 75 (1970).

ION SYNCHROTRON COMPLEX OF V. G. KHLOPIN RADIUM INSTITUTE

N. A. Perfilov, V. P. Shilov,
V. P. Eismont, V. L. Auslender,
V. N. Lazarev, and B. L. Faktorovich

UDC 621.384.634

Existing accelerators can deliver heavy ions with an energy $E \leqslant 10$ MeV/nucleon and $E \geqslant 1$ GeV/nucleon. The range of intermediate energy values (several tens and hundreds of megaelectron volts) remains open: at the present time there are no special accelerators capable of producing continuously variable ion beams of such energy. Moreover, this range is now of extreme interest, since hopes for research into the most fundamental properties of nuclear matter and product nuclei are linked with it: the form of the equation of states (including the problem of "superdense" isomers), the existence of a critical nuclear temperature, maximum rotational moments, the nature and magnitude of nuclear "friction," etc. At an energy of several tens of megaelectron volts per nucleon, important limits of the physics of heavy ions are reached, e.g., the sound barrier ($E \approx 15$–20 MeV/nucleon) and the Fermi energy (30–40 MeV/nucleon). It is expected that hydrodynamic effects of compression of nuclear matter begin at the first, while at the second the mechanism of nuclear collision changes significantly, i.e., there is a transition from interaction between nuclei as a whole to interaction between the nucleons constituting them.

It is not surprising, therefore, that the aim of almost all heavy-ion accelerator projects now is to attain energies of tens and hundreds of megaelectron volts per nucleon. Such projects exist in our country [1, 2] and abroad [3].

In this paper we report on an ion-synchrotron complex for an energy of 50 MeV/nucleon, under construction at the V. G. Khlopin Radium Institute in Leningrad. Besides the synchrotron, the complex includes large experimental facilities and systems for automatic control of the accelerator and research on it.

The ion synchrotron [4, 5] has been designed to produce beams of accelerated protons and completely ionized atoms ($Z/A \approx 0.5$) in the continuously variable ranges 10–200 and 0.3–50 MeV/nucleon, respectively. The energy homogeneity of the extracted beams is not less than 1% with a current-pulse duration of 20 μsec and pulse-repetition rate of 50 Hz. The intensity of the extracted proton beam is up to 10^{11} particles/sec, while that of the beam of multiply charged ions is no less than 10^{8} particles/sec. The synchrotron is a weak-focusing ring with four straight gaps and an equilibrium-orbit radius of 1.4 m. Bending–focusing magnets, an accelerating cavity, and a system for particle injection and extraction are installed inside a common vacuum-tight housing with an outer diameter of ∿4.2 m. The design average vacuum in the synchrotron orbit is no less than $6.7 \cdot 10^{-5}$ Pa ($\sim 5 \cdot 10^{-7}$ torr) [6].

Translated from Atomnaya Énergiya, Vol. 54, No. 2, pp. 137-139, Feburary, 1983. Original article submitted July 9, 1982.

0038-531X/83/5402-0161$07.50 © 1983 Plenum Publishing Corporation

Declassified and Approved For Release 2013/02/06 : CIA-RDP10-02196R000300020002-8

Declassified and Approved For Release 2013/02/06 : CIA-RDP10-02196R000300020002-8

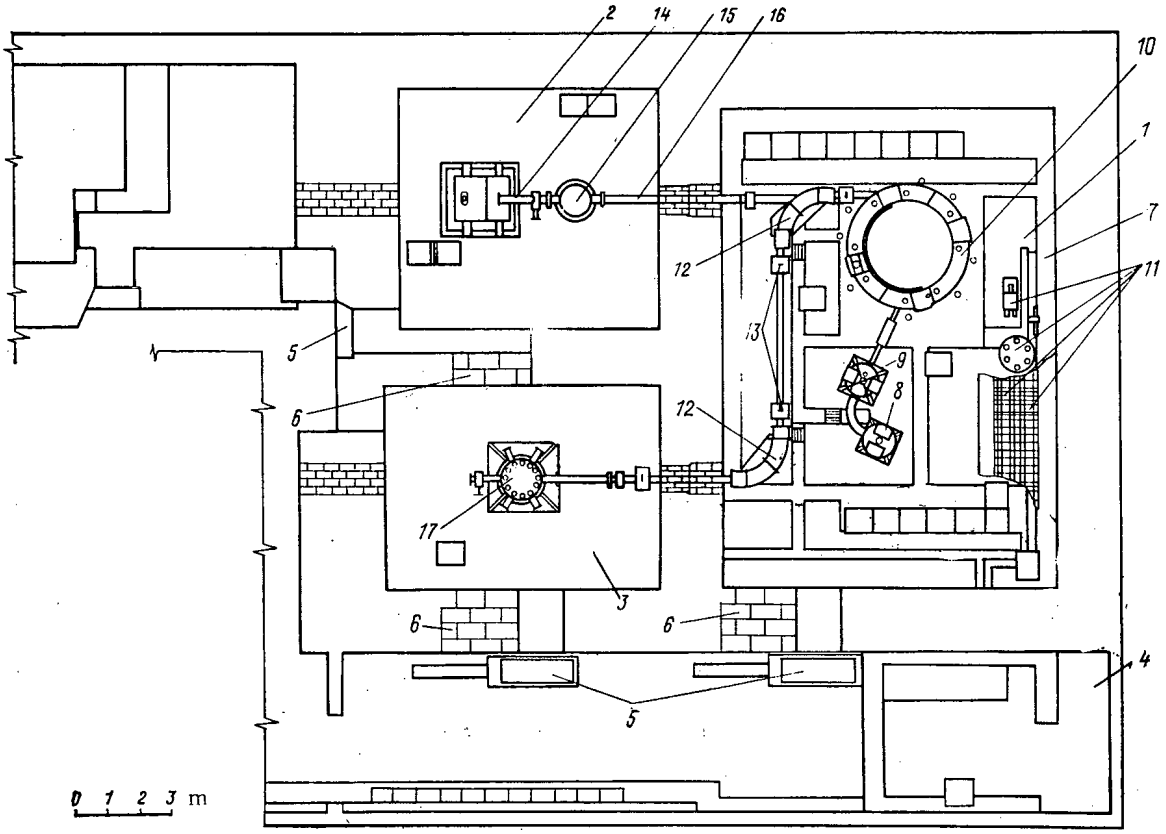

Fig. 1. Layout of accelerator and experimental facilities: 1) accelerator hall; 2) experimental hall No. 1; 3) experimental hall No. 2; 4) auxiliary premises containing the power equipment of the magnet power supply; 5) protective gates and doors; 6) walled-up openings; 7) cable channels; 8) ion source; 9) injector; 10) main ring of accelerator; 11) magnet power supply; 12) bending magnets; 13) quadrupole lenses; 14) "on-line" mass spectrometer; 15) ion source of mass spectrometer; 16) ion guide; 17) "Globus" universal nuclear-reaction chamber.

Particles are injected into the synchrotron from a pulsed rf linac [7], formed by a quarter-wave coaxial resonator shortened by the capacitance of the drift tube. The energy of protons at the exit from the resonator is 1.5 MeV, while that of ions is 0.6-1 MeV/nucleon with $Z/A \approx 0.5$.

For use of the injector in the domain of radiation research, a multibeam electron–ion accelerator was suggested [8] and designed [9] on its basis; this accelerator makes it possible to obtain, along with an ion beam, one or several electron beams whose total power at an energy of $\sim$0.6 MeV is 10-12 kW. In order to expand its capabilities, the accelerator has been supplemented with a second drift tube [10] and at the present time a version of the injector with two independent ion-acceleration channels is being built.

Protons are extracted from a source with a Penning discharge with a cathode needle in the discharge chamber [11]. The duration of the proton-current pulse is 4 μsec and the current is 90 mA at an extraction voltage of 50 kV and a pulse-repetition rate of 50 Hz.

A "warm" version [12] of an electron-beam source, suggested by E. D. Donets [13] and developed at the Institute of Nuclear Physics, Siberian Branch of the Academy of Sciences of the USSR, was used as the source of multiply charged ions. The intensity of the source of multiply charged ions is up to 10^9 nuclei/pulse for elements up to argon. The ionization cycling rate is up to 50 Hz. Just like the multibeam version of the pulsed rf linac, introducing a new quality into radiation research and technology, the heavy-ion source is also of great importance in itself. By means of two bending magnets and several quadrupole-lens doublets, the beam accelerated in the synchrotron is divided and directed into two independent experimental halls (see Fig. 1). Large experimental facilities in these halls constitute an essential part of the complex being built. It is intended to use them for a wide range of basic research on the dynamics of the interaction of complex nuclei, for the study

Declassified and Approved For Release 2013/02/06 : CIA-RDP10-02196R000300020002-8

Declassified and Approved For Release 2013/02/06 : CIA-RDP10-02196R000300020002-8

of the properties of compressed and heated nuclear matter, for the study of the decay of products formed in reactions, and for applied work on radiation physics and chemistry. The principal pieces of equipment are the "Globus" automated nuclear-reaction chamber, a high-resolution mass spectrometer, a double beta-spectrometer with a superconducting magnet of the solenoid type, and a high-vacuum chamber for studying the effect of heavy ions on matter [4].

The ion-synchrotron complex is a unique automated system whose component parts — the accelerator and the experimental facilities — are controlled and linked together by a minicomputer. Automation of the accelerator control improves the physical characteristics of the machine; eliminates unproductive losses of time, especially for resetting the accelerator regimes; and substantially improves the quality of investigations by increasing their accuracy and the volume and reliability of the data obtained. At the present time the accelerator is controlled with an M-6000 computer [14], but in the future it will be replaced with an SM-2 general-purpose computer. An automated system for scientific research on the synchrotron is being built on the basis of two SM-2 general-purpose computers.

At the present time the main systems of the ion synchrotron are undergoing comprehensive alignments at the Institute of Nuclear Physics, Siberian Branch of the Academy of Sciences of the USSR. The complex is to be put into operation in 1984.

LITERATURE CITED

1. A. M. Baldin et al., Preprint No. 9-11796, Joint Institute for Nuclear Research, Dubna (1978).
2. Yu. Ts. Oganesyan, Preprint No. R9-12843, Joint Institute for Nuclear Research, Dubna (1979).
3. J. Martin, IEEE Trans. Nucl. Sci., NS-26, No. 3, 3645 (1979).
4. V. L. Auslender et al., Preprint No. RI-56, Radium Institute, Leningrad (1976).
5. V. G. Abdul'manov, in: Proceedings Tenth Int. Conf. on High-Energy Charged-Particle Accelerators [in Russian], Vol. 1, July, 1977, Serpukhov (1977), p. 345.
6. V. L. Auslender et al., Preprint No. 79-5, Institute of Nuclear Physics, Novosibirsk (1979).
7. V. G. Abdul'manov et al., Preprint No. 78-25, Institute of Nuclear Physics, Novosibirsk (1978).
8. V. L. Auslender et al., Inventor's Certificate No. 641851, Byull. OIPOTZ, No. 3, 276 (1980).
9. V. L. Auslender et al., in: Proceedings Third All-Union Conference on the Application of Charged-Particle Accelerators in the National Economy [in Russian], Vol. 1, Leningrad (1971), p. 114.
10. V. L. Auslender et al., Inventor's Certifice No. 720838, Byull. OIPOTZ, No. 9, 305 (1980).
11. V. L. Auslender, V. N. Lazarev, and A. D. Panfilov, Prob. Tekh. Eksp., No. 4, 33 (1979).
12. V. G. Abdul'manov et al., in: Proceedings Sixth All-Union COnference on Charged-Particle Accelerators [in Russian], Dubna, October 11-13 (1978), Dubna (1979), Vol. 1, p. 98.
13. E. D. Donets, Inventor's Certificate No. 248860, Byull. OIPOTZ, No. 24 (1969).
14. V. L. Auslender et al., Preprint No. 78-89, Institute of Nuclear Research, Novosibirsk (1978).

Declassified and Approved For Release 2013/02/06 : CIA-RDP10-02196R000300020002-8

Declassified and Approved For Release 2013/02/06 : CIA-RDP10-02196R000300020002-8

RUSSIAN JOURNALS IN THE PHYSICAL AND MATHEMATICAL SCIENCES

AVAILABLE IN ENGLISH TRANSLATION

ALGEBRA AND LOGIC
Algebra i Logika
Vol. 21, 1982 (6 issues) $270

ASTROPHYSICS
Astrofizika
Vol. 18, 1982 (4 issues) $320

AUTOMATION AND REMOTE CONTROL
Avtomatika i Telemekhanika
Vol. 43, 1982 (24 issues) issues) $495

COMBUSTION, EXPLOSION, AND SHOCK WAVES
Fizika Goreniya i Vzryva
Vol. 18, 1982 (6 issues) $345

COSMIC RESEARCH
Kosmicheskie Issledovaniya
Vol. 20, 1982 (6 issues) $425

CYBERNETICS
Kibernetika
Vol. 18, 1982 (6 issues) $345

DIFFERENTIAL EQUATIONS
Differentsial'nye Uravneniya
Vol. 18, 1982 (12 issues) $395

DOKLADY BIOPHYSICS
Doklady Akademii Nauk SSSR
Vols. 262–267, 1982 (2 issues) $145

FLUID DYNAMICS
Izvestiya Akademii Nauk SSSR, Mekhanika Zhidkosti i Gaza
Vol. 17, 1982 (6 issues) $380

FUNCTIONAL ANALYSIS AND ITS APPLICATIONS
Funktsional'nyi Analiz i Ego Prilozheniya
Vol. 16, 1982 (4 issues) $320

GLASS AND CERAMICS
Steklo i Keramika
Vol. 39, 1982 (6 issues) $460

HIGH TEMPERATURE
Teplofizika Vysokikh Temperatur
Vol. 20, 1982 (6 issues) $400

HYDROTECHNICAL CONSTRUCTION
Gidrotekhnicheskoe Stroitel'stvo
Vol. 16, 1982 (12 issues) $305

INDUSTRIAL LABORATORY
Zavodskaya Laboratoriya
Vol. 48, 1982 (12 issues) $400

INSTRUMENTS AND EXPERIMENTAL TECHNIQUES
Pribory i Tekhnika Eksperimenta
Vol. 25, 1982 (12 issues) $460

JOURNAL OF APPLIED MECHANICS AND TECHNICAL PHYSICS
Zhurnal Prikladnoi Mekhaniki i Tekhnicheskoi Fiziki
Vol. 23, 1982 (6 issues) $420

JOURNAL OF APPLIED SPECTROSCOPY
Zhurnal Prikladnoi Spektroskopii
Vols. 36–37 (12 issues) $420

JOURNAL OF ENGINEERING PHYSICS
Inzhenerno-fizicheskii Zhurnal
Vols. 42–43, 1982 (12 issues) $420

JOURNAL OF SOVIET LASER RESEARCH
A translation of articles based on the best Soviet research in the field of lasers
Vol. 3, 1982 (4 issues) $95

JOURNAL OF SOVIET MATHEMATICS
A translation of Itogi Nauki i Tekhniki and *Zapiski Nauchnykh Seminarov Leningradskogo Otdeleniya Matematicheskogo Instituta im. V. A. Steklova AN SSSR*
Vols. 18–20, 1982 (18 issues) $680

LITHOLOGY AND MINERAL RESOURCES
Litologiya i Poleznye Iskopaemye
Vol. 17, 1982 (6 issues) $420

LITHUANIAN MATHEMATICAL JOURNAL
Litovskii Matematicheskii Sbornik
Vol. 22, 1982 (4 issues) $205

MAGNETOHYDRODYNAMICS
Magnitnaya Gidrodinamika
Vol. 18, 1982 (4 issues) $325

MATHEMATICAL NOTES
Matematicheskie Zametki
Vols. 31–32, 1982 (12 issues) $400

continued on inside back cover

Declassified and Approved For Release 2013/02/06 : CIA-RDP10-02196R000300020002-8